

University of Nebraska - Lincoln

DigitalCommons@University of Nebraska - Lincoln

---

Civil and Environmental Engineering Theses,  
Dissertations, and Student Research

Civil and Environmental Engineering

---

Spring 5-4-2023

## Three-Dimensional Structural Analysis of Temple 16 and Rosalila at Copan Ruinas

Luis Tuarez

University of Nebraska-Lincoln, lt Suarez98@huskers.unl.edu

Follow this and additional works at: <https://digitalcommons.unl.edu/civilengdiss>



Part of the [Civil Engineering Commons](#), and the [Structural Engineering Commons](#)

---

Tuarez, Luis, "Three-Dimensional Structural Analysis of Temple 16 and Rosalila at Copan Ruinas" (2023).  
*Civil and Environmental Engineering Theses, Dissertations, and Student Research*. 195.  
<https://digitalcommons.unl.edu/civilengdiss/195>

This Article is brought to you for free and open access by the Civil and Environmental Engineering at DigitalCommons@University of Nebraska - Lincoln. It has been accepted for inclusion in Civil and Environmental Engineering Theses, Dissertations, and Student Research by an authorized administrator of DigitalCommons@University of Nebraska - Lincoln.

THREE-DIMENSIONAL STRUCTURAL ANALYSIS OF TEMPLE 16 AND  
ROSALILA AT COPAN RUINAS

By

Luis Francisco Tuarez Mejia

A THESIS

Presented to the Faculty of

The Graduate College at the University of Nebraska

In Partial Fulfillment Requirements

For the Degree of Master of Science

Major: Civil Engineering

Under the Supervision of Professors Richard L. Wood & Christine E. Wittich

Lincoln, Nebraska

May, 2023

# THREE-DIMENSIONAL STRUCTURAL ANALYSIS OF TEMPLE 16 AND ROSALILA AT COPAN RUINAS

Luis Francisco Tuarez Mejia, M.S.

University of Nebraska, 2023

Advisors: Christine E. Wittich & Richard L. Wood.

Temple 16 is an ancient Maya structure located at the heart of the Copán Ruinas Acropolis in Western Honduras. Temple 16 contains several earlier structures within it that were built on top of each other throughout Copán's history. One of these earlier structures, Rosalila, is one of the most culturally significant structures within the Acropolis due to its preservation. An intricate series of archeological tunnels have been excavated throughout Temple 16 to allow for its study. However, significant cracking has been observed within Rosalila and several tunnels have experienced partial collapse. This not only poses a life safety issue for those utilizing the tunnels, but also demonstrates the risk to invaluable cultural heritage. To this end, this thesis aims to provide a rigorous structural assessment of Temple 16 and the buried Rosalila structure, accounting for its complex 3D tunnel system, to understand the leading causes of tunnel collapse and structure deterioration.

Geometric data was collected of the acropolis, Temple 16, Rosalila, and the complex network of tunnels using a combination of ground-based lidar and uncrewed aerial systems. The resulting point clouds were vectorized to yield a series of connected surfaces, which were then meshed as a solid to facilitate finite element analysis. Analyses

were conducted to understand both the current stress distribution within Temple 16 as well as to study the impact of various hypothetical tunnel backfilling scenarios to provide recommendations for preservation and tunnel safety. The generated finite element models were analyzed under three water saturation levels to account for the impact of heavy rainy seasons and water infiltration on the stress levels of the tunnels. From the analyses, sixty-three highly stressed areas were identified among the current tunnel system, with most of them being close or directly underneath Rosalila. From the tested hypothetical backfilling scenarios, it was found that, backfilling excavated sections can improve or worsen these stress concentrations depending on the location of the tunnel within the system. Finally, by analyzing Rosalila's current geometry, it was observed that the structure experiences high levels of stress on its southern side due to its location within Temple 16. From this, it was concluded that fixing exposed areas of Rosalila that were affected by excavation on its southern side can significantly alleviate the existing deterioration and improve the stress flow in these areas.



## **DEDICATION**

I would like to dedicate this thesis to my parents, Francisco and Paola, my brother, José Francisco, and my grandparents, Luis and Aracely, for being my main source of motivation and perseverance every day. I would also like to dedicate this work to my fiancé, Heidi, for her constant and unconditional love, support, and encouragement throughout this project.

## **AUTHOR'S ACKNOWLEDGMENTS**

I would like to express my gratitude to my advisors and mentors: Dr. Christine E. Wittich and Dr. Richard L. Wood, who are also chairs of my thesis committee. I would like to thank both for their continuous guidance and support during the course of this research project, and throughout my graduate studies. I would like to thank Dr. Wittich for her unconditional support as my main graduate advisor and for letting me be part of her research group. I would like to thank Dr. Wood for providing me with the opportunity to be part of this unique research project which has allowed me to grow as an engineer and a professional.

Next, I would like to thank Dr. Heather Richards-Rissetto, the final member of my thesis committee, for volunteering her time to serve on my thesis committee, collecting data in the field, and reviewing my work. As one of the leading experts on the history of Copán's ancient Maya civilization, I strongly appreciate her support on my thesis work with hopes that it will help in the conservation of this unique archeological site and its invaluable heritage to humanity.

This research was sponsored by the Asociación Copán, a Honduran non-profit organization dedicated to research and conservation of national heritage. Additional funding was from the University of Nebraska-Lincoln Research Council Interdisciplinary Research Grants. This work was completed utilizing the Holland Computing Center of the University of Nebraska, which receives support from the Nebraska Research Initiative. I would also like to thank Altair and its team for providing me with unlimited

access to their Hyperworks software package for the purposes of this investigation.

Access to this software was crucial for the completion of this project.

Field work and point cloud data used in thesis were collected at the Copán Archaeological Park in Copán, Honduras. This field work and data collection was made possible by the Honduran Institute for Anthropology and History (Instituto Hondureño de Antropología e Historia) and with the support of the Copán Association. Several members of the Asociación Copán were critical in data collection, analysis, and logistics, namely Ricardo Agurcia Fasquelle, Elisandro Garza, Manuel Cueva, and Liz Nutter-Valladares. The assistance and support of many other local individuals, including Luis Cueva, is gratefully acknowledged. External collaborators and their support to this project is greatly appreciated, including that by Dr. Loa Traxler of the University of New Mexico, Dr. Amy E. Thompson of the University of Texas at Austin (UT), and Chris Ploetz of UT.

Finally, I would like to thank my family and close friends for their constant love and support throughout my graduate studies. I could not have accomplished this without them.

## TABLE OF CONTENTS

DEDICATION .....	iv
AUTHOR’S ACKNOWLEDGMENTS .....	v
TABLE OF CONTENTS.....	vii
LIST OF FIGURES .....	xii
LIST OF TABLES .....	xxiv
CHAPTER 1 - INTRODUCTION.....	1
1.1 Motivation .....	1
1.2 Research Objectives .....	2
1.3 Organization of Thesis .....	3
CHAPTER 2 – LITERATURE REVIEW .....	5
2.1 The Evolution of Structure 10L-16 .....	5
2.1.1 Brief History of Copán Ruinas .....	5
2.1.2 Temple 10L-16 and Rosalila .....	8
2.1.3 Construction Methods and Construction Materials of Temple 10L-16.....	14
2.2 Archaeological Tunnels beneath Temple 16.....	15
2.2.1 History of Archaeological Tunnel Excavations in Copán.....	15
2.2.2 Tunnel Stabilization Practices .....	17
2.2.3 Current State of Tunnel System and Related Structural Problems.....	20

2.3 Current Research Work and Conservation Studies on the Copán Acropolis Tunnels .....	22
2.3.1 3D Mapping of the Acropolis and Archaeological Tunnels .....	23
2.3.2 Preliminary Structural Assessment of Excavated Archaeological Tunnels of Copán .....	26
2.4 Finite Element Analysis for Cultural Structures .....	27
2.5 From lidar to FEM for Cultural Applications and Underground Structures .....	30
2.5.1 Lidar and FEA for Cultural Heritage Applications .....	31
2.5.2 Lidar and FEA for Underground and Earthen Structures .....	35
2.6 Scope and Contribution .....	36
CHAPTER 3 – GEOSPATIAL DATA MODELING .....	38
3.1 Chapter Overview .....	38
3.2 Data Acquisition and Point Cloud Generation .....	39
3.2.1 Lidar .....	39
3.2.1.1 Lidar Data Collection .....	39
3.2.1.2 Lidar Data Registration .....	43
3.2.2 UAS Data Collection and Point Cloud Generation .....	44
3.3 Point Cloud Data Processing .....	46
3.3.1 Cleaning and Filtering .....	46

3.3.2 Coordinate Transformation.....	48
3.4 Geometry Vectorization .....	57
3.4.1 Vectorization of Temple 16's Exterior Point Cloud Data .....	57
3.4.2 Vectorization of Interior Tunnels Point Cloud Data. ....	59
3.4.2 Vectorization of Rosalila's Replica Point Cloud Data .....	61
3.5 Geometry Generation .....	62
3.5.1 Temple 16 Exterior and Interior Tunnel Geometry Generation .....	62
3.5.2 Rosalila's Exterior Geometry Generation .....	66
CHAPTER 4 – FINITE ELEMENT MODELING.....	70
4.1 Chapter Overview .....	70
4.2 General Model Characterization .....	70
4.2.1 Element Type.....	70
4.2.2 Analysis Considerations and Loading .....	72
4.3 Material Modeling Characterization .....	74
4.3.1 Infill Material Characterization .....	74
4.3.2 Infill Material Modeling .....	80
4.3.3 Rosalila's Material Modeling and Characterization.....	82
4.4 Validation of Tunnel Stress Analysis and Boundary Conditions.....	83
4.4.1 Proposed Case Study .....	83

4.4.2 Finite Element Model Setup and Results .....	86
4.4.3 Closed-Form Solution Approximation for Stress Analysis.....	91
4.4.4 Validation Study .....	96
4.5 Validation and Numerical Convergence of Exterior Geometry.....	98
4.5.1 Convergence Study and Finite Element Results.....	99
4.5.2 Closed Form Solution Approximation for Bearing Pressure.....	104
4.5.3 Model Validation.....	107
CHAPTER 5 – RESULTS AND ANALYSIS.....	108
5.1 Chapter Overview .....	108
5.2 Model Configuration.....	109
5.2.1 Objectives .....	109
5.2.2 Analysis Approach Limitations .....	116
5.2.3 Configuration Geometry.....	118
5.3 Results and Discussion.....	129
5.3.1 General Remarks on Temple 16 without Tunnels .....	129
5.3.2 Temple 16 Tunnels .....	134
5.3.2.1 Current State of Tunnels .....	134
5.3.2.2 Overview of Stress Changes for Other Scenarios.....	140
5.3.2.3 Impact on Upper-Level Tunnels .....	142

5.3.2.4 Impact on Lower-Level Tunnels.....	149
5.3.3 Rosalila .....	154
5.3.3.1 Current State of Rosalila.....	154
5.3.3.2 Backfilling of Rosalila’s Center Room.....	158
5.3.3.3 Rosalila’s Southern Wall Repair.....	163
CHAPTER 6 – CONCLUSIONS AND FUTURE WORK.....	165
6.1 Research Findings .....	165
6.2 Future Work .....	167
REFERENCES .....	170
APPENDIX A - LS-DYNA MASTER SCRIPT .....	181
APPENDIX B -STRESS CONCENTRATIONS RESULT LIST .....	184



## LIST OF FIGURES

Figure 2.1. Geographical location of the Copán region (Google Earth, 2023).....	6
Figure 2.2. Copán Acropolis during the late 8th century (Proskouriakoff, 1946). ....	7
Figure 2.3. Copán Acropolis section showing superimposed structures (Larios Villalta, 2020). ....	8
Figure 2.4. Temple 10L-16 (also known as Temple 16) in Copán Acropolis (Flickr User, 2019). ....	9
Figure 2.5. Cross-section of Temple 16 showing underlying construction sequence (Fash et al., 2004). ....	10
Figure 2.6. Plan view of Temple 16 (Fash et al., 2004). ....	11
Figure 2.7. Replica of Rosalila at Copán Sculpture Museum (Asociación Copán, 2019).12	
Figure 2.8. Floor plan of Rosalila's lower level (Fash et al., 2004). ....	13
Figure 2.9. Plan view of the Copán Acropolis with sketch of archaeological tunnels (Larios Villalta, 2018). ....	16
Figure 2.10. Cracks observed in exposed walls (Lacombe et al., 2020). ....	20
Figure 2.11. Sketch showing the impact of water flow in stabilized tunnels (Lacombe, 2017). ....	22
Figure 2.12. Screenshot of 3D model of tunnels beneath Temple 16 by Lacombe (2019). ....	26
Figure 3.1. General FEA model generation pipeline. ....	38
Figure 3.2. Lidar scanning of Temple 16 during site expedition on the summer of 2021.40	

Figure 3.3. FARO s350 mounted on telescopic tripod for scanning interior tunnel areas. .....	42
Figure 3.4. FARO s350 mounted on telescopic tripod in inverted position for scanning exterior tunnel areas. ....	42
Figure 3.5. DJI Mavic Pro 2 during UAS data collection. ....	45
Figure 3.6. Aerial view of UAS point cloud data of temple 16 and surrounding areas of the acropolis (scale in meters). ....	45
Figure 3.7. View from the southwest of Temple 16 and surrounding areas. ....	46
Figure 3.8. View from the southwest of lidar point cloud of Temple 16 after segmentation (scale in meters). ....	47
Figure 3.9. View from the southwest of UAS point cloud of Temple 16 after segmentation (scale in meters). ....	48
Figure 3.10. View from the southwest of cloud-to-cloud distance comparison between UAS and high-resolution point clouds of Temple 16 after alignment process (scale in meters). ....	52
Figure 3.11. Aerial view of Temple 16 tunnels point cloud collected during the summer of 2021 (scale in meters). ....	53
Figure 3.12. View from the west of Temple 16 tunnels point cloud (collected during the summer of 2021) prior to segmentation and alignment (scale in meters). ....	53
Figure 3.13. View from the west of Temple 16 tunnels point cloud (collected during the summer of 2021) after segmentation and alignment (scale in meters). ....	54

Figure 3.14. View from the west of Temple 16 tunnels point cloud after segmentation and alignment between 2021 and 2022 datasets (scale in meters). .....	54
Figure 3.15. Aerial view of Temple 16 tunnels point cloud after segmentation and alignment between 2021 and 2022 datasets (scale in meters). .....	55
Figure 3.16. View from the southwest of Rosalila's replica point cloud (scale in meters). .....	55
Figure 3.17. View from the southwest of cloud-to-cloud distance comparison between Rosalila's replica and exposed sections of original structure along the tunnel system (scale in meters). .....	56
Figure 3.18. Aerial view of final setup of Temple 16, tunnel system and replica's point clouds after alignment (scale in meters). .....	56
Figure 3.19. View from the southwest of Temple 16's point cloud with vectorized features. ....	58
Figure 3.20. Aerial view of Temple 16's point cloud with vectorized features. ....	59
Figure 3.21. Aerial view of extracted tunnel cross-sectional slices. ....	60
Figure 3.22. Plan view of vectorized tunnel slices. ....	60
Figure 3.23. View from the southwest of extracted cross-sectional slices from Rosalila's replica point cloud. ....	61
Figure 3.24. View from the southwest of Rosalila's replica vectorized cross-section. ....	62
Figure 3.25. Rendered plan view of Temple 16's vectorized features in AutoCAD. ....	64
Figure 3.26. Rendered plan view of Temple 16 tunnels and Rosalila's vectorized features in AutoCAD. ....	64

Figure 3.27. Rendered plan view of Temple 16's regenerated geometric model in AutoCAD (units in meters).....	65
Figure 3.28. Rendered view from the west of Temple 16's regenerated geometric model in AutoCAD (units in meters).....	65
Figure 3.29. Rendered plan view of Temple 16's tunnels regenerated geometric model. Rosalila's excavated rooms and tunnels marked with red. ....	66
Figure 3.30. View from the east of Temple 16's point cloud system showing overlap between replica and Temple 16 exterior surface (scale in meters).....	67
Figure 3.31. Rendered view from the west of Rosalila's regenerated geometric model (units in meters). ....	68
Figure 3.32. Rendered view from the southwest of Rosalila's regenerated geometric model (units in meters). ....	68
Figure 3.33. Rendered view from the southwest of Rosalila and Temple 16 tunnels geometric models. ....	69
Figure 3.34. Rendered view from the west of Rosalila and Temple 16 tunnels regenerated geometric models. ....	69
Figure 4.1. LS-DYNA ELFORM 16 10-noded tetrahedron and its integration points (red marked) (DYNAmore, 2011).....	71
Figure 4.2. Applied unit load curve for gravity loading. ....	73
Figure 4.3. Unified Soil Classification System (USCS) chart. ....	77
Figure 4.4. Mohr-Coulomb vs Drucker-Prager failure envelopes. ....	81

Figure 4.5. Cross-sectional View of Proposed Circular Cavity Validation Model (units in meters).....	85
Figure 4.6. Isometric View of Proposed Circular Cavity Validation Study (units in meters).....	86
Figure 4.7. Isometric view of circular cavity finite element model.....	87
Figure 4.8. Cross-sectional view of circular cavity finite element model. ....	88
Figure 4.9. Vertical stress distribution along cross-section at model midspan.....	89
Figure 4.10. Horizontal stress distribution along cross-section at model midspan. ....	89
Figure 4.11. Shear stress distribution along cross-section at model midspan. ....	90
Figure 4.12. Tresca stress distribution along cross-section at model midspan. ....	91
Figure 4.13. Analysis of circular cavity under hydrostatic loading (Celada & Beniawski, 2019). ....	93
Figure 4.14. Closed-form solution vertical stress distribution.....	94
Figure 4.15. Closed-form solution horizontal stress distribution. ....	94
Figure 4.16. Closed-form solution shear stress distribution. ....	95
Figure 4.17. Closed-form solution Tresca stress distribution. ....	95
Figure 4.18. Normalized vertical stress vs normalized radial distance.....	97
Figure 4.19. View from the southwest of exterior of Temple 16's finite element model. ....	99
Figure 4.20. Vertical stress distribution of mesh #1 at the XZ plane. ....	101
Figure 4.21. Vertical stress distribution of mesh #2 at the XZ plane. ....	102
Figure 4.22. Vertical stress distribution of mesh #3 at the XZ plane. ....	102
Figure 4.23. Vertical stress distribution of mesh #4 at the XZ plane. ....	103

Figure 4.24. Vertical stress distribution of mesh #5 at the XZ plane. ....	103
Figure 4.25. Convergence study of exterior of Temple 16's meshes. ....	104
Figure 4.26. Proposed embankment profile for approximating closed-form solution (units in meters). ....	105
Figure 4.27. Stress increment due to asymmetric embankment at a point "P" (Murthy). .....	106
Figure 4.28. Vertical stress distribution in infill below grade of Temple 16. ....	106
Figure 5.1. View from the south of Rosalila's southern side with surrounding tunnels.	111
Figure 5.2. View from the south of Rosalila's southern side showing overlapped tunnels section on upper wall section. ....	111
Figure 5.3. Rosalila's southwest corner: comparison between replica's exterior surface and Rosalila's current state due to tunnel excavation. ....	112
Figure 5.4. Rosalila's southeast corner: comparison between replica's exterior surface and Rosalila's current state due to tunnel excavation. ....	112
Figure 5.5. Comparison of expected stress distributions around a circular cavity surrounded by media modeled as linearly elastic (top) and elastic-plastic (bottom). ....	118
Figure 5.6. View from the southwest of Temple 16's exterior mesh (typical for all proposed configurations). ....	120
Figure 5.7. View from the west of Temple 16's exterior mesh (typical for all proposed configurations). ....	121
Figure 5.8. View from the southwest of Rosalila's exterior mesh (typical for configurations A, C, E). ....	121

Figure 5.9. View from the south of Rosalila's exterior mesh (typical for configurations A, C, E).	122
Figure 5.10. View from the southwest of Rosalila's exterior mesh for configurations B and D.	122
Figure 5.11. View from the south of Rosalila's exterior mesh for configurations B and D.	123
Figure 5.12. View from the southwest of Rosalila's exterior mesh for configuration F.	123
Figure 5.13. View from the south of Rosalila's exterior mesh for configuration F.	124
Figure 5.14. Plan view showing excavated areas within Rosalila (typical for configurations A, C, F).	124
Figure 5.15. Plan view showing excavated areas within Rosalila for configuration E (center room has been filled).	125
Figure 5.16. Plan view showing tunnel system modeled for configuration A.	125
Figure 5.17. View from the west showing tunnel system modeled for configuration A.	126
Figure 5.18. View from the north showing tunnel system modeled for configuration A.	126
Figure 5.19. View from the west showing tunnel system modeled for configuration C.	127
Figure 5.20. View from the north showing tunnel system modeled for configuration C.	127
Figure 5.21. View from the west showing tunnel system modeled for configuration D.	128
Figure 5.22. View from the north showing tunnel system modeled for configuration D.	128

Figure 5.23. Cross-sectional cut at YZ plane of configuration B stress results at midspan (90% saturation level).....	131
Figure 5.24. Cross-sectional cut at XZ plane of configuration B stress results showing Rosalila's southern profile (90% saturation level).....	131
Figure 5.25. Cross-sectional cut at XZ plane of configuration B stress results showing Rosalila's southern profile (90% saturation level).....	132
Figure 5.26. View from the southwest of configuration B stress results of Rosalila (90% saturation level).....	132
Figure 5.27. View from west of isosurface showing areas influenced by Rosalila's loading for configuration B stress results (90% saturation level).....	133
Figure 5.28. Tilt-up view from west of isosurface showing areas influenced by Rosalila's loading for configuration B stress results (90% saturation level).....	133
Figure 5.29. Transparent view from the west showing tunnel stress results for configuration A (90% saturation level).....	135
Figure 5.30. Transparent plan view showing tunnel stress results for configuration A (90% saturation level).....	136
Figure 5.31. Front view of isosurface showing areas with stress levels higher than the median Tresca stress around tunnels for configuration A. ....	136
Figure 5.32. Plan view of isosurface showing areas with stress levels higher than the median Tresca stress around tunnels for configuration A. ....	137



Figure 5.33. Plan view of isosurface showing areas with stress levels higher than the median Tresca stress around tunnels surrounding southern side of Rosalila and tunnels around Oropéndola for configuration A. ....	137
Figure 5.34. Plan View of isosurface showing areas showing approximated radius of areas influenced by Rosalila for configuration A stress results. ....	138
Figure 5.35. Close-up view of isosurface showing areas with stress levels higher than the median Tresca stress around a tunnel junction near west entrance. ....	138
Figure 5.36. Close-up view of isosurface showing areas with stress levels higher than the median Tresca stress around a tunnel sharp corner. ....	139
Figure 5.37. Front view of isosurface showing areas with stress levels higher than the median Tresca stress around lower-level tunnels for configuration A (upper infill layer hidden for clarity). ....	139
Figure 5.38. Plan view of isosurface showing areas with stress levels higher than the median Tresca stress around lower-level tunnels for configuration A (upper infill layer hidden for clarity). ....	140
Figure 5.39. Front view of isosurface showing areas with stress levels higher than the median Tresca stress around upper-level tunnels for configuration C. ....	145
Figure 5.40. Plan view of isosurface showing areas with stress levels higher than the median Tresca stress around upper-level tunnels for configuration C. ....	145
Figure 5.41. Comparison of areas with stress levels greater than the median Tresca stress at upper-level tunnels between configuration A (all tunnels included) and configuration C (upper-level tunnels only) (view from the west).....	146

Figure 5.42. Comparison of areas with stress levels greater than the median Tresca stress between configuration A (all tunnels included) and configuration C (upper-level tunnels only) (plan view).....	147
Figure 5.43. Comparison of area with stress levels greater than the median Tresca stress of upper-level tunnel section that is close to lower-level tunnels in configuration A (all tunnels included) with configuration C (upper-level tunnels only) (view from west). ..	148
Figure 5.44. View from the northeast of Rosalila surrounding areas with stress levels greater than the median Tresca stress for configuration C (upper-level tunnels only) ..	149
Figure 5.45. View from the west of isosurface showing areas with stress levels higher than 95% of maximum Tresca stress around upper-level tunnels for configuration D. .	151
Figure 5.46. Plan view of isosurface showing areas with stress levels higher than 95% of maximum Tresca stress around upper-level tunnels for configuration D.....	151
Figure 5.47. Comparison of areas with stress levels higher than 95% of maximum Tresca stress at lower-level tunnels between configuration A (all tunnels included) and configuration D (lower-level tunnels only) (plan view). ....	152
Figure 5.48. View from northeast of areas with stress levels higher than 95% of maximum Tresca stress at tunnels underneath Rosalila configuration D (lower-level tunnels only).....	153
Figure 5.49. View from the southwest of Rosalila stress results for configuration A (90% saturation level).....	155
Figure 5.50. View from the northeast of Rosalila stress results for configuration A (90% saturation level).....	155

Figure 5.51. Comparison of stress concentrations level at areas surrounding Rosalila between configuration A (all tunnels included) and configuration B (no tunnels included) (plan view). .....	156
Figure 5.52. Comparison of stress concentrations level at areas surrounding Rosalila between configuration A (all tunnels included) and configuration B (no tunnels included) (view from the southeast). .....	157
Figure 5.53. Transparent view from the southwest of Rosalila stress results for configuration A (90% saturation level). .....	159
Figure 5.54. Transparent plan view of Rosalila stress results for configuration A (90% saturation level). .....	159
Figure 5.55. View from the south of cross-sectional cut of configuration A Rosalila stress results at Rosalila's center room midspan (90% saturation level). .....	160
Figure 5.56. View from the west of cross-sectional cut of Configuration A Rosalila stress results at Rosalila's center room midspan (90% saturation level). .....	160
Figure 5.57. Comparison of stress concentrations levels at areas surrounding Rosalila's center room between configuration A (all tunnels included) and configuration E (center room filled) (view from the west). .....	161
Figure 5.58. comparison of stress concentrations levels at areas surrounding Rosalila's center room between configuration A (all tunnels included) and configuration E (center room filled) (view from the south). .....	162

Figure 5.59. Comparison of stress concentrations levels at Rosalila's southern wall between configuration A (current state) and configuration E (southern wall fixed) (view from the south).....	164
Figure B.1. Top view of 63 identified areas with high stress levels along Temple 16 tunnels (top) and isolated locations (bottom).....	186

## LIST OF TABLES

Table 3.1. Summary of lidar instruments and collected datasets.....	41
Table 3.2. Summary of number of scans collected per location and year. ....	41
Table 4.1. Soil parameters used by Pires et al. (2021) for characterizing silty sand infill layer.....	75
Table 4.2. Chosen material characterization parameters. ....	79
Table 4.3. LS-DYNA material input parameters. ....	82
Table 4.4. Generated mesh densities for convergence study. ....	99
Table 5.1. Proposed analysis configurations and comparison cases.....	114
Table 5.2. Considered saturation levels for analysis of each infill layer. ....	116
Table 5.3. Stress changes at identified locations at 90% saturation level.....	141
Table 5.4. Summary of results comparison at 70% saturation level.....	142
Table 5.5. Summary of results comparison at 50% saturation level.....	142
Table B.1. Description and location of identified stress concentrations at upper-level tunnels. ....	184
Table B.2. Description and location of identified stress concentrations at lower-level tunnels. ....	185
Table B.3. Stress concentration results for upper-level tunnels at 90% saturation.....	186
Table B.4. Stress concentration results for lower-level tunnels at 90% saturation.....	188
Table B.5. Stress concentration results for upper-level tunnels at 70% saturation.....	189
Table B.6. Stress concentration results for lower-level tunnels at 70% saturation.....	190
Table B.7. Stress concentration results for upper-level tunnels at 50% saturation.....	191

Table B.8. Stress concentration results for lower-level tunnels at 50% saturation.....	192
--	-----

## CHAPTER 1 - INTRODUCTION

### 1.1 Motivation

Today, Copán is UNESCO World Heritage Site located in Western Honduras. However, between the 5<sup>th</sup> and 9<sup>th</sup> centuries A.D Copan was the most important cultural and commercial center at the southeast periphery of the Maya world. The Copán Acropolis, the core of the city's main civic-ceremonial precinct, comprises temples and monumental structures that were built on top of each other throughout the reigns of the 16 rulers that shaped this site to its final form. One of these structures, Temple 10L-16 (more commonly known as Temple 16,) is located at the cosmological center of the Acropolis, serving a pivotal role in this ancient city's political, administrative, and religious functions across four centuries (Bell et al. 2004; Sharer et al. 1999; Sharer et al. 1992; Traxler et al. 2004). Temple 16 contains several earlier structures within it that were built on top of each other throughout Copán's history. One of these earlier structures, Rosalila, is one of the most culturally significant structures within the Acropolis. Unlike other buried structures, Rosalila was not demolished, but it was carefully filled, preserved, and buried by the time the final construction phases of Temple 16 began (Agurcia Fasquelle 2004).

An intricate series of archeological tunnels have been excavated throughout Temple 16 to allow for its study. However, significant cracking has been observed within Rosalila and several tunnels have experienced partial collapse. This not only poses a life safety issue for those utilizing the tunnels, but also demonstrates the risk to invaluable cultural heritage. There is an urgent need to document and analyze Temple 16 and its

archeological tunnel system so appropriate conservation decisions can be made. This requires a robust and comprehensive structural analysis of Temple 16, its underlying tunnels, and Rosalila, that accounts for their intricate geometries and spatial orientation within the overall structure.

## **1.2 Research Objectives**

This thesis aims to conduct a detailed structural assessment of Temple 16, accounting for the complex 3D tunnel system and the impact on Rosalila, to understand the leading causes of tunnel collapse and structural deterioration. To reach this goal, the first research objective is to develop a high-fidelity three-dimensional geometry that represents the current state of Temple 16, including Rosalila and the underlying archeological tunnel system by leveraging ground-based lidar and uncrewed aerial systems. The second research objective is to develop and calibrate finite element models based on the generated geometries and available material information to adequately identify concentrations of high stress within the system via linearly elastic static finite element analysis. Finally, the third research objective is to study the impact of the current excavations on the stress concentrations within Temple 16 and make recommendations for conservation. For this last objective, geometric variations are made within the finite element model to represent a series of hypothetical configurations where certain excavated areas of the tunnel system are backfilled to study the impact on the stress concentrations.



### 1.3 Organization of Thesis

The fulfillment of these three research objectives centered on the generation of a three-dimensional finite element model of Temple 16 and its archeological tunnels. However, to achieve these objectives required multiple components that are presented and discussed in subsequent chapters and appendices including collected background information, as well as the steps followed for generating, processing, and analyzing Temple 16's current geometry.

**Chapter 2** provides a literature review that highlights the historical relevance and conservation challenges of Temple 16 and Rosalila due to archeological tunnel excavation. Additionally, this chapter explores previous case studies involving geometric data acquisition and structural analyses for historic structures. Finally, the scope and contribution of this thesis are discussed within the context of the existing historical and technical background.

**Chapter 3** outlines the methodology developed to generate high-fidelity finite element geometry models of Temple 16, Rosalila, and the archeological tunnel system, which leverages field-collected point cloud data. This chapter also includes a discussion of the methods employed and data collected over multiple field missions to Copán.

**Chapter 4** further explains the methods and inputs used to generate and characterize the finite element models based on the high-fidelity generated geometries and available infill material knowledge. This chapter then focuses on validating the numerical approach, selected boundary conditions, and material inputs via numerical convergence studies.

**Chapter 5** uses the processed geometric information and calibrated inputs to identify areas of concern along the archeological tunnel system and Rosalila by studying six different geometric configuration cases. Additionally, to account for the effect of the heavy rainy season, each of these configurations is analyzed under three different water saturation levels. Results obtained from these finite element simulations are compared to understand the influence of the tunnel excavations on the stress distribution and concentrations.

**Chapter 6** summarizes the conclusions and recommendations of this thesis and outlines suggested future work related to the analysis and conservation of Temple 16, Rosalila, and its archeological tunnels.

## **CHAPTER 2 – LITERATURE REVIEW**

Given Temple 16's unique history and cultural relevance, this chapter aims to set the historical and technical foundations that will be used to define the scope and contribution of this investigation by relating them with the efforts that have been made to preserve this and similar archaeological sites to future generations (e.g., Chase et al. 2020; Lercari et al. 2018). To achieve this, the first half of this chapter covers a literature review of the historical background and preservation challenges of Temple 16, Rosalila, and the archaeological tunnel system. Finally, a literature review that justifies the selected modeling approach is covered in the second half of this chapter. For this part, a comprehensive review of previous cases where lidar and the Finite Element Method were used for generating and analyzing models of historic structures worldwide is presented. Hence, the end of this chapter considers this overall review to introduce the scope of this thesis and set a clear structure for subsequent chapters.

### **2.1 The Evolution of Structure 10L-16**

#### **2.1.1 Brief History of Copán Ruinas**

Copán is a Classic Period Maya site located in the Western part of Honduras, near the Guatemalan border (see Figure 2.1). The first historical documentation by Europeans was in 1570 by the Spanish explorer Diego García de Palacio during his expeditions around the area. This Maya site is one of the most relevant sites of the ancient Maya because it served as the political center and cultural focus of a larger territory that at its peak covered over 250 square kilometers in the southeast portion of the Maya area (Fash 2001).



Figure 2.1. Geographical location of the Copán region (*Google Earth, 2023*).

The Maya royal dynasty of Copán reigned from 426-820 A.D. Its first ruler, K'inich Yax, K'uk' Mo, arrived at Copán in 426 A.D and was succeeded by another 15 kings that shaped the architecture of the Acropolis and surrounding areas to become one of the greatest Maya cities of the Classic Maya Period (Stuart 2004). The Acropolis constitutes a critical part of the Copán's main civic-ceremonial that provides key insights to the history, development, and significance of the city (Figure 2.2). The Acropolis is the result of four centuries of superimposed construction campaigns, with each phase having a new structure dedicated to the ruler of the time. When a new king ascended to power,

the previous structure would be filled and demolished to serve as the base of a new one. This unique construction approach led the Acropolis to rise 30 meters above grade at its highest peak (Agurcia Fasquelle, 2004). The final construction phase of the Acropolis encompasses the exterior structures exposed to the environment and make up this main complex (Figure 2.3). The most notable structures of the Acropolis are Temple 22, the focal point of the Acropolis's East Court (von Schwerin 2011), and Temple 16, the focal point of the Acropolis' West Court, particularly in the later years of the Copán dynasty.

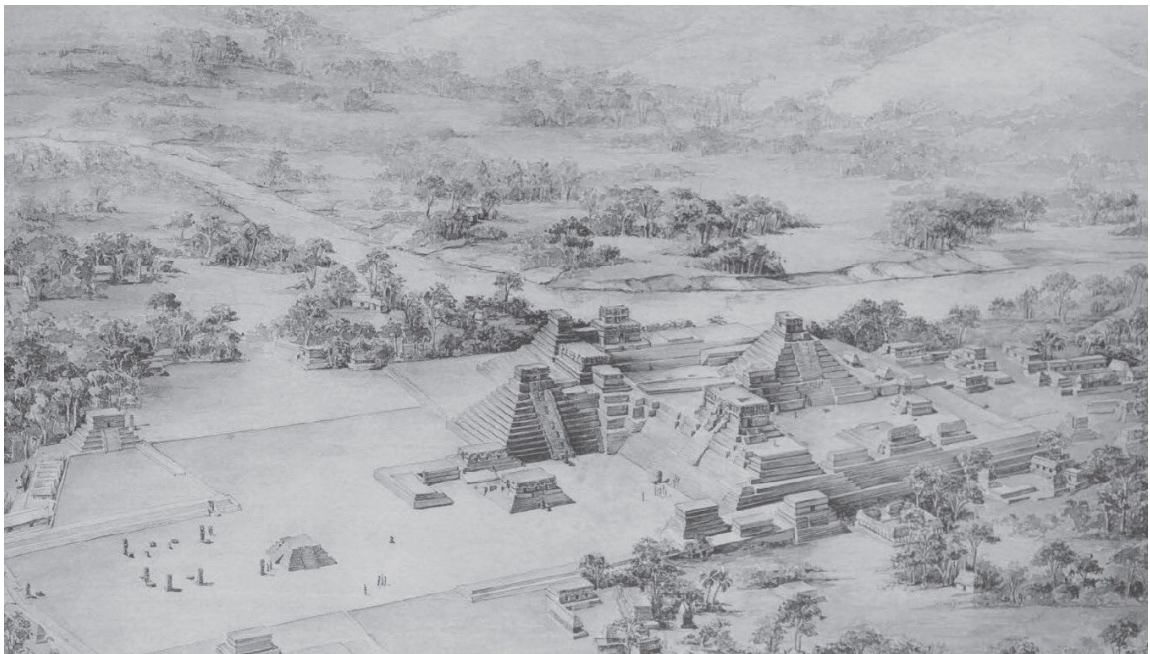


Figure 2.2. Copán Acropolis during the late 8th century (*Proskouriakoff, 1946*).

### 2.1.2 Temple 10L-16 and Rosalila

The location on which Temple 10L-16 (also referred to as Temple 16), and its underlying structures, was the cosmological origin point of the ancient kingdom of Copán, playing a key role in its social, economic, and religious power for over 400 years (Figure 2.4). Geographically, Temple 16 is the fundamental component linking the Acropolis's two main plazas: the West and East Courts. It is the tallest structure at Copán, with an estimated height of more than 20 meters above the West Court and 30 meters above the Great Plaza. This structure is the last of a long sequence of structures that was located at the geographical heart of the Acropolis. Temple 16 covers a series of earlier structures that form a sacred central axis for the Acropolis (axis Mundi), which was revered from the beginning of the dynasty, around 427 A.D., according to Agurcia et al. (2004). At the very bottom of this sequence, the residence of the First Ruler of Copán (known as Hunal (9<sup>th</sup>)) can be found about 30 meters below grade, and it serves as the tomb of this first king. Above Hunal, a substructure known as Yehnal (8<sup>th</sup>) was built by Copán's first rulers. Yehnal serves as the base for Margarita and Xukpi (7<sup>th</sup>), with Xukpi



having been almost wholly demolished for building Jade-Chile Verde/ Dulcinea (6<sup>th</sup>) and Celeste (5<sup>th</sup>). Similar to what happened to its predecessors, Celeste was partially destroyed to build Rosalila (4<sup>th</sup>), one of the most archaeologically relevant structures of this sequence, and its substructure Azul. On the Southeast of Rosalila, a similar temple known as Oropéndola was also built beneath Temple 16 at around the same time as Rosalila. Both Oropéndola and Rosalila were buried beneath Púrpura 1/ Jilguero (3<sup>rd</sup>), and Púrpura 2 (2<sup>nd</sup>), the last known structure that lies directly beneath the surface of Temple 16 (1<sup>st</sup>), which makes up to 70% of its bulk volume, as shown in Figure 2.5 (Agurcia Fasquelle & Fash, 2005). It has been theorized that the rest of Temple 16 was finished using the remaining terraces that were potentially built and demolished on top of Purpura as infill material.



Figure 2.4. Temple 10L-16 (also known as Temple 16) in Copán Acropolis (*Flickr User, 2019*).

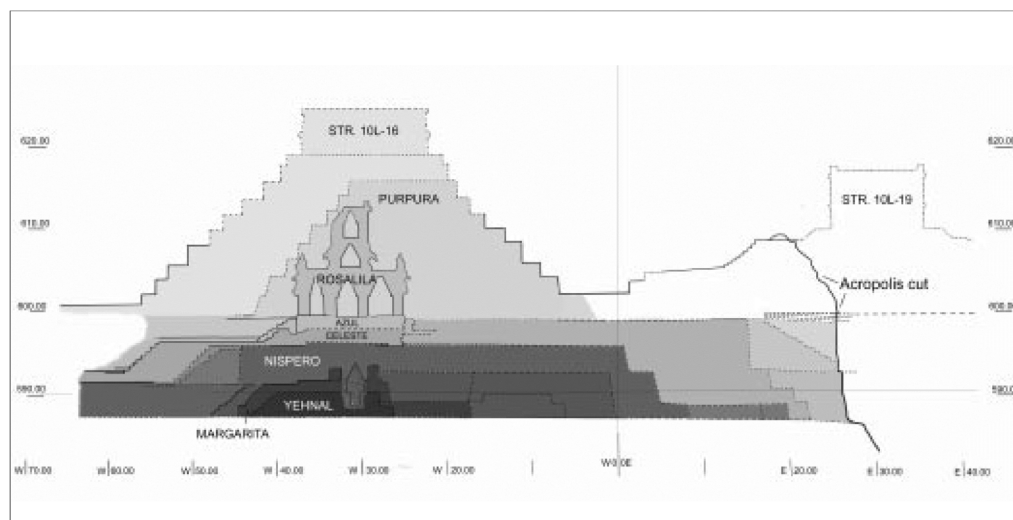


Figure 2.5. Cross-section of Temple 16 showing underlying construction sequence (Fash et al., 2004).

Temple 16 is the last monumental construction at Copán and was built by Yax Pasaj, Copán's 16<sup>th</sup> and final dynastic ruler. On its outside, this structure is covered with volcanic tuff and decorative stucco. It comprises ten stepped terraces with an average height of 1.90 meters. At its top, there are remains of what used to be a superstructure with an inner chamber and an internal stairway, and entrances facing the four main cardinal directions (Figure 2.6). At its base, Temple 16 has been measured to be more than 40 meters in length on its three free-standing sides. The northern side of this structure is attached to a platform that connects it with the rest of the structures of the Acropolis. The central axis of Temple 16 is shifted 13 meters to the south from the leading superimposed structure group (Rosalila/Azul, Celeste, Margarita, Yehnal, and Hunal). A 19-meter-high central staircase can be found on the west side of Temple 16. This staircase comprises 46 steps from grade level to the top of the structure. It has been



measured to be 16.2 meters wide at its base. It is divided into two sections: the lower part, which is made of 19 steps wide steps, and the upper part, which is made of 27 larger and narrower steps that have a measured average width of 10.6 meters, giving the whole staircase an appearance of an inverted “T.” (Agurcia Fasquelle & Fash, 2005)

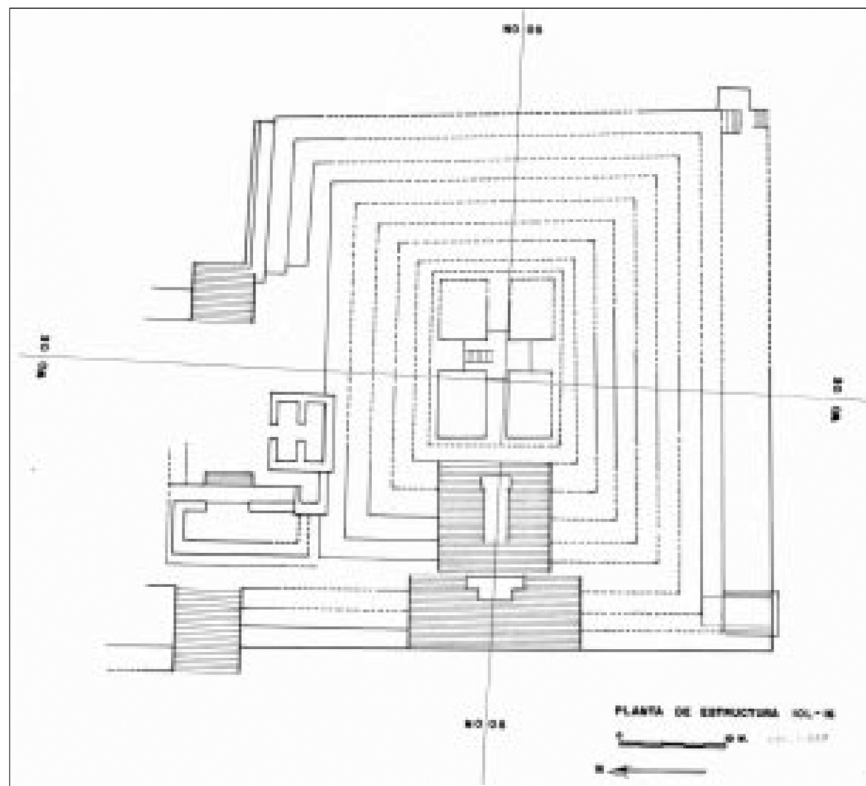


Figure 2.6. Plan view of Temple 16 (Fash et al., 2004).

Rosalila (also known as Temple 10L-16 4<sup>th</sup>) is the first discovered structure that was completely preserved and not demolished during the construction sequence of Temple 16. This structure served as the principal religious temple during the 6<sup>th</sup> century A.D, which makes it part of Copán’s Early Classic Architecture. Honduran archaeologist Ricardo Agurcia discovered it on June 23, 1989, through archaeological tunnel

excavations. Its architecture and sculptures are mostly preserved, providing a unique insight into ancient Maya engineering and aesthetics, as they look like when it was being used (see Figure 2.7). Excavations around this structure indicate that it was buried with great care. According to statistics, this structure is 97% intact (Asociación Copán, 2019). Its inner rooms and stucco decorations were carefully filled with mud and smaller rocks, allowing them to retain most of their original multicolored paint. Its exterior was coated with a thick white paint for its interment, performed with a religious ceremony (Asociación Copán, 2019).



Figure 2.7. Replica of Rosalila at Copán Sculpture Museum (Asociación Copán, 2019).

Based on archaeological excavations, Rosalila has three primary levels and an approximate height of 12.90 meters. The base level has approximated dimensions of 18.50 meters by 12.50 meters, with the longest dimension running along the north-south direction. This level is 5.70 meters high, divided into four main rooms (Figure 2.8) with

an average size of 11.2 meters and 2.4 meters. The second floor has a measured height of 3.7 meters, 11 meters long by 5 meters wide, leaving a 3-meter exterior corridor with respect to the base level bounded by 40-cm-high parapets. This floor has a single room that is 8.6 meters by 2.4 meters and has no connection to the base level as it only serves decorative purposes. Finally, the third floor has a measured height of 3.5 meters and base dimensions of 4.30 by 8.20 meters. Inside this level, three small cubicles were separated by two narrow windows that ran along the east-west direction. This last level is the most poorly preserved level of the structure, with the northern cubicle mostly destroyed during the construction of the final superstructure of Temple 16 (Fash et al, 2004).

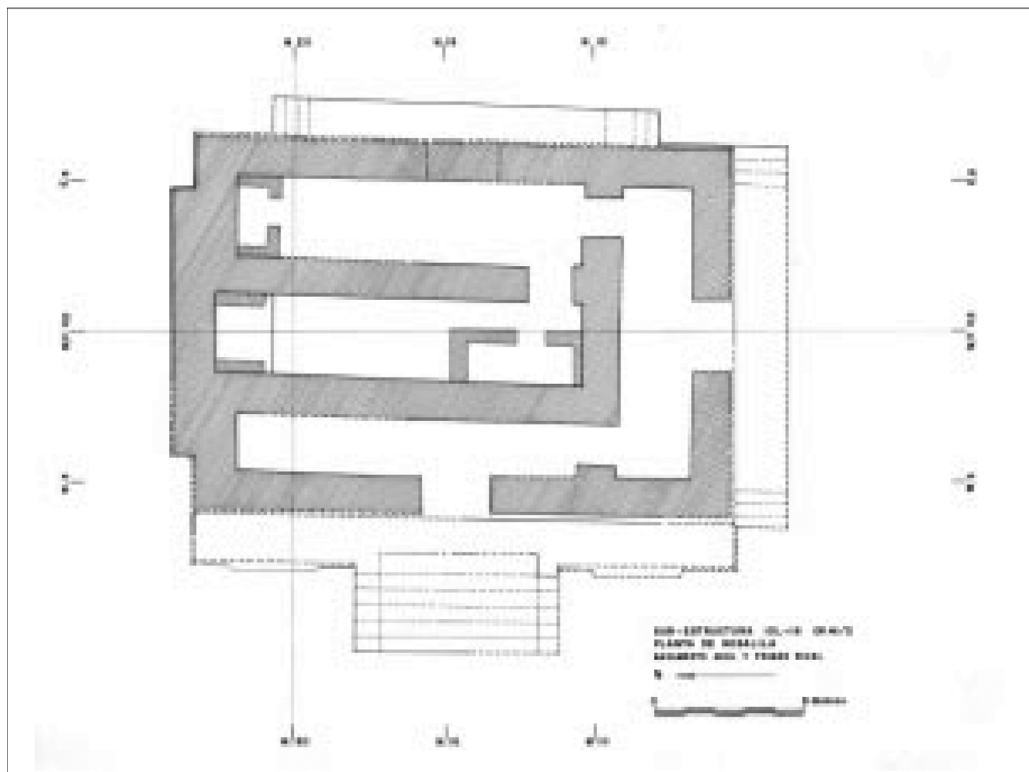


Figure 2.8. Floor plan of Rosalila's lower level (Fash et al., 2004).

### **2.1.3 Construction Methods and Construction Materials of Temple 10L-16**

The Copán Acropolis was built over four centuries by the ancient Maya who achieved an excellent level of mastery in constructing their structures with the local materials (Lacombe, Fash, & Fash, 2020). Copán's architects heavily relied on the sediments found along the Copán River to build their structures. Because the Copán Valley is in a flood plain, the soil near the river level is rich in clay sediments. The Copán craftsmen used this as an advantage by employing dark clay-rich river mud (barro) as their primary binder for constructing the earliest adobe structures. Barro was also used as the complementary infill when using these structures as the base for the construction of new structures at the Acropolis. Archeologists have found that the lowermost layers of the Acropolis are mostly made of barro, of which the stability is dependent on a minimum moisture content (Larios Villalta, 2018). Since the areas built with this material are deep and close to the water table, there is no risk of outside ventilation or drastic changes in the moisture content; thus, making this layer very stable and structurally sound.

Later levels of the Acropolis incorporate more masonry, i.e., stone rather than adobe, elements in the construction. Structures found at the upper levels of the construction phase were mainly built with masonry elements using volcanic green tuff from the Sesesmil ravine near Copán and a mixture of clay and lime as mortar (Turner, Johnson, Mahood, & Jackie, 1983). Furthermore, these structures show more variation in the materials that the Maya used to infill their structures, including construction debris and different soil types. Whereas the earliest structures were filled with barro before

building on top of them, it has been noted that the Maya used a new type of reddish soil as infill for later construction phases. This infill layer contains lower levels of clay combined with silt, sand, and construction debris that researchers have called *tierra café oscuro*. This infill material is relatively stable, but it has been noted that it crumbles when dry and loses cohesion if it becomes too wet (Larios Villalta, 2018).

After the 8<sup>th</sup> century A.D., a yellow sandy soil known as *girún* was incorporated within Temple 16, including to bury structures like Rosalila and to construct others. This material is known to be extremely loose and unstable. The instability of this material is assumed to be one of the causes of deterioration and collapse of Temple 16 exterior areas, such as the upper five terraces and most of the eastern side of the structure. To recap, this chapter provides both a historical context and qualitative descriptions of Copán construction materials to illustrate the cultural significance of Rosalila and an overview of its construction sequence, particularly related to changes in construction materials that impact its current state of preservation. A more detailed discussion of the engineering properties and distribution of these soil layers are provided in Chapter 3.

## **2.2 Archaeological Tunnels beneath Temple 16**

### **2.2.1 History of Archaeological Tunnel Excavations in Copán**

Given the multi-layered construction methodology in the Acropolis at Copán, much of the city's invaluable history and culture comprises superimposed structures with temples that were built over four centuries and extend beneath the present-day surface. Because of the multiple sequences of construction, archeologists and researchers worldwide carried out excavations beneath the Acropolis by building a system of

underground archaeological tunnels over the years (Figure 2.9). These tunnels were built by different expedition groups over time. While the archaeological nature of these tunnels necessitated that all groups excavate by hand, each group had a different approach to stabilizing their tunnels to prevent collapse.



Figure 2.9. Plan view of the Copán Acropolis with sketch of archaeological tunnels  
(Larios Villalta, 2018).

There has been a total of eight primary archaeological excavations that have shaped the existing system of archaeological tunnels beneath the Acropolis. The Peabody's C.A. expedition made the initial excavations on the Acropolis at Copán at the beginning of the 1890s, which the Carnegie Institute of Washington later resumed during the 1930s. This first expedition showed researchers a glimpse of the elaborately layered architecture hidden inside and under the structures of the Acropolis (Fash & Agurcia

Fasquelle, 2005; Fash, 2001; Gordon, 1896). The increasing archaeological discoveries related to emerging tunneling excavation techniques in other Maya and Aztec sites around Mesoamerica led to an increase in the interest in expanding the archaeological tunnels in Copán by the second half of the 1970s. In 1977 the Proyecto Arqueológico de Copán (Copán Archaeological Project) or PAC 1 led a new tunneling operation known as Operation 1 on the east side of the Acropolis (Baudez et al. 1983). This archaeological project was in charge of continuing the exploration of the early Acropolis with tunnels. A decade later, the Northern Illinois University (NIU) directed a new operation to study the Hieroglyphic Stairway and Temple 26 in 1986. In 1988, the Proyecto Arqueológico de la Acrópolis de Copán (Copán Acropolis Archaeological Project) or PAAC was established and continued expanding the tunnel system to explore the inside of Temple 26 and Temple 16. Since 1996, different groups of archeologists from the Copán Association, University of Pennsylvania and Harvard University have led various tunnel excavations in conjunction with the PAAC to explore deeper parts of Structure 16 and the Hieroglyphic Stairway (Bell et al. 2004; Sharer et al. 1992). By 2003, a total of 4 km of tunnels were present; however, the total tunnel system has since expanded on a smaller scale, especially because of the exploration of the Oropendola Temple by Ricardo Agurcia in 1989.

### **2.2.2 Tunnel Stabilization Practices**

While the excavated tunnels beneath the Acropolis have allowed unique discoveries and a better understanding of Copán's history and culture, the tunnels have brought increasing concerns related to their stability and safety and their influence with

the increasing cracks that can be noticed around the unburied sections of the underground structures. Furthermore, opening buried structures to the outside environment via upper tunnels has exposed them to varying weather cycles and pollution that has accelerated their deterioration. The major stability challenge for tunnel excavation and maintenance has been the poor and unstable infill material surrounding them. Most of the tunnels are excavated through the reddish-brown infill material (known as *tierra café oscuro*) and the loose yellow sand (known as *girún*) that are highly unstable and depend on the moisture conditions that surround them. This property has led to the sudden collapse of tunnel sections during and after excavations. This is a safety concern for the researchers who visit the site and use the tunnels for their studies. On the other hand, the nature of these infill materials and the heavy rainy seasons that are typical in the region have also led to constant water intrusion that, in the best case, floods certain tunnel sections that make certain areas inaccessible for researchers due to tunnel inundation. The various tunnel operations used different approaches to stabilize their tunnels using different consolidation materials to address these problems.

The stabilization methods that different researchers along the tunnel system used mainly differ with the choice of stabilization material they use and its impact on its surroundings. In 1942, Gustav Stromsvik stabilized the first tunnels below Temple 11 by widening their cross sections and using masonry walls and arches to support the loose infill material. His masonry supports were built with a mortar with a high percentage of Portland cement that was able to effectively support the surcharge loads (Stromsvik, 1946). However, archeologists have found Stromsvik's work problematic since the



masonry elements were built by trying to imitate surrounding Maya architecture, making it difficult to distinguish from the original buried structures. Furthermore, the Portland cement mixture has been a problem since it blends with the volcanic tuff used by the Maya, making it difficult to remove and causing efflorescence, or white deposit of minerals and salts due to interaction with underground water and moisture, on the concrete surfaces and its surrounding areas.

Several debates have been made regarding whether backfilling or looking for ways to stabilize tunnels are the best approaches to ensure public safety and heritage preservation. Over the years, many tunnels were “cancelled” (backfilled) or “consolidated” (stabilized) as soon as they were excavated due to their high instability. Many tunnel excavations have adopted an approach similar to Stromsvik’s for immediate tunnel stabilization by removing one meter of infill material from both sides of the tunnels (when permitted by surrounding architecture) and consolidating it with a special mortar mixture with a lower cement content. The mortar formulas used on each project vary from one another, but most restoration work uses 6 parts of sand, 4 parts of earth, 2 parts of lime and 4% to 10% cement depending on the severity of the surrounding conditions (Lacombe, Fash, & Fash, 2020). In an effort to minimize the impact of cementitious mixtures to surrounding architecture and maximize the usage of native materials, a similar recipe with 0% cement but with more lime content has been used for recent stabilization work (Lacombe, Fash, & Fash, 2020). However, in some tunnels below Temple 16, a harder cement material has been used in conjunction with iron rebar to build support beams and columns that are starting to crack and contaminate

surrounding areas with metal corrosion. Other structural elements have been placed in random tunnel locations that temporarily prevent tunnel collapse, but their efficiency remains uncertain.

### 2.2.3 Current State of Tunnel System and Related Structural Problems

Currently, 47% of all tunnels have been stabilized with mortar mixture, lime, mud, and river stones, and 18% have been backfilled using barro and river stones (Lacombe et al., 2020). The remaining 35% of tunnels have not been consolidated nor backfilled. The presence and influence of the tunnels on their adjacent buried structures also have a major impact on the overall stability and preservation of these. Vertical and horizontal cracks have been observed on the walls of buried structures that have been exposed by the excavated tunnels (Figure 2.10). Lacombe et al. (2020) postulate that the cracks are primarily due to exposure to varying temperature and wetting cycles.



Figure 2.10. Cracks observed in exposed walls (Lacombe et al., 2020).

The variable consolidation materials used for tunnel stabilization and the proximity of tunnels to each other are accelerating stucco deterioration and tunnel instability or collapse during the rainy season. Tunnels stabilized with a hard and dense concrete mortar tend to be impermeable to water, so the concrete consolidation material does not allow water infiltration into the tunnel cavity. However, this creates another problem for surrounding tunnels that are not consolidated or consolidated with weaker material. Water accumulates around the impermeable layer of the consolidated tunnel, which causes pressure to build up around this area. In some cases, water pressure differential and erosive properties cause localized cracks and material failure of the consolidation concrete mixture. In other cases, the pressure differential affects neighboring tunnels with different stabilization conditions. Because some of these neighboring tunnels were excavated next to stucco or architectural detailing, the built-up water pressure can reach and infiltrate through the stucco and facades that are invaluable historical importance for this site (Figure 2.11). Finally, in cases where the neighboring tunnels have not been consolidated or do not have any stabilization means, the built-up pressure from the densely consolidated tunnels causes water to quickly infiltrate into these tunnels due to the pressure differential, which triggers their collapse (Lacombe, 2017).

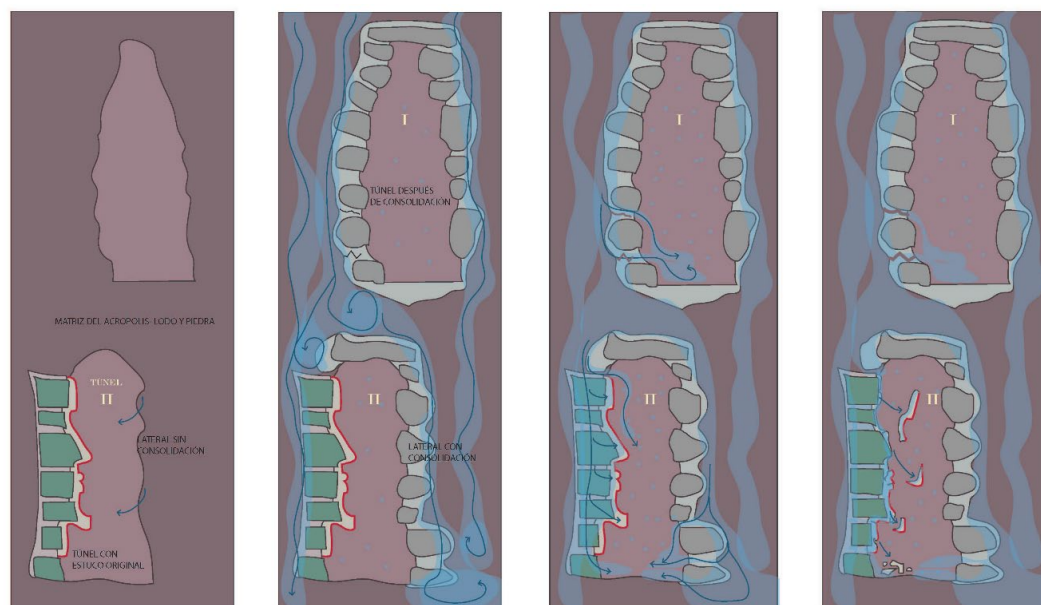


Figure 2.11. Sketch showing the impact of water flow in stabilized tunnels (*Lacombe, 2017*).

## 2.3 Current Research Work and Conservation Studies on the Copán

### Acropolis Tunnels

As discussed in the previous sections of this chapter, the archaeological tunnel system that lies beneath the Copán Acropolis has enabled archaeologists to collect and analyze invaluable data to formulate interpretations about ancient Copán and bringing a unique understanding to broader Maya culture, architecture, and religion. However, the combined effect of excavating into an archaeologically sensitive area and disrupting the previously established load paths through the artificial infill layers has brought preservation problems and challenges over the years. Besides the issues noted in Section 2.2, archeologists and other researchers have noticed additional tunnel-related problems, such as biological threats and stucco deterioration due to microbial invasion from the

external environment. Environmental hazards such as seismic events, hurricanes, or heavy storms due to the site's geographical location have also been a concern, particularly after Hurricane Mitch in 1998, and more recently in the aftermath of back-to-back Hurricanes Eta and Iota in 2022. To find and refine a more comprehensive set of policies for tunnel management regarding stabilization and backfilling efforts, the Copán Association, in conjunction with the Instituto Hondureño de Antropología e Historia (IHAI) and other local and international entities such as Harvard University and The Santander Program have come up with The Long-Term Conservation Plan of the Copán Acropolis Tunnels. This program aims to create better documentation strategies for the tunnels in three dimensions and continue the dialogues and research about ways to preserve better the exposed stucco and structure sections that the tunnel excavations over the years have exposed.

### **2.3.1 3D Mapping of the Acropolis and Archaeological Tunnels**

One of the main goals of the current Long-Term Conservation Plan is to be able to generate 3D documentation of the excavated tunnels that can help to make better conservation decisions as well as to have an interactive visualization model for identifying potential problems and for keeping a record of how the tunnel system changes over time. Even though the tunnels have been documented before via 2D drawings, there is an increasing need for updating to 3D documentations of the tunnels that is high-fidelity of the tunnel geometries and orientations, as well as geo-referenced. This 3D data provides more accurate measurements in sections of interest allowing archaeologists, conservators, and others to better understand the surrounding conditions of the tunnels.

The first maps of the exterior of the Acropolis were made by Galindo (Galindo, 1836; Hohmann & Vogrin, 1982) and later expanded by Stephens and Catherwood during the 1840s (1841). The drawings of the exterior gained more detail after Gordon (1896) and Stromsvik (1947) published maps at a scale of 1:1500. During the late 1970s and early 1980s, the Copán Archaeological Project (PAC 1) directed the earliest systematic archaeological surveys within the valley. During the 80s and 90's, the Copán Acropolis Archaeological Project performed surveying expeditions on the Acropolis tunnels, leading to about 5,000 drawings produced with total station technology. These drawings were combined with the knowledge of the tunnels of Fernando López to make the first 2D maps of the archaeological tunnels below the Acropolis. Between 2015 and 2018, these drawings were updated by López and Larios to reflect the current state of the tunnel system.

With the advent of modern surveying technologies such as remote sensing and photogrammetry, there has been an increasing interest in digitizing sections of the Acropolis with invaluable historical relevance. Hohman and Vogrin (1982) were the first to employ photogrammetric techniques to acquire 3D data of the Copán Acropolis. Several years later, in 1995, Hohmann (1982) was the first to use photogrammetry for the 3D reconstruction of excavated buildings at Las Sepulturas. Richards-Rissetto (2007, 2010) digitized and georeferenced the drawings made by PAC 1 and combined them with more updated information to create the first GIS dataset of the entire Copán Valley. Given the great success of creating 3D documentation of the Acropolis and its neighboring areas, researchers have tried to reproduce these results by creating 3D

models of the Acropolis tunnels. The first attempt was performed by Lacombe and the Proyecto de Conservación, Educación y Desarrollo de Museos Arqueológicos de Copán (COEDMAC), which created 3D models of 1.4 kilometers of tunnels over two years by employing a total station surveying technique that was employed to map tunnels beneath the Pyramid of the Moon in Teotihuacan, Mexico. Lacombe and her team used a Topcon DS-205 robotic total station for shooting a detailed sequence of tunnel cross-sections every 2 or 3 meters along the length of a tunnel. They then used the processed points to create a final three-dimensional model in AutoCAD 3D. To ensure precision, a loop of benchmarks on the exterior of the Acropolis was measured and triangulated with original benchmarks established by the US Geographical Survey in 2001. Traverses of tunnels were built-off by taking this initial loop as a reference, but they were difficult to close given the nature of the tunnels with sharp corners and dead ends. The resulting 3D model (Figure 2.12) was the first one of its kind for the Copán Tunnels, which has been used to monitor the recorded tunnels and take measurements of their dimensions. However, given the challenges of ensuring precision due to instrumentation availability, i.e., total station, which limited 3D data acquisition and also experienced problems due to the high humidity of lower tunnels, the resulting model had alignment errors up to 11.60 centimeters or an average of 0.0006 centimeters per linear meter of recorded tunnel. This error level was considered acceptable for performing basic length and volume calculations and served as a critical starting point for subsequent work.

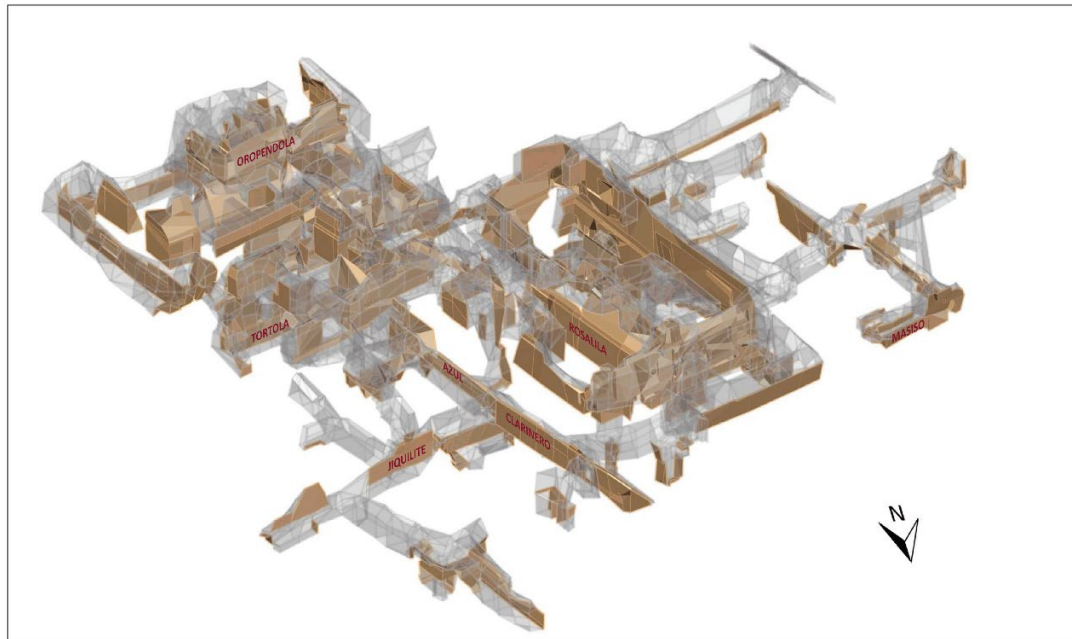


Figure 2.12. Screenshot of 3D model of tunnels beneath Temple 16 by Lacombe (2019).

### 2.3.2 Preliminary Structural Assessment of Excavated Archaeological Tunnels of Copán

Another critical task from the Long-Term Conservation Plan was to gain more insight into the stability conditions of the tunnels based on the available information regarding their geometric properties and location in space. The primary goal was to use collected surveying information on the tunnels to study their stability and causes of failure. In this sense, in order to provide a better understanding of the structural behavior of the excavated archaeological tunnels and a preliminary assessment of the stability concerns for formulating a plan of protective action, a research group led by Flora and Lorenzo (2021) conducted a structural analysis via a 2-D Finite Element Model of different typical tunnel cross-section geometries located below the Hieroglyphic Stairway



on Structure 26. In this study, they generated a general exterior geometry representing the Stairway. They came up with four representative tunnel cross-sections based on general observations and statistical analysis of the collected measurements on existing tunnels below this area of the Acropolis from the 3D survey. Due to the limited infill material information available from the site, this study assumed a homogenous infill mixture within the structure assumed to be filled by the girún infill only. By relying on unsaturated soil theory and a strength-reduction approach, several finite element simulations were produced in the Plaxis 2D software based on different cross-section scenarios and considering nearby-tunnel interactions and the effect of nearby buried structures. This preliminary study showed that most of their generated cross-sections would only allow maximum saturation levels of 60% to 90% for proper stability, depending on the influence of nearby tunnels and tunnel geometry.

## **2.4 Finite Element Analysis for Cultural Structures**

Analyzing a complex system such as Temple 16, Rosalila, and archaeological tunnels requires a comprehensive method for modeling and simulating complex geometries and loading cases. Since its modern conception during the first half of the last century, the finite element method has been a powerful tool used across different engineering disciplines for studying and approximating the behavior of physical systems without the need to solve nor establish a set of partial differential equations that describe them (Cook et al., 2001). With the arrival of modern and more robust processors and hardware, this powerful method has become the preferred choice by industry and researchers for performing engineering simulations to design and study systems in a field

known as computer-aided engineering (CAE). In the field of structural engineering and cultural heritage preservation, the finite element method has proven to be a crucial tool for analyzing historic structures with unique architecture and load transfer mechanisms that differ from how modern societies build and design their infrastructure (Wood et al., 2017). The robustness of the finite element method allows the study of systems with complex geometries. Therefore, this analysis technique has become an important tool for studying historic structures with unique architectural features that contribute to the overall structural response. Researchers have used this feature and current finite element analysis (FEA) software package capabilities to model and analyze complex historical sites worldwide.

Finite element analysis (FEA) for cultural heritage applications has been mainly used to investigate how historic structures or their components can transfer loads due to their weight and how the current load path mechanism might be causing their deterioration. One of the earliest uses of FEA for historic structures is the case of the Roman Parthenon made by Mark and Hutchinson (1986), which was performed to understand the structural behavior of the dome and the supporting cylindrical walls under the action of gravity. They used the current knowledge of the dome's architectural geometry to create a representative meridional cross-section of the system simplified from architectural details. This geometry and the knowledge of material behavior were used to create a characteristic finite element model for the analysis in which its resulting stress concentration patterns matched with observed cracking patterns of the structure. A similar 2D simplification approach as the one used by Mark and Hutchinson was also

utilized by Brune and Perucchio (2012) for the study of the structural configuration of the vault system and surrounding arches of the Great Hall of Trajan's Markets (Rome, Italy) under the action of the roof and self-weight gravity loads. Finally, a more recent and more sophisticated analysis was the case study of the Santa Maria Novella Church in Florence, Italy, conducted by Beheshti (2015). For this case, they digitized the historical set of drawings of the structure and combined them with on-site survey measurements to generate a 3D geometry model of the structure. Like the Parthenon case, this model was used for a finite element model that could predict the stress concentrations where cracking patterns were occurring in real life.

Finite element models have also been generated for studying historical structures under dynamic loading. One example is the seismic assessment performed in a medieval masonry tower in Northern Italy made by Milani et al. (2012). For this case, the 3D geometry of the structure was extracted from an already generated modern set of plans used for building the 3D model. During this study, a non-linear material formulation with the feature of modeling masonry damage and collapse was used to perform non-linear and limit static and dynamic analyses of the structure subjected to pre-recorded seismic loads to study its behavior and safety performance. The obtained modal frequencies and dynamic stresses and displacements were compared with theoretical approximations and local safety guidelines to validate the structure's safety, which was deemed appropriate.

In investigations of underground and earthen historical structures, the finite element method has also been a powerful tool for understanding and assessing the current conditions of underground structures exposed to vertical and horizontal soil and seismic

forces. One example is the study of the Pantokrator Cistern in Istanbul, Turkey, performed by Ustundag et al. (2012) where a 3D finite element model was created based on available historical information and site measurements. The FEA model was developed and used to study the system's performance under various heights of overlying soil infill and the action of pre-recorded local seismic events by also considering a proposed retrofitting system for repairs. The study suggested removing all the soil infill from the top of the structure as a mitigative measure, since a high level of damage was detected. Finally, FEA has been used recently to study the underground catacombs in Alexandria and their performance against seismic threats. Based on available historical information, Hemeda (2022) developed a 2D finite element model of the catacombs to assess their seismic performance with and without a proposed polymer anti-seismic piling technique for seismic isolation. The simulation results and site observations confirmed significant site deterioration due to the nature of the surrounding limestone rock material against seismic hazards in both cases.

## **2.5 From lidar to FEM for Cultural Applications and Underground Structures**

When trying to perform a representative analysis of the current state of historical structures, the amount of information available regarding structural geometry and material behavior is crucial for an accurate assessment. However, documentation of these structures' overall geometries is generally limited. To address this, Light Detection and Ranging (lidar) technologies have been extensively used by the research community in the past decade, given their ability to capture variable geometries and terrains into a point

cloud (Remondino F. , 2014). Lidar is an active remote sensing technique that utilizes either continuous, modulated or pulsed laser light reflections to determine the distance to surfaces in the scanner's field of view. This allows capturing the 3D geometry, color, and intensity of the object of interest. Therefore, lidar has recently become a powerful tool for extracting geometric information and developing models of historical and modern-day structures to analyze their current state. This is achieved by using lidar to generate dense points cloud of a structure's surface that can then be used to generate a corresponding CAD model of the structure's geometry. The obtained digitized geometries can be used to generate Finite Element Models for detailed analysis and structural assessment. This is typically accomplished by importing digitized CAD geometries into an FEA meshing platform or FEA preprocessor.

### **2.5.1 Lidar and FEA for Cultural Heritage Applications**

Lidar, as well as photogrammetry techniques, have already been widely used by archeologists and researchers in the field of cultural heritage preservation for more accurately documenting the complex geometries of archaeological structures (e.g., Ebolese et al. 2019, Saperstein 2016). Given this increasing trend in acquiring 3D archaeological data using remote sensing, researchers have begun using the resulting point clouds to generate finite element models of these ancient systems to understand their structural behavior against the environmental threats surrounding them (Hemeda, 2021). By incorporating such analyses into management practices, communities can make more informed preservation decisions that will help preserve cultural heritage for future generations.

The earliest cases of lidar-based 3D and Finite Element models are preliminary studies where high-fidelity geometries were needed to approximate the structural behavior of cultural heritage structures. The general approach for model generation was manipulating the generated point cloud of the system to extract relevant dimensions and measurements of the structure that were subsequently used to manually build a CAD model. One of these earliest studies was the case of the surrounding walls of the city of Montagnana, Italy. Guarneri et al. (2005) combined different surveying techniques such as reflectorless total stations, GPS local network setup, and a Leica HDS 3000 laser scanner to acquire and register a point cloud of the structure. With this data, this research team extracted relevant cross sections of the wall to create high-fidelity 3D geometry and a finite element model that they used for gravity load and lateral wind load analysis. Another early lidar-based structural assessment case was the Cernadela bridge in Galicia, Spain. In their study, Izabela et al. (2009) used lidar techniques via Rigel LMS-Z390i equipment and ground penetrating radars to capture the complex geometry of this bridge. Once the point cloud was generated, cross-sectional slices of the bridge point cloud were used to extract relevant geometric information to develop a representative CAD model. This CAD model was then exported into an FEA software package, where it was meshed and calibrated to conduct modal and sensitivity analysis to determine the impact of the variation of Young's modulus in the fundamental frequencies and dynamic response of the bridge.

Another recent study that uses lidar-based geometries for cultural heritage damage assessment investigated the Nyatapola Temple in Bhaktapur, Nepal (Wood et al., 2017).

Unfortunately, this was the only structure of its kind that remained in this area after a  $M_w$  7.8 earthquakes, pre- and post-earthquake making it imperative that researchers acquired highly accurate data for use in documentation and analysis. To do this, lidar point clouds were collected using ground-based lidar scanning. These point clouds were used to manually extract relevant cross-sectional dimensions of the structure along its height. These data were used to manually develop representative FEA models. Finally, these models were used to study the fundamental structural frequencies and the overall structural response of the structure when subjected to the recorded ground motion. The modeling results matched the post-earthquake damage observed and theoretical approximations and thus were used for recommending ways to reinforce the structure against future seismic events.

Other uses of lidar for 3D and FEA model generation were refined with the latest advancements in CAD software technologies. Barazzetti et al. (2015) used a Faro Focus 3D laser scanner to compile a dense point cloud of the Castel Masegra (Sordino, Italy) to create a BIM (Building Information Model) geometric model. Their study illustrated that BIM geometries from lidar high-fidelity information do not need to undergo an exhaustive simplification process for finite element analysis. To do this, they imported the 3D point data collected on-site imported into the BIM software Revit. In Revit, they used the software's native capabilities to create vectorized non-uniform rational B-spline (NURBS) surfaces that made up the system's geometry. This approach generated a high-fidelity finite element model in the same software package to conduct a static analysis that could predict cracking and high-stress zones that would match with site observations.

Finally, because of these, and other, promising results and implications of using lidar for high-fidelity FEA models for structural assessment, researchers are exploring how to develop software that generates FEA models using simplified lidar point clouds, given computational challenges with employing raw 3D point clouds. One of these cases is the study of the San Felice Sul Panaro Fortress near the city of Modena, in San Felice Sul Panaro (Italy). After being hit by the Emilia Earthquake in 2012 that had two consecutive peaks ( $M_W = 5.86$  and  $M_W = 5.66$ ), the local municipality performed several surveying operations on the damaged structure using lidar and other photogrammetry techniques to acquire and create point clouds to conduct studies to preserve its integrity. To compare CAD-based FEA mesh generation methods with an experimental algorithm that generates a FEA mesh from a simplified point cloud (known as CLOUD2FEM), Castellazzi et al. (2015) generated FEA models of the principal tower of the fortress (known as Mastio). This team used the surveying information collected from the site with FARO Focus 3Dx330 laser scanners and a total station Trimble S6. As part of their processing, they first simplified the initial point cloud on the open-source mesh processing system MeshLab by using an algorithm that populated a new dataset via point sampling dictated by a Poisson-disk distribution. To test the efficiency of their software, they created two FEA models based on this lidar data: one generated via CLOUD2FEM and another generated via CAD methods by collecting geometric information of the point cloud at critical slices or sudden geometric changes. They used both models to cross-validate a frequency analysis of the structure for



determining the natural frequencies of modal shapes. The results from both models differed by less than 4%, which was deemed acceptable.

### **2.5.2 Lidar and FEA for Underground and Earthen Structures**

One of the main challenges in accurately surveying or characterizing underground structures, such as tunnels or earthen structures, is the inability to accurately capture the overall geometry of this system with traditional surveying techniques. Because, by definition, tunnels are negative spaces that run through a soil matrix, conventional surveying techniques are not capable of accurately capturing the nature of complex tunnel systems without allowing for a significant margin of error. With lidar, it is possible to capture high-fidelity geometry of underground structures that can also be used for generating finite element models. A notable example of lidar-based finite element models for earthen structures is the case of the Huaca de la Luna archaeological site in Trujillo, Peru made by Chácara et al. (2014) where lidar point clouds of the unearthed structures were collected and used for updating the existing 3D geometry of the site and for the generation of finite element models of unearthed columns, adobe walls and the whole archaeological site for gravity and seismic loads analysis. Similarly, another current example of lidar-based FEA models for underground excavations was the case for Kartchner Caverns in Arizona made by Kemeny and Chun, where they used field-collected lidar point clouds to create a high-fidelity 3D finite element model for stability analysis (2017). The findings of this study matched field observations and were grounds for future stabilization work.

## 2.6 Scope and Contribution

Temple 16 and the Copán Acropolis are cultural and historical treasures for the people of Copán, Honduras, and the world. In the process of archaeological discovery, an entire archaeological tunnel system has been excavated through the Acropolis structures, including Temple 16. Because of the different excavation and tunnel stabilization techniques that have been used over the years, some of the Copán archaeological tunnels pose a danger to both researchers as well as the buried structures that the tunnels expose, such as Rosalila. The 3D CAD model of Temple 16 tunnels, developed by Lacombe and her team (2019), had alignment errors up to 11.6 centimeters due to limitations in their surveying technique. In addition, this model did not fully capture the entire tunnel system and only represented the tunnels excavated during certain operations. Therefore, there is a need for accurate 3D documentation of the archaeological tunnel system to facilitate studies on their stability. While Pires et al. (2021) offered a preliminary assessment of the stability of generic tunnel sections below the Acropolis, the analysis did not account for the complex 3D geometry of the tunnels nor how the tunnels are actually distributed in space. Therefore, this thesis aims to conduct a detailed structural assessment of Temple 16, accounting for the complex 3D tunnel system and the impact on Rosalila, to understand the leading causes of tunnel collapse and structural deterioration. This is intended to inform historic preservation for the site in terms of tunnel cancellation (backfilling) or additional consolidation. To accomplish this, lidar and finite element analysis techniques are used to accurately develop and analyze 3D models of Temple 10L-16, Rosalila, and their surrounding archaeological tunnels.

First, the techniques and processes used for developing the system's 3D CAD geometric models will be explained in CHAPTER 3. This section includes the lidar instruments and methods for collecting and processing data for creating point clouds. This chapter then dives deeper into the techniques used to extract geometry information from the point clouds to create a high-fidelity CAD geometry used for Finite Element modeling. To ensure accuracy in the analysis results, finite element model parameters are then calibrated and validated in CHAPTER 4. The calibrated model is then used to evaluate the stability of the tunnel system and Rosalila in CHAPTER 5. Finally, analysis results are interpreted and further discussed in CHAPTER 6, where further actions for the historic preservation of this site will be addressed.

## CHAPTER 3 – GEOSPATIAL DATA MODELING

### 3.1 Chapter Overview

The overall objective of this thesis is to conduct a structural assessment of Copán's Temple 16, its complex tunnel system, and the buried Rosalila structure. This chapter outlines the methodology followed to develop high-fidelity finite element geometry models of Temple 16, Rosalila, and the archaeological tunnel system, which leverages lidar data to generate CAD geometries that are exported and transformed into a Finite Element Model (Figure 3.1). As such, lidar data collection and processing will be detailed, including segmentation and registration. Vectorization is then employed to extract relevant geometric data for reconstructing Temple 16's geometry in CAD.

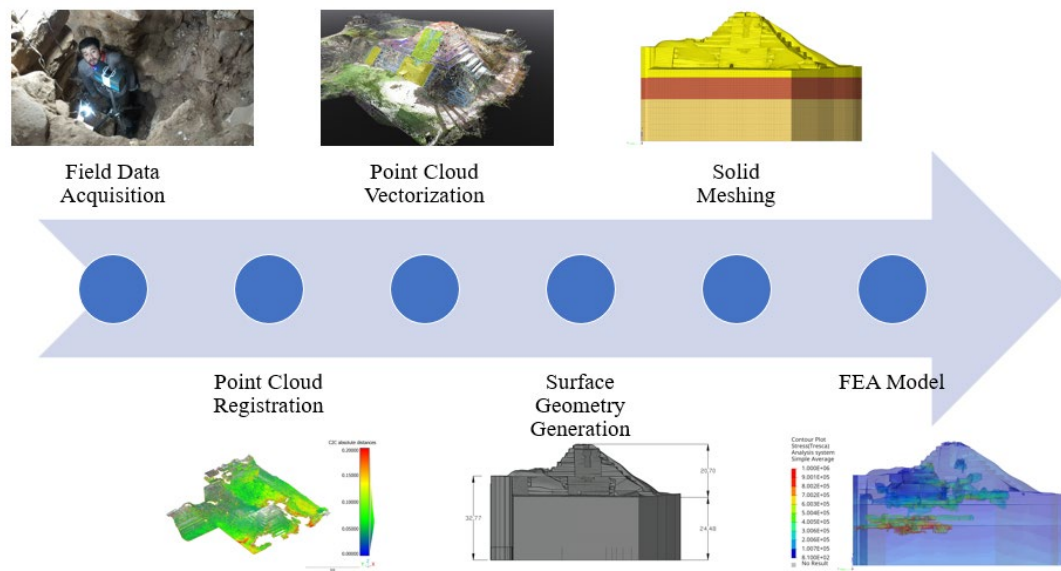


Figure 3.1. General FEA model generation pipeline.

## **3.2 Data Acquisition and Point Cloud Generation**

### **3.2.1 Lidar**

#### **3.2.1.1 Lidar Data Collection**

Lidar data of the exterior of Temple 16 and its underlying archaeological tunnel system was collected by a group of local and international researchers under the University of Nebraska-Lincoln's Richard Wood during three data collection campaigns between January 2020 and August 2022 (Figure 3.2). Additionally, Rosalila's Replica that was built at the Copán Sculpture Museum was also scanned in order to capture relevant geometric information for later modeling of this structure. Table 3.1 shows a summary of the instrumentation and the lidar type and parameters that were used for collecting information of the archaeological tunnels (interior scans), exterior of Temple 16 (exterior scans), and Rosalila's Replica. Similarly, Table 3.2 summarizes the number of scans collected per year and per location. A total of 1,684 scans were taken among interior (1,468), exterior (179) and replica (37) scans during all missions.

The majority of the interior scans were intended for tunnel mapping and to facilitate finite element model generation; however, a subset of the scans was intended to document certain buried structures in high-resolution for conservation purposes. The scans for tunnel mapping were conducted at lower-resolution and without color to expedite data collection and minimize occlusion. These scans were collected at roughly 2 meters spacing along straight tunnels and at much closer spacing around corners and near turns. Due to the tunnel geometry, mapping scans were collected at only one elevation

near the approximate center of the tunnel cross-section. In contrast, the scans intended for high-resolution documentation were collected at several elevations and at close spacing that was defined to ensure adequate coverage of the architectural features of the buried structure. For the collection of interior scans, the usage of a telescoping tripod was critical for data collection in tunnel areas where access for data collection was challenging such as tall shafts or wells that connect tunnels (Figure 3.3& Figure 3.4).



Figure 3.2. Lidar scanning of Temple 16 during site expedition on the summer of 2021.

Table 3.1. Summary of lidar instruments and collected datasets.

Scanned Location	Resolution Type	Scanner Range	Resolution <sup>(1)</sup>	Quality	Color Type	Time Duration (minutes/scan)	Mount Height (cm)	Lidar Type
Interior Scans	Mapping	360 Degrees	1/8	4x	No Color	2	75	FARO s350
	High-Resolution	360 Degrees	1/4	4x	HDR Color	16	Varies	FARO s350
Exterior Scans	High-Resolution	360 Degrees	1/4	4x	Standard Color	13	150	FARO x130 and FARO s350
Rosalila Replica	High-Resolution	360 Degrees	1/5	4x	HDR Color	12	150	FARO s350
		360 Degrees	1/5	4x	Standard Color	8	150	FARO s350
	Mapping	360 Degrees	1/8	4x	No Color	2	150	FARO s350

<sup>(1)</sup>:Resolution is defined by FARO as the number of points in a 360-degree scan (in millions): 1/8, 11.1; 1/5, 28.4; 1/4, 44.4.

Table 3.2. Summary of number of scans collected per location and year.

Scanned Location	Resolution Type	Number of Scans				Total per Scanned Location
		2020	2021	2022	Total per Resolution Type	
Interior Scans	Mapping	204	317	583	1104	1468
	High-Resolution	42	320	2	364	
Exterior Scans	High-Resolution	20	159	-	179	179
Rosalila Replica	High-Resolution	-	25	-	25	37
		-	5	-	5	
	Mapping	-	7	-	7	
Total Number of Scans						1684



Figure 3.3. FARO s350 mounted on telescopic tripod for scanning interior tunnel areas.



Figure 3.4. FARO s350 mounted on telescopic tripod in inverted position for scanning exterior tunnel areas.



### 3.2.1.2 Lidar Data Registration

All lidar scans were preliminarily processed and locally registered with a custom built-up PC with 256 GB of RAM, dual Xeon 6130 Gold CPU, and dual NVIDIA GeForce RTX 2080 TI GPUs. Preliminary processing included point cloud filtering for dark, stray, and far points as well as colorizing of the point cloud where applicable. The iterative closest point algorithm was used to register all scans to a common reference frame. Point cloud processing and registration was initially done separately for mapping, exterior, and high-resolution scans. Due to the computational expense, the high-resolution scans were further sub-divided for processing based on individual walls or facades as well as by level and orientation. This processing and registration were conducted within the FARO Scene software. The registration process was iterative over the course of the many missions and required significant initial manual alignment and checking based upon recorded scan metadata regarding scan location. Due to the significant number of scans, registration was done in clusters, representing distinct loops and off-shoot tunnel sequences. The clusters were then registered to a single common reference frame to facilitate georeferencing, which is described in later sub-sections. To minimize the registration error, the exterior scans were incorporated in a closed-loop strategy to the interior scan data via 3 access tunnels (the tunnel near the west court (Tunnel 4), the hatch access point in the east court (Tunnel 46), and the tunnel near the Jaguar platform and northeast of Rosalila (Tunnel 21)). The final lidar-based point cloud was aligned with a mean registration error of 3.9 mm, with a maximum value of 34.8 mm at the exterior scans, where objects were transient. The highest mean point error was 18.5

mm. The registered point clouds were exported from FARO Scene for post-processing as individual .las files corresponding to individual scans.

### **3.2.2 UAS Data Collection and Point Cloud Generation**

UAS-based data was generated from 336 aerial images that were taken by a retrofitted DJI Mavic Pro 2 (Figure 3.5). Images were PPK geotagged (post-processed kinematic tagging) and processed in Pix4DMapper, a structure-from-motion implementation, for point cloud generation (Figure 3.6 & Figure 3.7). Images were georeferenced relative to a temporal base station, placed near the archaeological cut (east of Temple 16). The position of the base station was determined using the Online User Position Service (OPUS), with accuracies at the centimeter-level. Several checkerboard targets were placed throughout the site to serve as check points within the point cloud for validating the accuracy of the structure-from-motion. The checkerboard targets were also used to aid in registration of the lidar-based point clouds with the georeferenced UAS-based point cloud. This task resulted in a single point cloud (Figure 3.6), unlike the many individual point clouds that resulted from lidar.



Figure 3.5. DJI Mavic Pro 2 during UAS data collection.



Figure 3.6. Aerial view of UAS point cloud data of temple 16 and surrounding areas of the acropolis (scale in meters).

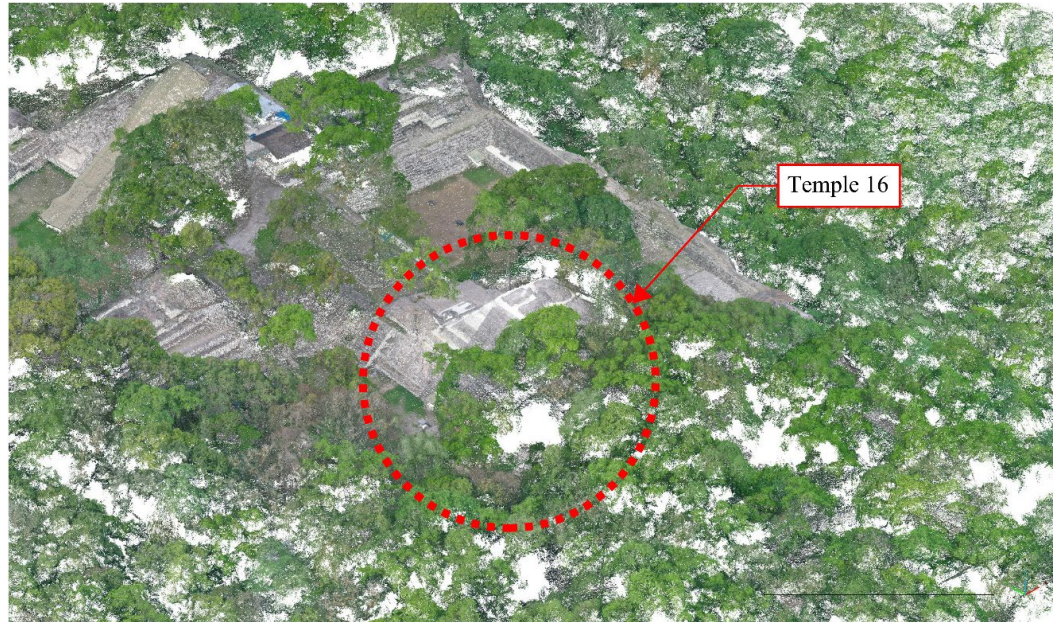


Figure 3.7. View from the southwest of Temple 16 and surrounding areas.

### 3.3 Point Cloud Data Processing

#### 3.3.1 Cleaning and Filtering

Due to the site's location, surrounded by dense vegetation, the exterior scans need to be segmented and cleaned from noise and significant vegetation. However, the primary vegetation that covers deteriorated areas of the structure caused occlusion in some areas. Given the overall size of the geometric data, the random location of deteriorated areas, and the need to store as much relevant geometric information as possible, the application of automatic cleaning filters was disregarded, and manual cleaning of the scans was selected as the preferred method. CloudCompare (2022), a software specialized in point-cloud manipulation, segmentation, and alignment, was used to manually segment the scans from undesirable vegetation elements and isolate areas of interest. Once the individual scans were adequately cleaned, they were merged to create a final lidar-based



point cloud for the exterior of Temple 16 and surrounding areas (Figure 3.8). Similarly, this process was repeated with the lidar scans collected from the archaeological tunnels that had to be cleaned from vegetation captured near the tunnels' entrance and from noise created by mirror reflections in the visitor's tunnel sections. CloudCompare was also used to clean and isolate Temple 16 and surrounding areas from the UAS point cloud for later registration processes (Figure 3.9).

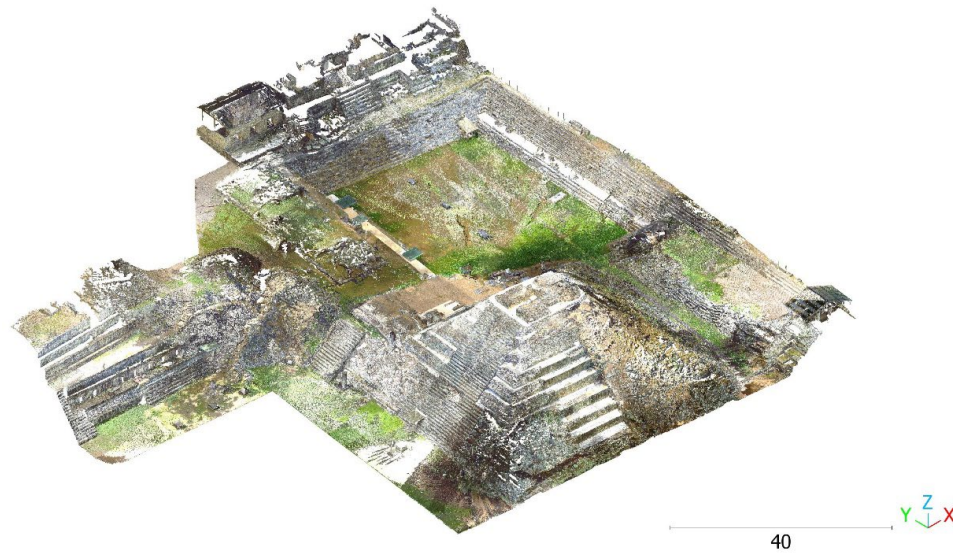


Figure 3.8. View from the southwest of lidar point cloud of Temple 16 after segmentation (scale in meters).

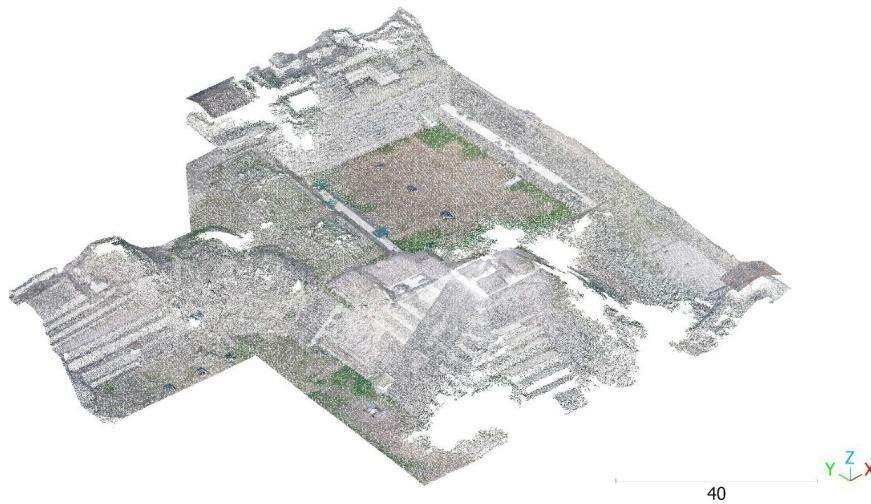


Figure 3.9. View from the southwest of UAS point cloud of Temple 16 after segmentation (scale in meters).

### 3.3.2 Coordinate Transformation

CloudCompare was also used for registering the lidar-based point clouds to the georeferenced UAS-based (or SfM-based) point cloud in UTM-16N coordinates. This registration relied upon the significant overlap between the merged exterior lidar point and the UAS-based point cloud. The overall registration process was divided into three steps: (1) global shift, (2) rough initial alignment, and (3) final registration.

The need to perform global shifts to georeferenced point clouds as part of the registration process comes from the precision storage limit that CloudCompare has. Because of the  $10^6$  to  $10^9$ -digit precision that the geo-referenced coordinates have, CloudCompare requires applying a global shift to point clouds with coordinate systems that are above  $10^5$  to ensure numerical stability and relative precision when computing the transformation matrices. This is because CloudCompare works under 32-bit floating

point values which only allow precision of around  $10^{-7}$  to  $10^{-8}$  (CloudCompare, 2019).

Therefore, CloudCompare provides the option of applying these shifts as either temporary (for cloud manipulation purposes) or permanent (for cloud alignment purposes), which are retained and used for scaling values as metadata.

A rough alignment between clouds was performed to align the point clouds in space preliminarily. This step was done by using the CloudCompare point picking alignment tool. This tool allows a point-based registration by letting the user roughly align two entities by picking at least four equivalent point pairs in both entities. The rough registration of the point clouds was performed by suppressing any scaling operations and only allowing rigid body translations and rotation.

As a final step, the point clouds are finely registered by utilizing the iterative closest point (ICP) algorithm available in CloudCompare, which is similar to that performed for the lidar-based scans in FARO Scene (Section 3.2). This operation assumes that the exact point correspondences between clouds are not known a priori but, rather, the entire or a significant percentage of the points are compared to minimize point-to-point distance via several iterations. Because of the nature of this algorithm, this process demands the compared clouds to be roughly aligned and with sufficient overlap. While the first requirement was achieved in the previous step, the overlap between clouds is usually unknown. To get better results, CloudCompare allows to adjust the expected percentage of overlap for performing the ICP operation, and it also lets the user adjust the expected final level of alignment precision by either adjusting the RMS difference between iterations or by adjusting the number of iterations performed by the algorithm.

Because of the size of the point clouds, the desired level of precision was achieved by trial and error by first approximating the overlap and by then adjusting the RMS difference to the maximum level permitted by the machine's computing capacity. Finally, the ICP registrations were performed by maximizing the number of random sampling points limit and enabling farthest point removal. The resulting transformation matrices were only allowed to perform rigid body operations and point cloud scaling was prevented for all datasets.

The lidar-based point cloud of the exterior of Temple 16 was aligned to the UAS-based point cloud using the UAS-based point cloud as reference since it was georeferenced in UTM-16N state plane coordinates (SPC). A global shift was applied to the UAS-SfM data to ensure relative precision. Because of the size of the lidar-based cloud and the significant difference in points densities, a clone of the lidar-based cloud was created and spatially subsampled by using a 10 cm radius for performing the rough alignment. Twenty-five point pairs were selected from both clouds by taking advantage of the sharp corners of the structure. By doing this, both clouds were roughly aligned with a registration mean square error (RMS) value of 12.844 cm, which is acceptable for a preliminary alignment. The final ICP registration was performed with a final overlap of 30% and a registration threshold defined by an RMS difference of  $5 \cdot 10^{-5}$ . This allowed a final transformation matrix with an RMS value of 4.4405 cm (Figure 3.10). It is clarified that this alignment represents the global alignment of the geometric data in UTM-16N coordinates, and the local accuracy of Temple 16's point cloud from the lidar maintains much higher accuracy (mean registration error of 3.9 mm).



The transformation matrices and alignment steps that were obtained from the alignment process of the exterior lidar-based point cloud with the UAS data were applied to the lidar-based point clouds of the interior tunnels. This process was possible since the interior point clouds were already aligned with the exterior lidar-based point clouds from the registration process performed in FARO (Section 3.2). Therefore, the process that was established for coordinate transformation of the exterior point cloud into UTM-16N coordinates was replicated for the final alignment of the interior archaeological tunnels. Prior to the alignment, interior clouds were partially cleaned by deleting exterior vegetation and overall noise (Figure 3.11 & Figure 3.12). The global shifts and transformation matrices that were previously performed in the exterior point cloud were applied to the interior point clouds. This process was initially performed with the interior point clouds that were collected in 2020 and 2021 (Figure 3.13), and it was later replicated after the addition of the data collected during the summer of 2022 (Figure 3.14 & Figure 3.15).

Finally, a similar process was used for aligning the replica of Rosalila (Figure 3.16) with the original. For this case, because only parts of the exterior of the original Rosalila are exposed in the tunnel system, these parts were adequately identified and isolated from the rest of the point clouds of the tunnels. The rough alignment was performed by equating some of the corner entrances of the original's first and third levels with the ones of the replica. A preliminary RMS value of 22.65 cm was achieved by doing this process. For the finer alignment, a Cloud-to-Cloud (C2C) distance comparison was run between the replica and the exposed parts of the original Rosalila in order to

determine adequately identify the overlapping parts. The resulting scalar field was utilized to filter out the parts of the replica that had an absolute distance greater than 20 cm from the original. The remaining parts were used to perform the final ICP registration of the replica with an overlap of 75% and an RMS difference of  $10^{-7}$ . The final transformation matrix allowed a final RMS of about 5.39 cm (Figure 3.17) which is acceptable considering the fabrication errors of the replica and the potential deterioration of Rosalia's exposed parts since the measurements for building the replica were taken. Finally, Figure 3.18 shows the general overlay of Temple 16 point clouds after alignment.

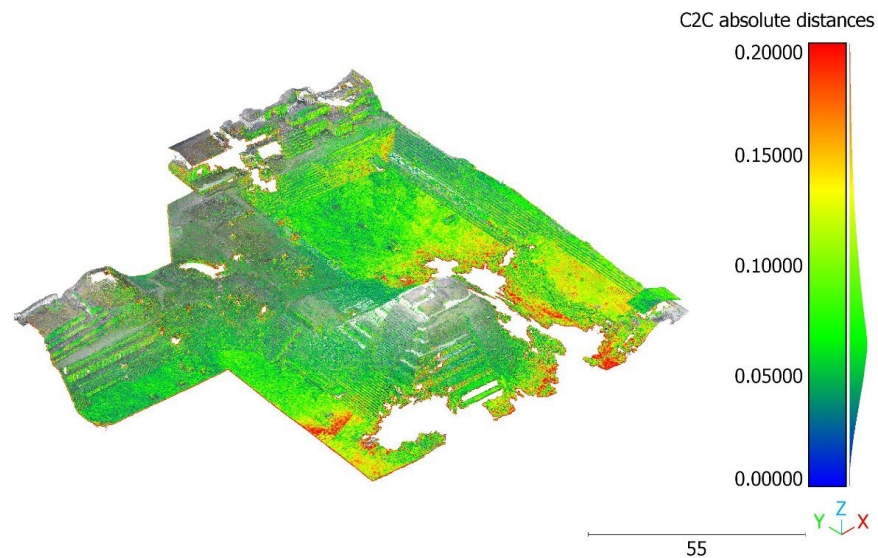


Figure 3.10. View from the southwest of cloud-to-cloud distance comparison between UAS and high-resolution point clouds of Temple 16 after alignment process (scale in meters).

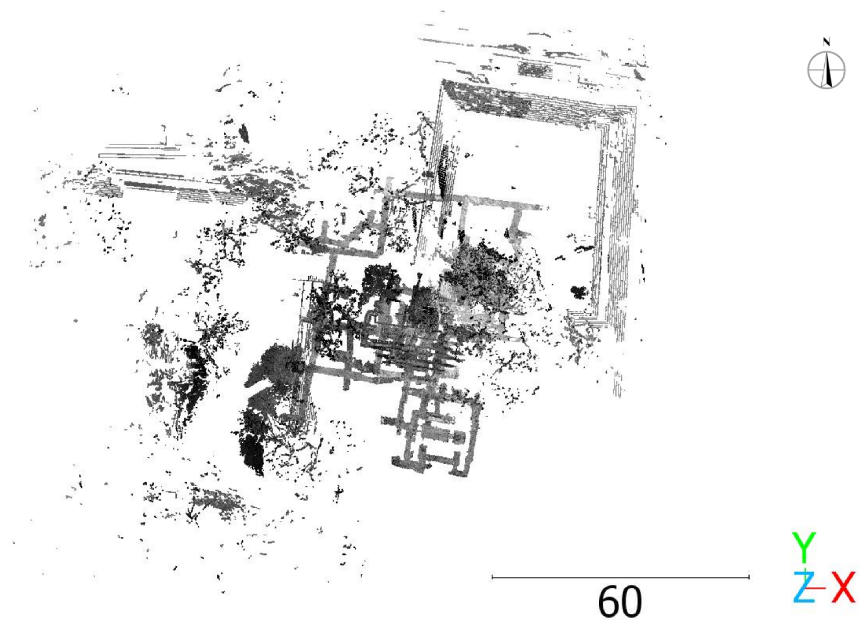


Figure 3.11. Aerial view of Temple 16 tunnels point cloud collected during the summer of 2021 (scale in meters).



Figure 3.12. View from the west of Temple 16 tunnels point cloud (collected during the summer of 2021) prior to segmentation and alignment (scale in meters).

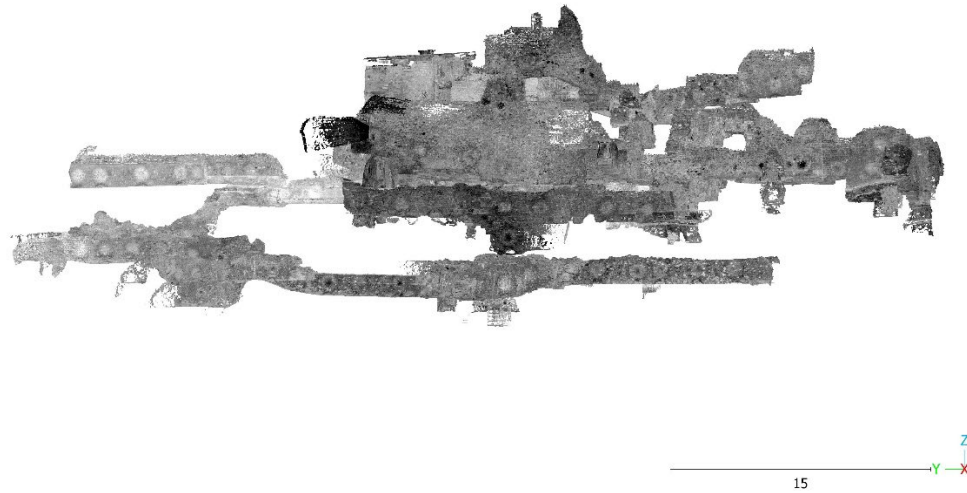


Figure 3.13. View from the west of Temple 16 tunnels point cloud (collected during the summer of 2021) after segmentation and alignment (scale in meters).



Figure 3.14. View from the west of Temple 16 tunnels point cloud after segmentation and alignment between 2021 and 2022 datasets (scale in meters).



Figure 3.15. Aerial view of Temple 16 tunnels point cloud after segmentation and alignment between 2021 and 2022 datasets (scale in meters).

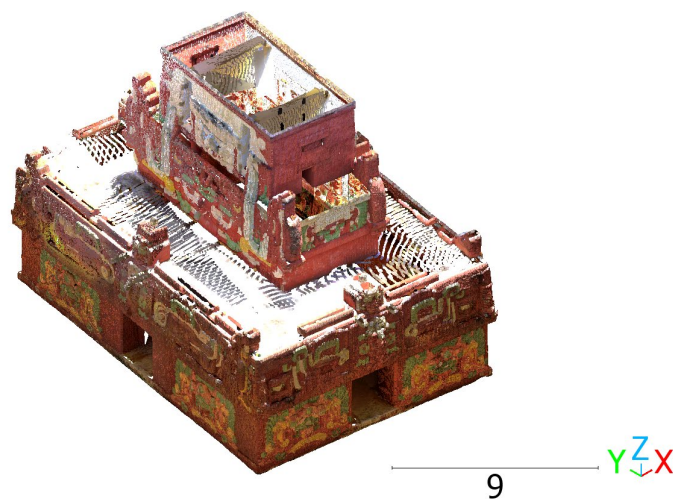


Figure 3.16. View from the southwest of Rosalila's replica point cloud (scale in meters).

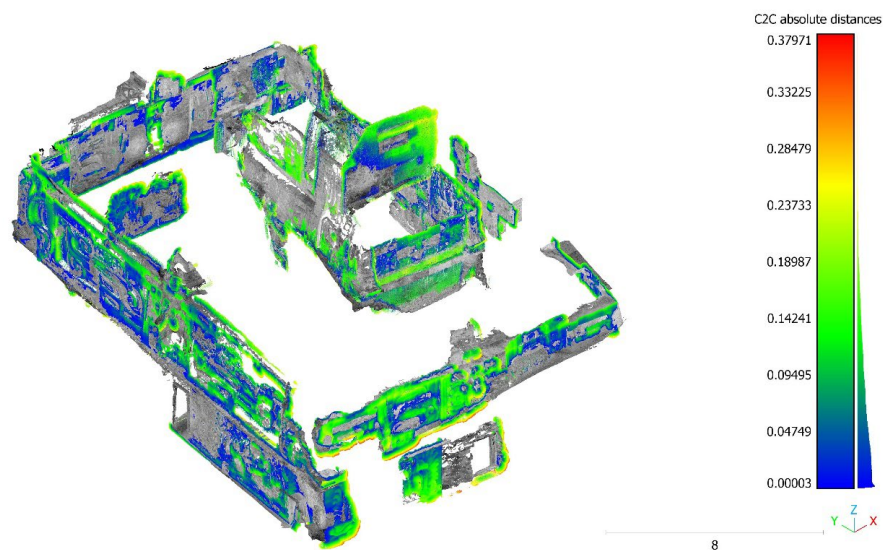


Figure 3.17. View from the southwest of cloud-to-cloud distance comparison between Rosalila's replica and exposed sections of original structure along the tunnel system (scale in meters).



Figure 3.18. Aerial view of final setup of Temple 16, tunnel system and replica's point clouds after alignment (scale in meters).

### **3.4 Geometry Vectorization**

#### **3.4.1 Vectorization of Temple 16's Exterior Point Cloud Data**

Several methods allow automatic geometry generation from a point cloud via surface meshing. As briefly explained in Chapter 2, these methods have been used for previous studies of more contemporary historic structures where the level of deterioration is typically not as aggressive as that observed in Temple 16. Because of the level of deterioration and the amount of remaining vegetation and occlusion in some of the areas of the point cloud, directly applying surface meshing algorithms for automatic geometry generation of the structures is not desired. This is because the resulting surface meshes will try to account for patches due to occlusion in the deteriorated areas, resulting in sharp geometries that are not desired for a Finite Element Mesh. Therefore, a manual geometry generation approach that selectively relieves some geometric features but keeps high-fidelity geometric information in others is necessary. In this sense, the point cloud vectorization method serves as an intermediate step for collecting relevant geometric point cloud data that can be used for rebuilding the desired geometries.

Vectorization is the process of converting a discrete set of points into a vector representation. For point cloud systems, this translates into using the recorded points to generate vertices and paths that can be used to create closed shapes (polylines) of a geometry of interest. These shapes can be exported into CAD software packages, where they can be used to regenerate surface geometries. Manual vectorization makes it possible to selectively pick relevant geometrical information and selectively relieve areas with sharp geometries by keeping a desired degree of accuracy. Furthermore, the



collected information keeps important global coordinates information of the points used so that the resulting geometry model is also geo-referenced. For the case of Temple 16 and its tunnels, this method allows the generation of a high-fidelity geometry model that is not compromised by the current structure's deteriorated features for later analysis.

Pix4DSurvey (2023) was used as the vectorization software tool for all the structures of interest.

Given the highly irregular geometric features of the exterior of Temple 16, interior and exterior corners were used as references for vectorizing the different levels of the temple and the stairs. Representative geometric sections were captured in the deteriorated areas to include their overall influence on the geometry, but they were simplified in most cases to avoid sharp features during the analysis. A final overview of the vectorized sections with the superimposed point cloud is shown in Figure 3.19 and Figure 3.20.

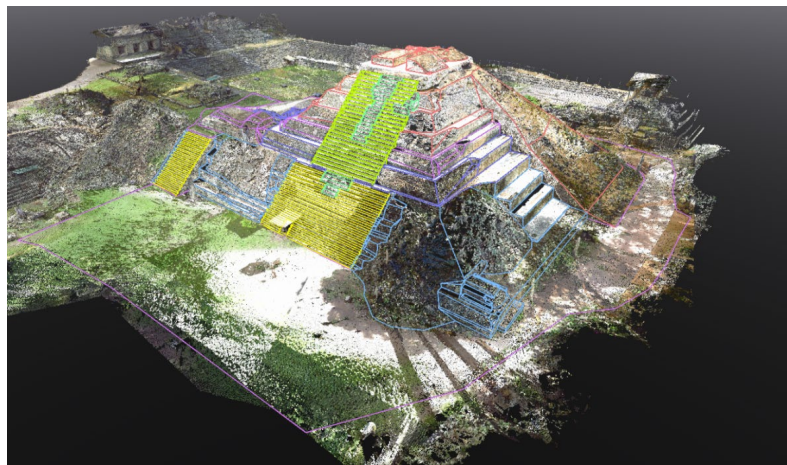


Figure 3.19. View from the southwest of Temple 16's point cloud with vectorized features.



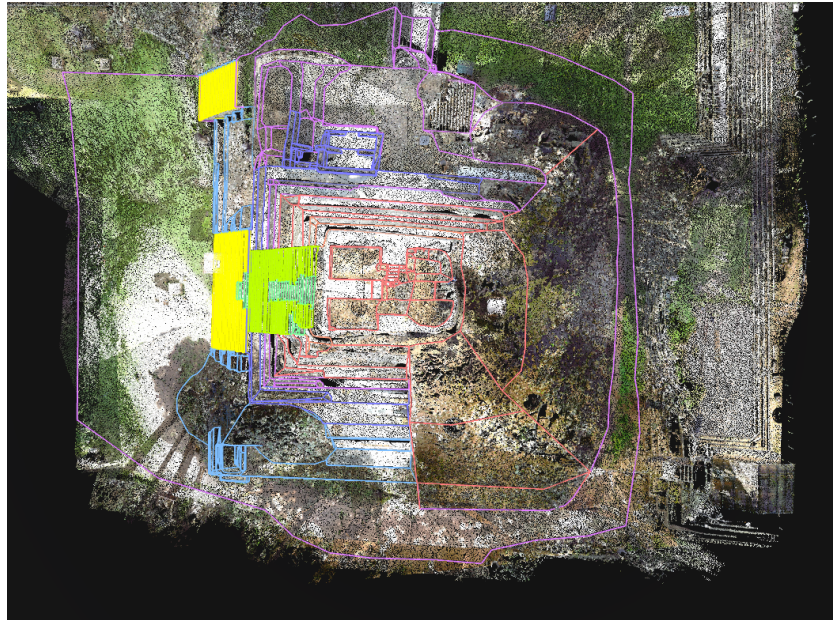


Figure 3.20. Aerial view of Temple 16's point cloud with vectorized features.

### 3.4.2 Vectorization of Interior Tunnels Point Cloud Data.

A different approach was used for the vectorization of the tunnels and the replica of Rosalila due to the different geometry. In the case of tunnels, their round nature and the global lack of sharp corners in their geometry do not allow an easy reference point selection to use for vectorization. Therefore, a slicing approach was selected where representative tunnel cross sections were sliced and extracted from the point clouds. The slices were strategically extracted from the geometry using CloudCompare's cross-section tool. The cross-sections were extracted in between certain intervals to keep the overall tunnel orientation. Furthermore, cross-sections were extracted where significant geometric cross-sectional changes were detected or when there was a sudden change in the tunnel cross-sectional orientation. By following this method, 1,429 slices were extracted for the vectorization of tunnels below and near Rosalila (Figure 3.21). These

slices were then vectorized by using their relevant geometric features and ignoring any sharp features present due to the excavation and consolidation processes (Figure 3.22).



Figure 3.21. Aerial view of extracted tunnel cross-sectional slices.

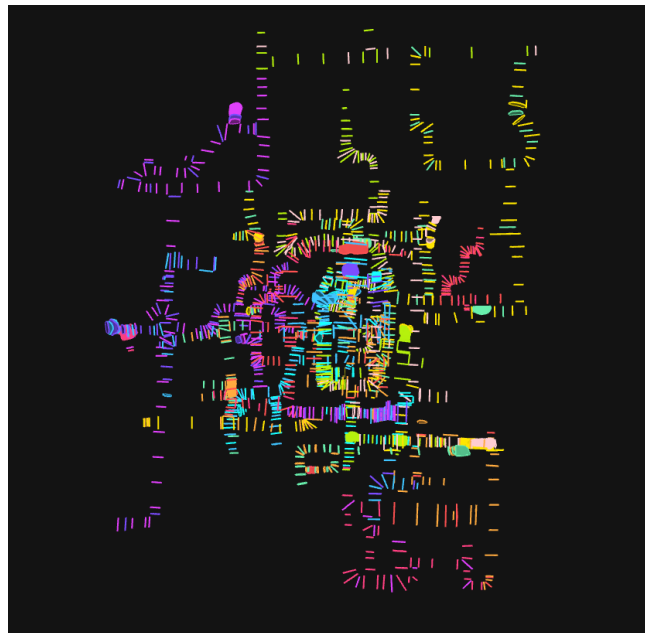


Figure 3.22. Plan view of vectorized tunnel slices.

### 3.4.2 Vectorization of Rosalila's Replica Point Cloud Data

This approach was also used to vectorize the overall geometry of the replica of Rosalila. For the purposes of this study, the overall structural analysis does not require capturing the stucco and minor detailing of the exterior of the replica, but only general information such as floor width and height and major decorative elements are required to generate a representative geometry. In this sense, for the replica, cross-sectional slices were extracted along the height of the structure at the beginning and at the end of its floor levels. Additional cross-sections of the entrances at the different floors were also captured. These slices were extracted with CloudCompare and exported into Pix4DSurvey (Figure 3.23), where they were vectorized with the rest of the tunnel system (Figure 3.24).

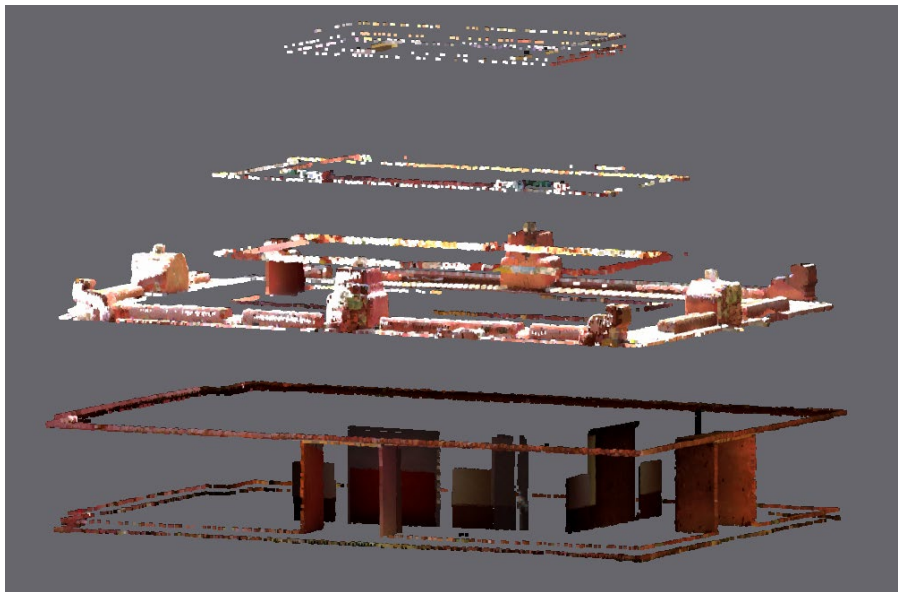


Figure 3.23. View from the southwest of extracted cross-sectional slices from Rosalila's replica point cloud.

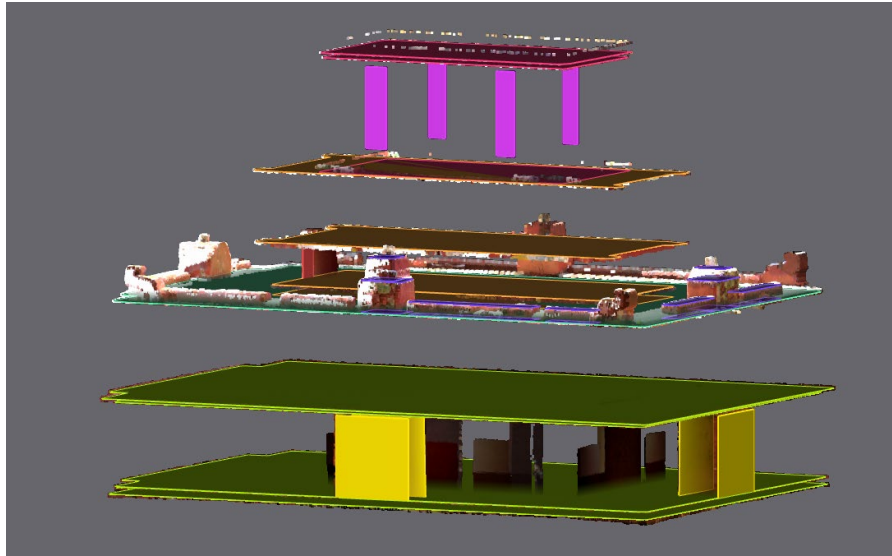


Figure 3.24. View from the southwest of Rosalila's replica vectorized cross-section.

### 3.5 Geometry Generation

#### 3.5.1 Temple 16 Exterior and Interior Tunnel Geometry Generation

The vectorization results were exported to AutoCAD (2022) in the form of .dfx files. This process converts the paths and shapes defined during vectorization into representative 3D polylines. Figure 3.25 and Figure 3.26 show the final results of the exterior of Temple 16 and the tunnel vectorization processes visualized in AutoCAD. The exported polylines are used to create associative surfaces in AutoCAD via the “SPATCH” command. AutoCAD's associative surfaces were chosen over the NURBS type considering that the vectorized polylines were already representative of the structure's geometry and very small adjustments were needed to regenerate the captured features from the geometry. Furthermore, associative patching surfaces allow the creation of a chain of dependency between surfaces and boundary objects and surfaces with other connecting surfaces. Given the complexity of the geometry, this type of surface satisfies

the purpose of creating a high-fidelity model that can be used for finite element analysis. Figure 3.27 and Figure 3.28 show the regenerated geometry of Temple 16 via patching surfaces. To create a water-tight volume for solid generation, an arbitrary maximum depth was set based on the maximum depth of the archaeological tunnels and the maximum tunnel diameter from this area. Previous closed-form solutions of circular cavities surrounded by a compressive elastic media under hydrostatic loading suggest that the effects due to stress concentration around the cavity's perimeter differ only by 2.8% from the media's field stress at a 3-diameter distance from the perimeter (Celada & Beniawski, 2019). By computing the distributed depth of the extracted slices for vectorization, the maximum tunnel depth was found at 588.89 m with a maximum diameter of 3.1 m. Therefore, to minimize the impact of boundary conditions on the lower-level tunnels, the maximum depth of the geometry was set at 578 m.

A similar process was performed for re-generating the tunnel geometries. The exported polylines were smoothed into 4<sup>th</sup>-degree polynomial splines and used for creating representative tunnel surfaces with the “LOFT” command. The smoothing of the exported polylines was done to avoid any sharp geometries that could potentially create undesired stress concentrations around the tunnels during the analysis. Figure 3.29 shows the regenerated geometries of the tunnels.

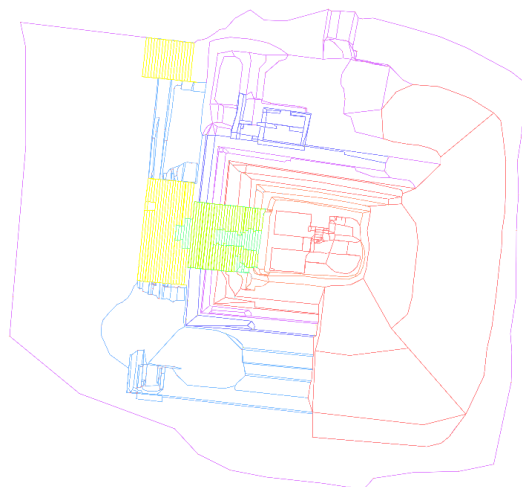


Figure 3.25. Rendered plan view of Temple 16's vectorized features in AutoCAD.

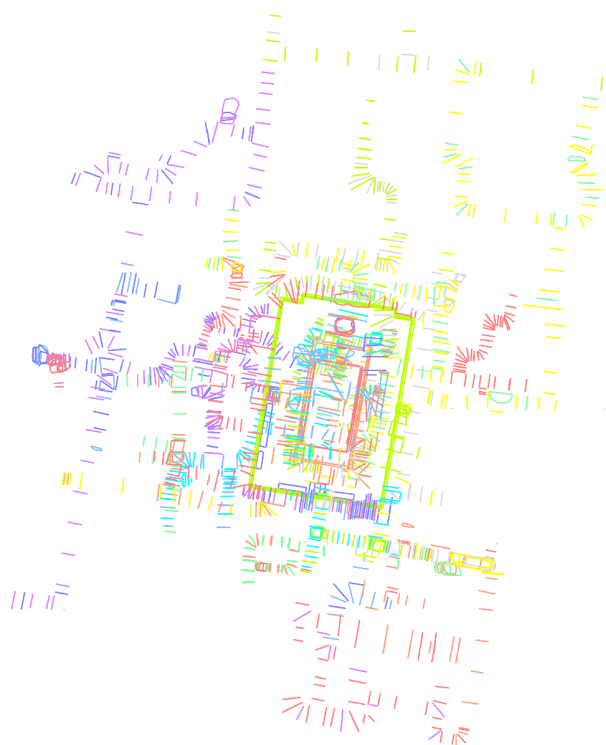


Figure 3.26. Rendered plan view of Temple 16 tunnels and Rosalila's vectorized features in AutoCAD.

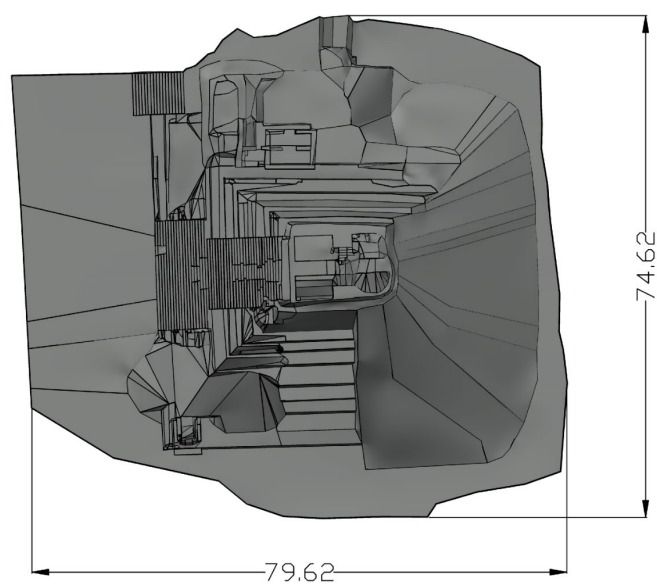


Figure 3.27. Rendered plan view of Temple 16's regenerated geometric model in AutoCAD (units in meters).

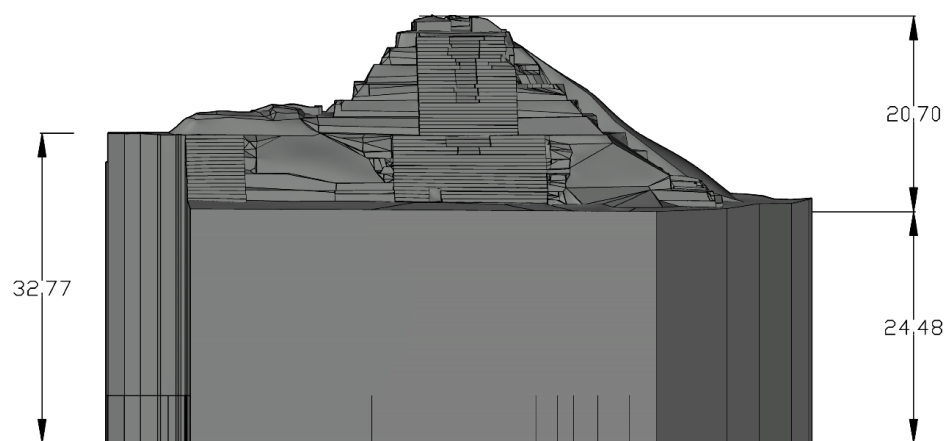


Figure 3.28. Rendered view from the west of Temple 16's regenerated geometric model in AutoCAD (units in meters).

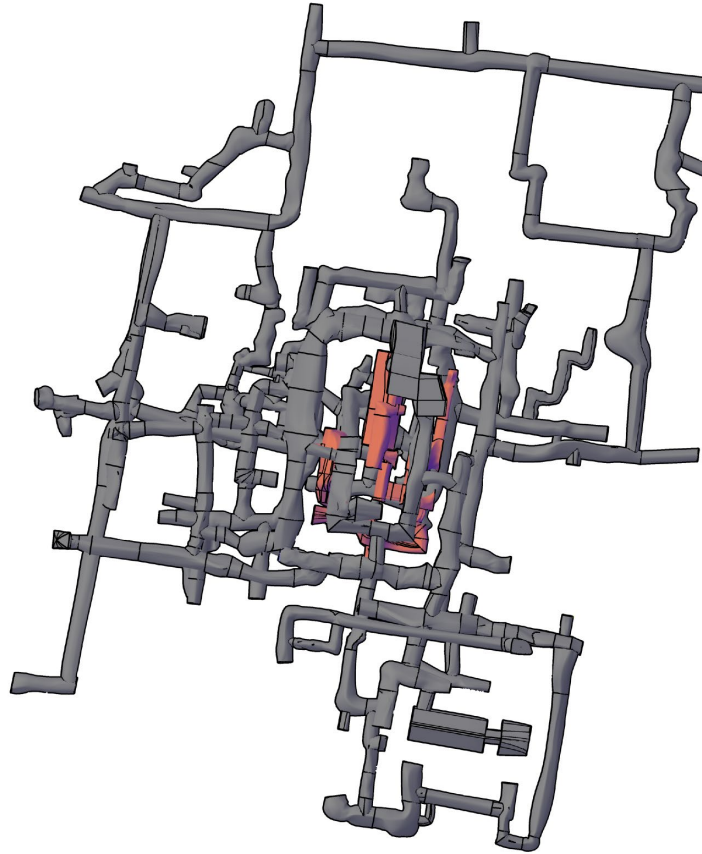


Figure 3.29. Rendered plan view of Temple 16's tunnels regenerated geometric model.

Rosalila's excavated rooms and tunnels marked with red.

### 3.5.2 Rosalila's Exterior Geometry Generation

The cross-sectional slices collected from Rosalila's replica geometry were utilized to generate a representative solid model of the structure. Once the vectorized polylines were exported, their corners were smoothed via 4<sup>th</sup>-degree polynomials, and cross-sectional patching surfaces were created via the "SPATCH" command. The square cross-sectional surfaces were converted into solids by extruding them to desire a height by



using the command “THICKEN”. More irregular cross-sectional surfaces were connected via the “LOFT” command and then converted into solids with the “SURFSCULPT” command. The generated geometry, however, is not completely representative of the current state of Rosalila. As Figure 3.30 shows, the point-cloud alignment of the Replica into the overall model shows that the northern side of its upper level was sticking out from the exterior point cloud. This observation confirms that the northern side of Rosalila’s third level was partially demolished during its burial. Because there is no current information about the approximated clearance between what remains of Rosalila’s third level and the exterior surface of Temple 16, it is assumed that the northern side of Rosalila’s 3<sup>rd</sup> level intercepts Temple 16 at its exterior surfaces. To include this in the geometry, Temple 16’s surfaces were exported into Rosalila’s model and used to perform parallel cuts to the solid (Figure 3.31 and Figure 3.32). Finally, Figure 3.33 and Figure 3.34 show views of the generated Rosalila geometry with the rest of the tunnel system.

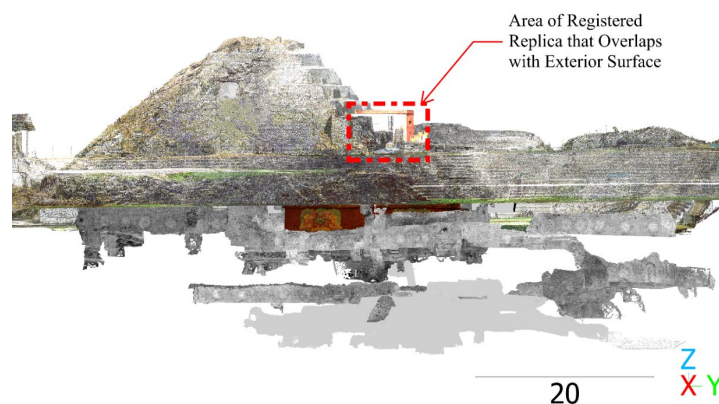


Figure 3.30. View from the east of Temple 16's point cloud system showing overlap between replica and Temple 16 exterior surface (scale in meters).

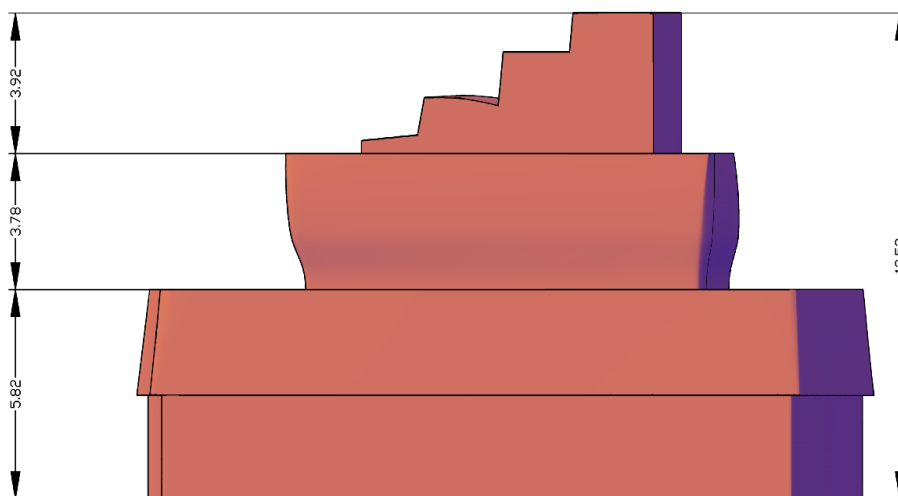


Figure 3.31. Rendered view from the west of Rosalila's regenerated geometric model  
(units in meters).

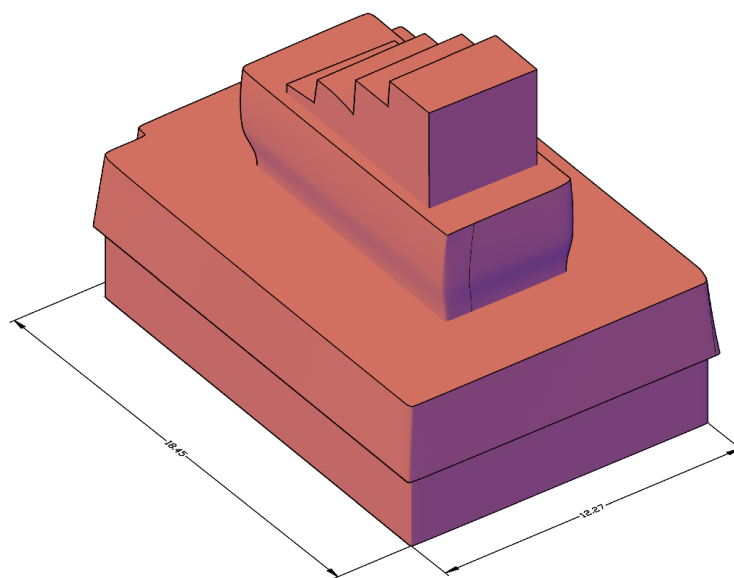


Figure 3.32. Rendered view from the southwest of Rosalila's regenerated geometric  
model (units in meters).

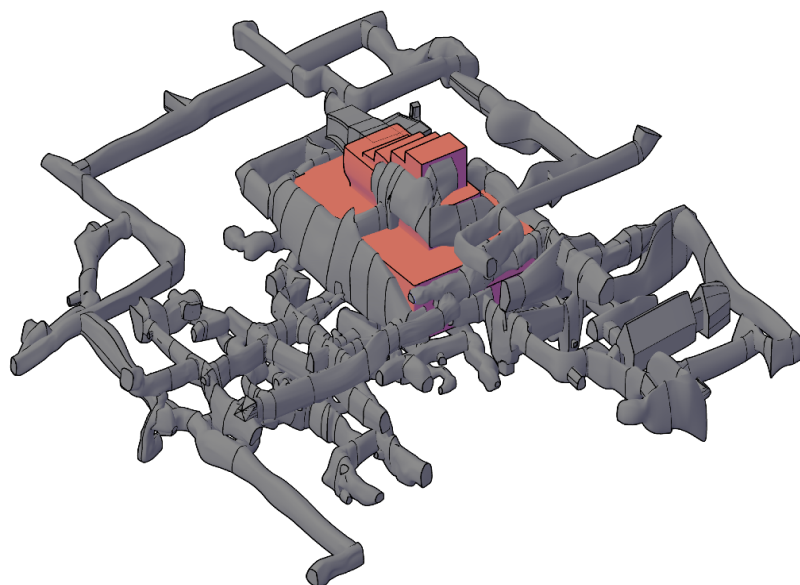


Figure 3.33. Rendered view from the southwest of Rosalila and Temple 16 tunnels  
geometric models.

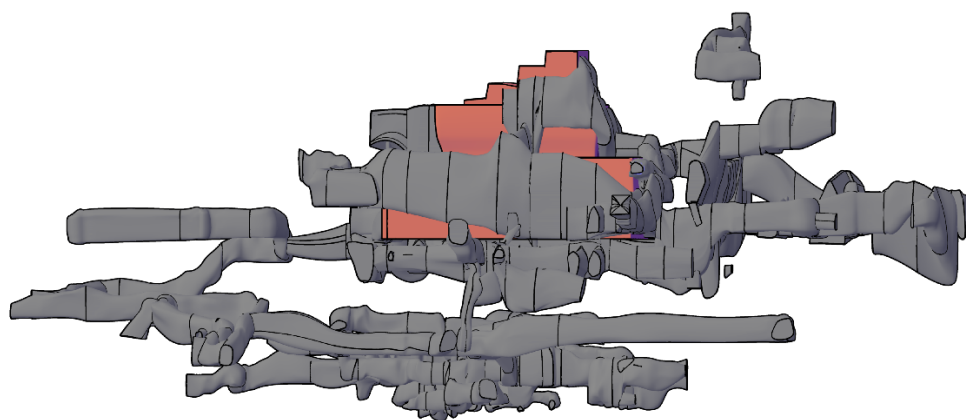


Figure 3.34. Rendered view from the west of Rosalila and Temple 16 tunnels regenerated  
geometric models.

## **CHAPTER 4 – FINITE ELEMENT MODELING**

### **4.1 Chapter Overview**

The first half of this chapter starts with an overall description of the element types selected for generating the meshes, as well as the general loading curve and selected boundary conditions. Material inputs and material modeling for the different infill levels within Temple 16 and Rosalila are then derived based on currently available information and modeling considerations. Finally, the selected inputs and analysis type will be validated in two different tests: a proposed circular cavity stress analysis for material and boundary conditions validation, and a test based on Temple 16's Exterior Geometry for validating numerical convergence. For the analysis of the Temple 16 system, the LS-DYNA v11.1 MPP (2023) finite element solver was selected as the finite element solver to be used for the analysis. On the other hand, Altair's Hyperworks (2023) environments were used for the pre- and post-processing phases of the analysis. For pre-processing, Altair's Hypermesh was selected for the final geometry assembly and meshing processes. Hypermesh is one of the industry's preferred tools, given its ability to generate high-quality meshes based on imported geometries, and its flexibility to export models to different solvers, including LS-DYNA. Finally, Altair's Hyperview was selected for final post-processing and results visualization.

### **4.2 General Model Characterization**

#### **4.2.1 Element Type**

Given the unique and irregular features of Temple 16's geometry, second-order 10-noded tetrahedral elements are used for geometry meshing. The geometric nature of

tetrahedral elements allows them to be used for automatic meshing algorithms that greatly simplify the overall meshing process. In addition, the second-order nature avoids the volumetric strain locking that is typical in linear triangular elements for stress-strain analysis, allows a more accurate approximation of the stress-strain field within an element subdomain, and can capture geometric curvatures within its geometry (in the form of quadratic approximation) without compromising its general formulation and solution accuracy. A reduced integration approach was selected, given the overall model complexity and corresponding computational demand. This element and integration approach are implemented in LS-DYNA through the \*SECTION\_SOLID card formulation 16, a 10-noded second-order tetrahedron with 5 Integration Points (Figure 4.1). To avoid any spurious stress due to the reduced integration approach, \*HOURLASS control card formulation 6 was included in the solid element formulation to enhance the strain formulation of the generated solids (LSTC, 2018).

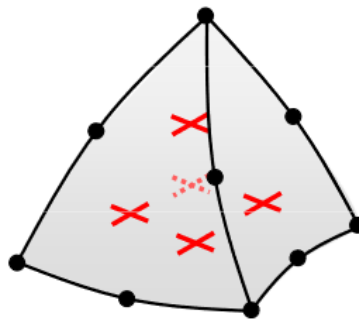


Figure 4.1. LS-DYNA ELFORM 16 10-noded tetrahedron and its integration points (red marked) (*DYNAmore, 2011*).

#### 4.2.2 Analysis Considerations and Loading

For the analysis of Temple 16's tunnels, a linearly elastic static analysis approach was selected, given its low computational demand when considering the level of geometric detail and overall model complexity. This was achieved using LS-DYNA's implicit analysis cards (Refer to Appendix A). While it is expected that the resulting stress and strains will be overestimated via this approach, it is expected that the obtained results will still reflect an overall understanding and localization of tunnel sections with stress concentrations and potential stability concerns.

Since the overall goal is to evaluate the existing tunnels against the action of the structure's self-weight, the only load to be considered for analysis is gravity. To define gravity in LS-DYNA, a linear unit load curve was first defined via the \*DEFINE\_CURVE card to progressively load the effects of gravitational acceleration for the first 4 seconds of the analysis (Figure 4.2). This load curve is then scaled to gravity's typical value ( $9.806 \frac{m}{s^2}$ ) when evoking the \*LOAD\_BODY\_Z card, which applies the load curve along the model's global Z axis.

Because most of the tunnels are below the current grade level, it is expected that more than 50% of the model's volume represents the underground features of the system. Because of the limited knowledge of the soils and infill materials that lie below Temple 16, it is assumed that the underground layers of the model are resting on top of a rigid soil layer. That is, the nodes that make up the bottom boundary surface of the model are prevented from displacing vertically (along the Z direction) and laterally (along the X or Y directions). Similarly, it is assumed that the system's underground levels will be

connected to its surroundings from all sides, allowing these layers to move vertically, but keeping them from any sideways displacements due to the continuity condition. Therefore, it is assumed that the nodes that make up the sides of underground boundary surfaces of the model will be allowed to be displaced vertically (along the Z direction) but not laterally (along the X or Y directions). These boundary conditions were applied to the LS-DYNA model by specifying \*BOUNDARY\_SPC cards for each respective case (see Appendix A).

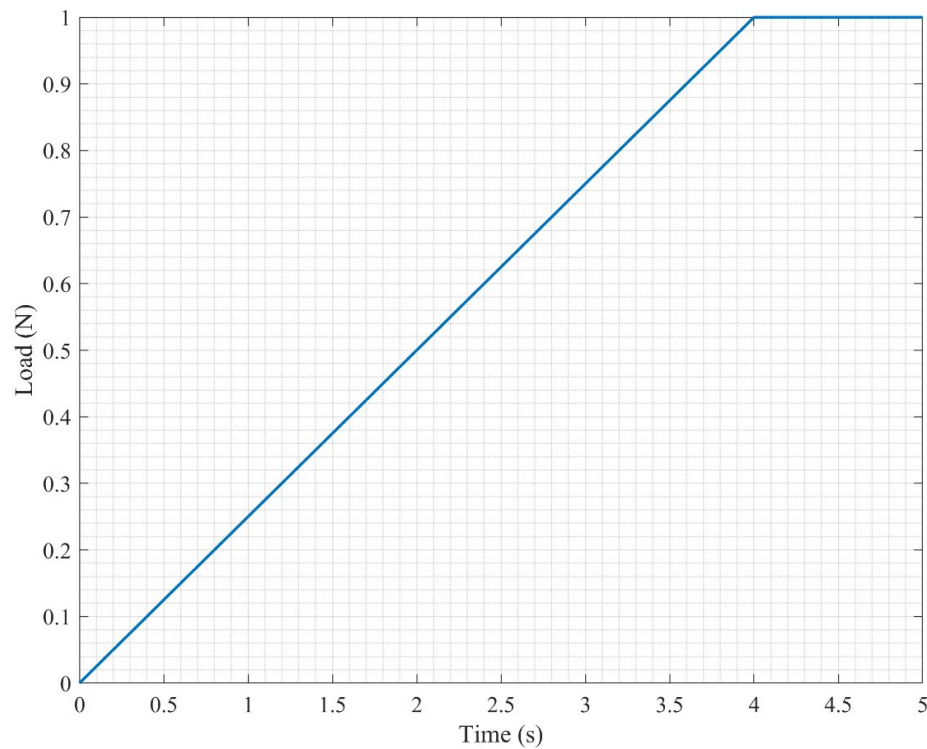


Figure 4.2. Applied unit load curve for gravity loading.

## **4.3 Material Modeling Characterization**

### **4.3.1 Infill Material Characterization**

Based on the historical literature outlined in Chapter 2, Temple 16 is comprised of three different types of soil layers:

- Bottom Layer: Barro or Clay/ Dark River Mud
- Medium Layer: Tierra café oscuro or Clayey Silty Sand with Gravel
- Upper Layer: Girún or Yellow Silty Sand

In their study of the Hieroglyphic Stairway and Temple 10-26 Tunnels, Pires et al. (2021) characterized girún as Silty Loose Sand based on a disturbed sample that was extracted from Rosalila in 2019. Given the limited geotechnical information that is available from the site, the parameters used in this study belong to typical parameters that are used for silty soils by geotechnical engineers. Table 4.1 shows the soil parameters chosen for this infill layer in the Pires et al. study (2021). Given that the extent of their study was to analyze the tunnel system laying above the current grade, the assumption of a homogenous silty sand layer was deemed appropriate for the scope. However, most of Temple 16's tunnel system is within the middle reddish-brown soil layer (clayey silty sand with gravel) with some extending into the river mud infill layer. Therefore, it is necessary to characterize these lower two soil layers in order to adequately assess Temple 16, which is summarized within the remainder of this section.



Table 4.1. Soil parameters used by Pires et al. (2021) for characterizing silty sand infill layer.

<b>Dry Unit Weight</b> $\gamma$ (kN/mm <sup>3</sup> )	<b>Modulus of Elasticity</b> <b>E</b> (MPa)	<b>Poisson's Ratio</b> <b>v</b> (-)	<b>Cohesion Parameter</b> <b>c</b> (KPa)	<b>Friction Angle</b> $\phi$ (Degrees)
17	10	0.3	Varies	30

According to the CATCP 2020, the bottom river mud layer is stable because of the constant exposure to high moisture content (MC), given its proximity to the water table (Lacombe, Fash, & Fash, 2020). From the available literature, the water table of the Copán River has an average elevation of 590 to 591 meters above sea level for the Copán Pocket Area (Windward & Eileen, 2013). Considering the geometric data of Temple 16 described in Chapter 3, there is a minimum tunnel elevation of 588.89 m. Given that the minimum tunnel elevation is less than the floodplain elevation, flooded tunnels in the lower portions of Temple 16 during the rainy season are very plausible. Because CATCP 2020 also indicates the presence of river-mud infill in the lowest tunnel levels the maximum elevation of the river-mud layer is assumed to be at 592.5 meters above sea level. This elevation was selected by considering a maximum tunnel height of 3.1 at the lowest levels and adequate meshing generation around the tunnel's cross-sections.

Approximating the distribution between the medium and top infill layers is similarly based on the historical fact that girún was utilized for burying Rosalila. Current point cloud data of the tunnels approximates the elevation of tunnels surrounding Rosalila to be between 601 and 602 meters above sea level. Assuming that the grade during the

construction and burial of Rosalila were at 600 and 601 meters, respectively, it is assumed that the maximum elevation of the middle soil layer is at 600 meters above sea level. Therefore, the girún upper layer would cover the rest of the upper superstructure of Temple 16, including the current grade, which matches with the historical information provided by the CATCP 2020 and historical literature.

Soil properties for each layer were determined based on the Unified Soil Classification System (USCS) that is widely used throughout the geotechnical field and shown in Figure 4.3. Based on the disturbed sample taken from Rosalila in 2019, Pires et al. categorized the top girún layer as silty sand (labeled as SM by the USCS). Pires et al. did not explicitly account for the presence of large gravel and boulders in the soil matrix since these elements are floating in the finer matrix and play no role in the overall mechanical behavior (Pires, Bilotta, Flora, & Lourenco, 2021). This assumption is necessary given the limited on-site geotechnical testing of the infill layers.

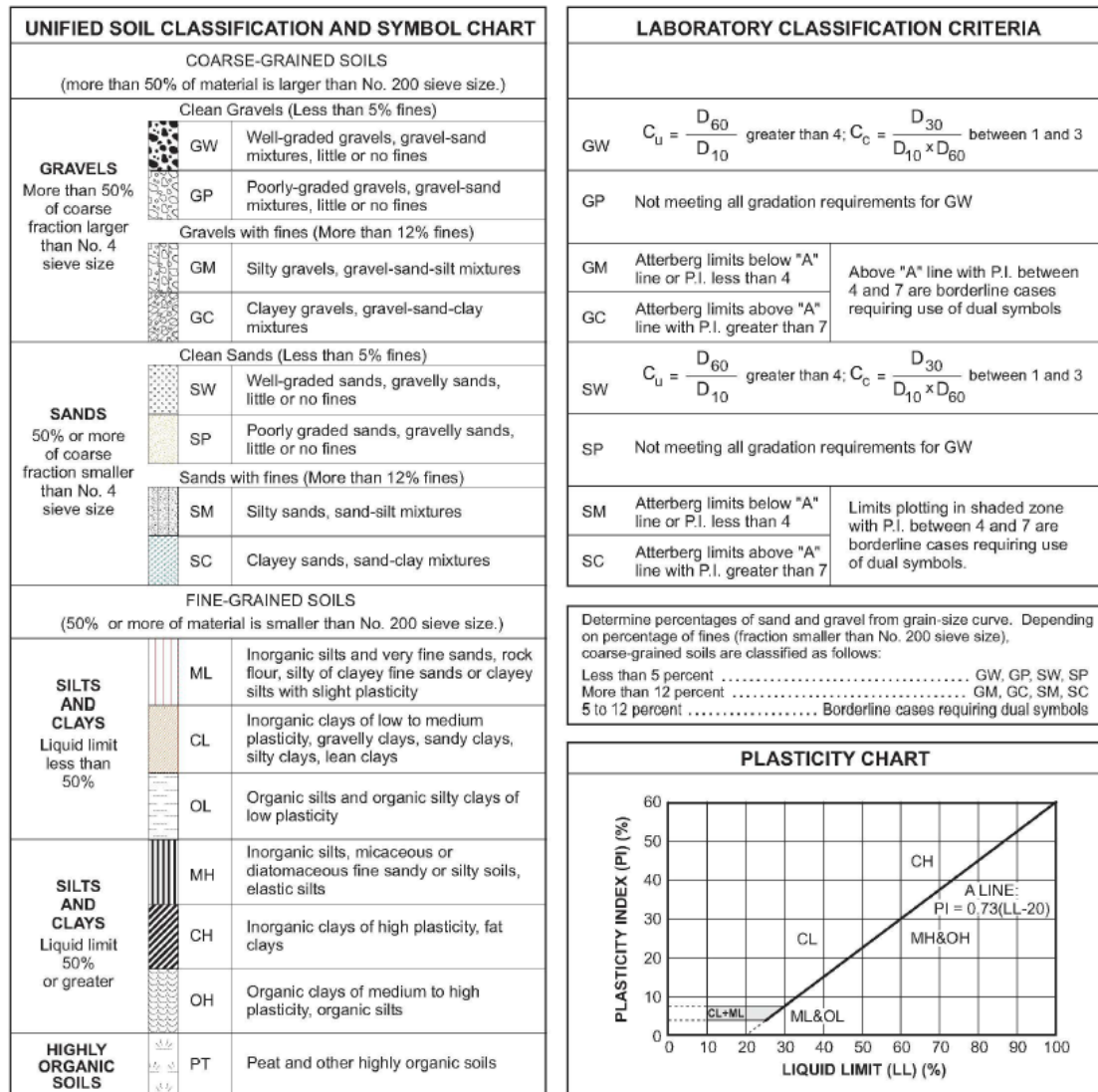


Figure 4.3. Unified Soil Classification System (USCS) chart.

From the CATCP 2020 report, the middle layer is characterized as reddish-brown soil with a minimum number of clays in its composition. This layer is described as an unstable layer that triggers collapse when it is too dry and loses cohesion if it becomes too wet (Lacombe, Fash, & Fash, 2020). Based on this description and by omitting the influence of construction debris in the infill matrix, this layer can be categorized as

clayey sand (SC) according to the USCS. Similarly, because the bottom layer was primarily filled with clay-rich materials, it can be categorized as a high plasticity inorganic clay (CH) when considering its high compressive stability and constant exposure to high moisture content. Once each layer has been associated with a USCS category, it is possible to characterize each infill type with widely accepted geomechanical parameters for their respective type of soil. As Pires et al suggested, the silty sand layer can be characterized by the values shown in Table 4.1. Similarly, average geotechnical parameters (Das & Sobhan, 2017) for the other two layers were assigned and summarized in Table 4.2.

Table 4.2. Chosen material characterization parameters.

In-Fill Layer Type	USCS Classification	Minimum Elevation with Respect to Sea Level (m)	Maximum Elevation with Respect to Sea Level (m)	Dry Unit Weight $\gamma$ (kN/m <sup>3</sup> )	Modulus of Elasticity E (MPa)	Poisson's Ratio $\nu$ (-)	Cohesion Parameter c (KPa)	Friction Angle $\phi$ (Degrees)
Girún (Yellow Sand)	Silty Sand (SM)	600	623.24 <sup>(2)</sup>	17	10	0.3	0	30
Tierra Café Oscuro (Reddish-Brown Soil)	Clayey Sand (SC)	592.5	600	18.5	15	0.4	0	31
Barro (River Mud)	High Plasticity Inorganic Clay (CH)	578 <sup>(1)</sup>	592	19	20	0.45	103	23
(1): Current Minimum elevation for Entire Model								
(2): Approximated Maximum Elevation for Entire Model								

### 4.3.2 Infill Material Modeling

While material formulations are typically selected based on the dominant failure theory that agrees with experimental results, this is unable to be done for the infill material in this analysis due to the lack of material data. Therefore, the material formulation is selected to ensure the following requirements:

- Must ensure easy formulation and convergence.
- Must be universally applicable for different types of soils (i.e., clayey soils, sandy soils, etc.)

For civil engineering studies and applications, soils have been classically modeled under the Mohr-Coulomb (M-C) failure criteria. This is because M-C theory is formulated as a function of the major and minor principal stresses ( $\sigma_1$  and  $\sigma_3$ , respectively), or as a function of  $\sigma_1$  and the shear stress  $\tau$  on the failure plane. This assumption fits well with experimental observations of granular soils during triaxial tests that are conducted under environments where the intermediate stress  $\sigma_2 = \sigma_3$ . However, the combination of these assumptions creates a hexagonal failure surface with sharp discontinuities that serve as an impediment to achieve convergence in numerical analysis and plastic deformation studies (Labuz & Zang, 2012). Because of the numerical challenges that M-C theory presents, Drucker-Prager Theory (D-P Theory) is an alternative formulation to the classic Mohr-Coulomb Theory that is widely used to characterize soil and granular material behavior. The main contrast between classic M-C

theory and D-P theory is that the latter recognizes the influence of the intermediate principal stress  $\sigma_2$  in the shape of the yielding surface. The pressure dependency of this theory allows a smoother yielding surface (Figure 4.4) where plastic deformation can be determined more accurately due to a better overall flow rule, and numerical convergence is easier to achieve compared to M-C theory.

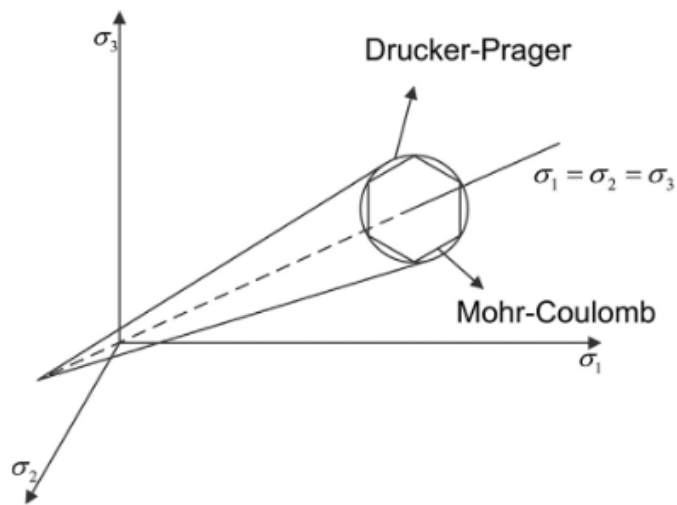


Figure 4.4. Mohr-Coulomb vs Drucker-Prager failure envelopes.

Given its easy formulation and its convenient numerical stability and convergence, the modified Drucker-Prager material model was selected to characterize the infill materials of Temple 16 via the \*MAT\_193 LS-DYNA material card. Table 4.3 shows the typical inputs defined for each infill material card and can also be found in the keyword scripts (Appendix A), the properties in Table 4.2 were used to derive and populate the specified inputs of this material card. As Figure 4.4 shows, the classical formulation of D-P theory produces a failure surface that tends to overestimate the soil's capacity around its failure surface. To correct this, a scaling factor  $K$  was added to the

formulation to fit the failure surface into experimental results. This scaling factor produces a more approximated and smoother version of the M-C surface that is still convenient for numerical convergence and matches with experimental data. For typical soils, a recommended value of  $K = 0.85$  is a standard. However, the chosen  $K$  value should not go below 0.75 (LSTC, 2018). Therefore, an average value of  $K = 0.8$  was conservatively assumed considering the limited available infill information.

Table 4.3. LS-DYNA material input parameters.

In-Fill Layer Type	Material Density $\bar{\rho}$ (kg/m <sup>3</sup> )	Shear Modulus G (Pa)	Poisson's Ratio $\nu$ (-)	$K$	Friction Angle $\phi$ (Radians)	Cohesion Parameter $c$ (Pa)	Dilation Angle $\Psi$ (Radians)
Girun (Yellow Sand)	1733.63	3.85E+06	0.30	0.80	0.52	0.00E+00	0.00
Tierra Café Oscuro (Reddish-Brown Soil)	1886.60	5.36E+06	0.40	0.80	0.54	0.00E+00	0.00
Barro (River Mud)	1937.59	6.90E+06	0.45	0.80	0.40	1.03E+05	0.00

#### 4.3.3 Rosalila's Material Modeling and Characterization

The material characterization of Rosalila will be further simplified as a linear elastic material. From available literature like the CATCP 2020, it is known that the construction methods that were used by the Copán civilization for building structures like Rosalila employed a mortar mixture of clayey materials and rock. The actual mechanical behavior of the resulting material has not been quantified or tested in sufficient detail. An analogy between Rosalila's material mixture and modern-day masonry can be made to



assume some general material properties. For further simplification, a smeared assumption between mortar and masonry elements can be made since the local failure of the elements that make up the structure is out of the scope of this investigation. Furthermore, a linearly elastic material response can be assumed in accordance with the simplifications made for this material and the overall analysis approach.

The material was defined via the \*MAT\_ELASTIC card available in LS-DYNA. This material card describes an isotropic hypoplastic material that is available for solid elements, which is considered as an acceptable candidate by assuming small strains under static loading. The modulus of elasticity  $E$  and Poisson's ratio  $\nu$  were assumed to be  $E = 1000 \text{ MPa}$  and  $\nu = 0.2$  as typical masonry parameters. The material density was set at  $\gamma = 22.78 \frac{\text{kN}}{\text{m}^3}$  (or  $145 \frac{\text{lb}}{\text{ft}^3}$ ) which is a typical density for unreinforced concrete and heavy-weight masonry (Pires F. , Bilotta, Flora, & Lourenco, 2021).

## **4.4 Validation of Tunnel Stress Analysis and Boundary Conditions**

### **4.4.1 Proposed Case Study**

From a geomechanical point of view, tunnels can be understood as holes or cavities that go through the soil media. Temple 16's archaeological tunnel system is made up of different irregular tunnel cross-sections that were excavated through different missions. In order to understand how the existing tunnels below Temple 16 disturb and influence the stress field in the surrounding media and buried structures, it is necessary to preliminarily investigate the influence of a single cavity in the overall stress field. This preliminary investigation would also allow validating assumptions regarding boundary

conditions as well as provide an expected accuracy level between the finite-element solution and an expected one derived from geomechanics.

While most archaeological tunnels can be approximated by arched or horseshoe-shaped cross-sections, this validation case study will utilize a simplified circular cross-section due to the depth of literature regarding circular cavity stress distribution and stability. The case study considers a circular tunnel cross-section that is meant to idealize the tunnel at the lowest elevation of Temple 16. The lowest elevation tunnel so that the validation can determine whether the base of the model is sufficiently deep such that boundary conditions do not alter the stress concentrations surrounding the tunnel cross sections. Based on the model geometry described in Chapter 3, the approximate height of the tunnel at the lowest depth (elevation of 588.89 m) is 3.1 m, making the idealized diameter of the circular cross-section equal to 3.1 m. The depth and placement of the circular cavity consider Temple 16's boundary depth of 578 m and an average surface grade elevation of 603.17 m. Considering the lowest tunnel's elevation of 588.89 m, this results in 10.9 m of soil below the cavity and 11.17 m of soil above the cavity. The cross-sectional width is set up to be equivalent to 7 diameters, or 21.7 meters. This is based on Celada and Beniawski's (2019) recommended minimum distance where the stress increase due to the presence of a circular cavity with respect to the surrounding media's hydrostatic stress starts being negligible. Figure 4.5 shows the typical cross-sectional shape of the proposed tunnel case study. Finally, in order to account for the three-dimensional nature of the model, the overall model is presented as a longitudinal circular

tunnel that runs east to west with an overall length of 77.60 meters (Figure 4.6), which is equivalent to the east-west length of Temple 16's model.

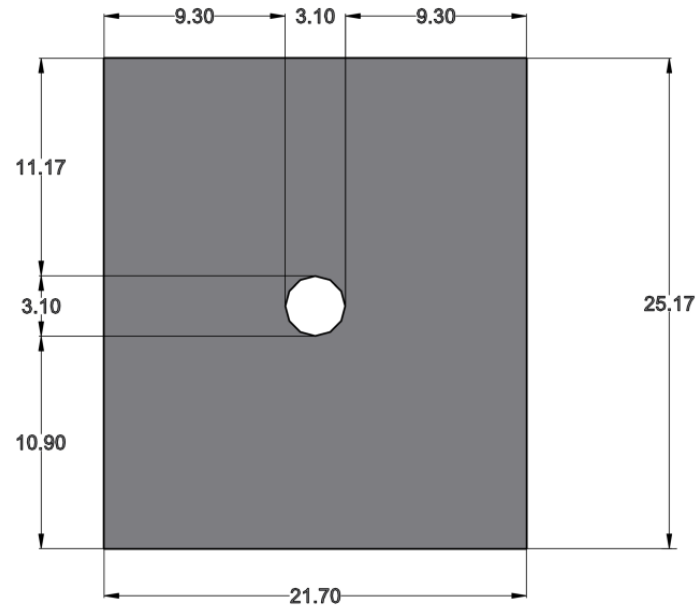


Figure 4.5. Cross-sectional View of Proposed Circular Cavity Validation Model (units in meters).

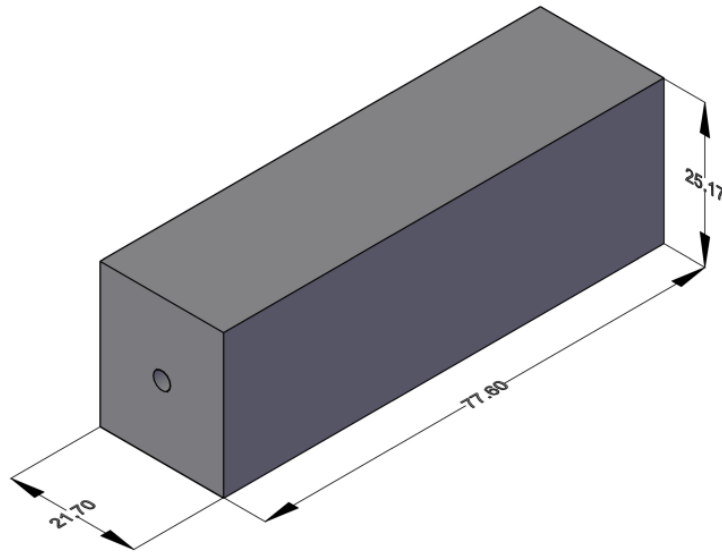


Figure 4.6. Isometric View of Proposed Circular Cavity Validation Study (units in meters)

#### 4.4.2 Finite Element Model Setup and Results

The generated solid geometry was exported to Hypermesh in order to be discretized into second-order tetrahedral elements. The size of the elements is about one-tenth of the circular cavity's diameter or 30 centimeters (Figure 4.7 & Figure 4.8). Boundary conditions were assigned to the geometry's bottom, and lateral faces such that the bottom face nodes are restrained against the three main cardinal directions (XYZ), and lateral face nodes are only free to displace along the vertical Z axis. For simplification purposes, the infill material is assumed to be homogenous along the model, and it is characterized by the selected material inputs assigned for the girún infill layer (See Table 4.2 ).

A linearly elastic implicit analysis of the proposed model under the gravitational influence of its own weight was conducted. As described in Section 4.2.2, the gravitational acceleration is progressively increased during the first 4 seconds until it reaches the constant value of gravity ( $9.81 \frac{\text{m}}{\text{s}^2}$ ) with a total simulation time of 5 seconds. By following this approach, Figure 4.9, Figure 4.10, Figure 4.11, and Figure 4.12 show the generated results for vertical, horizontal, shear and Tresca stress distributions of the model's cross-section at midspan.

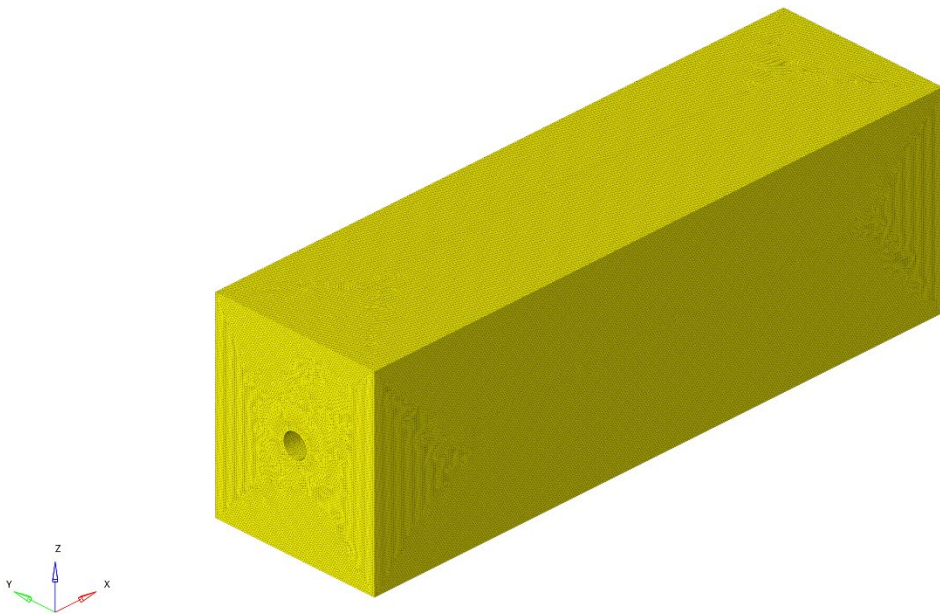


Figure 4.7. Isometric view of circular cavity finite element model.

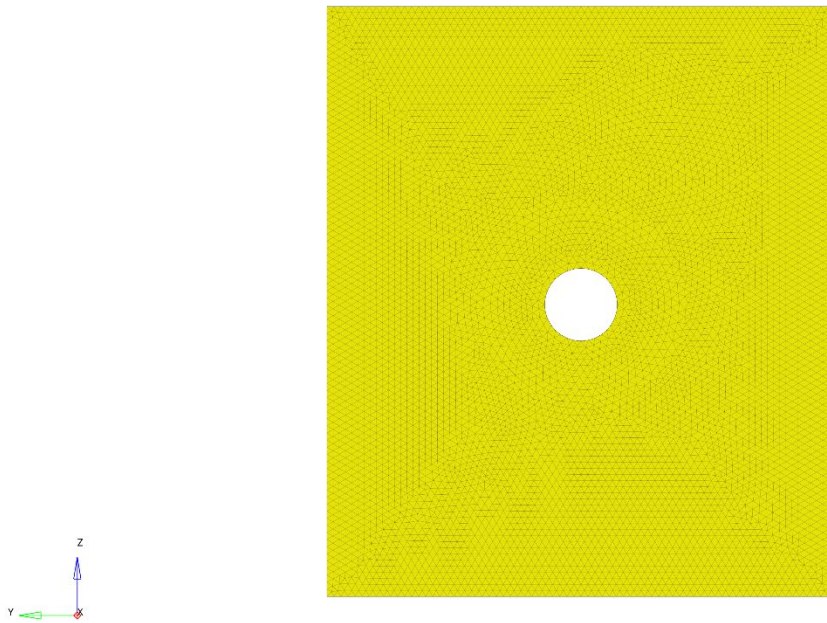


Figure 4.8. Cross-sectional view of circular cavity finite element model.

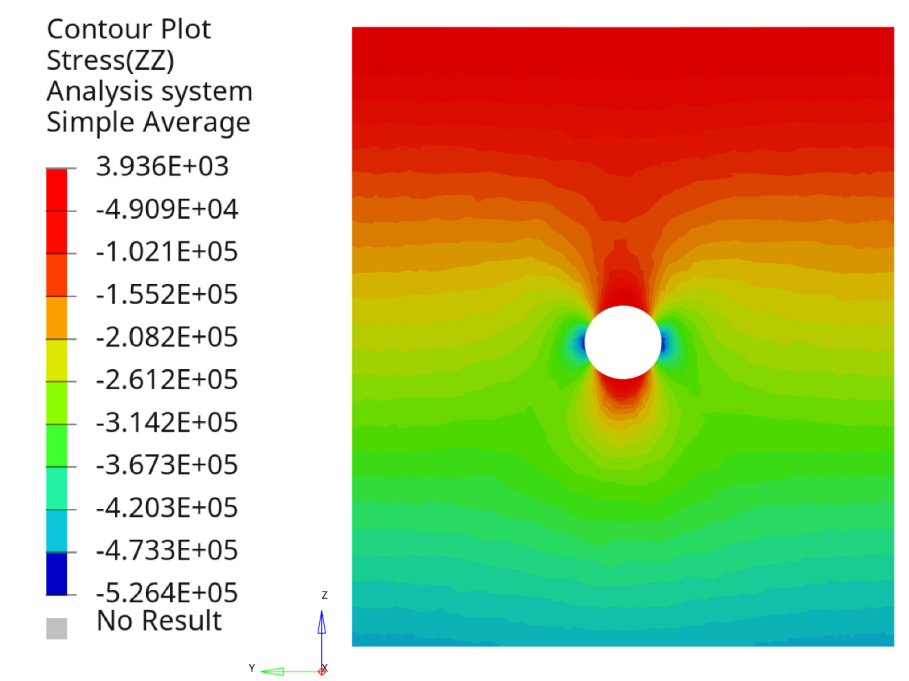


Figure 4.9. Vertical stress distribution along cross-section at model midspan.

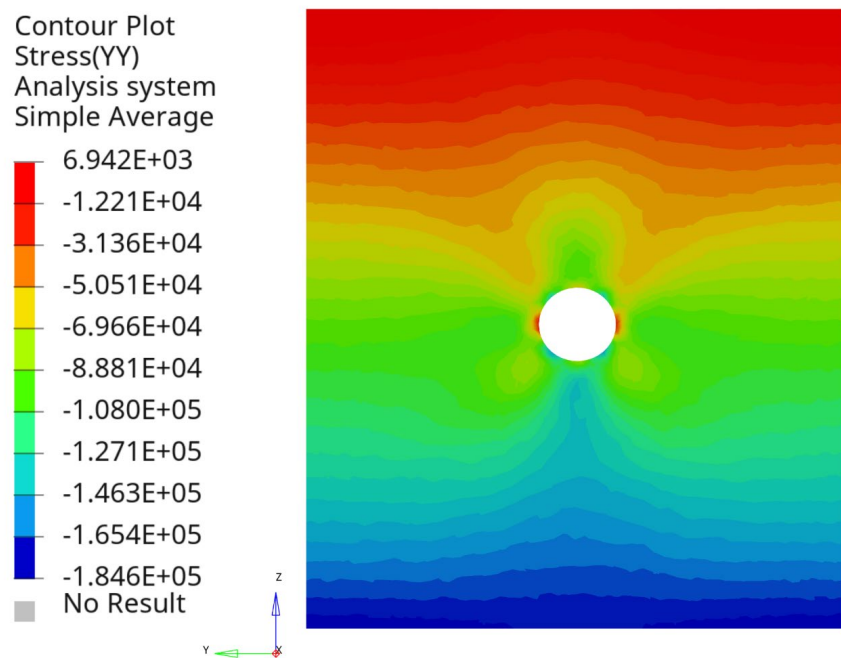


Figure 4.10. Horizontal stress distribution along cross-section at model midspan.

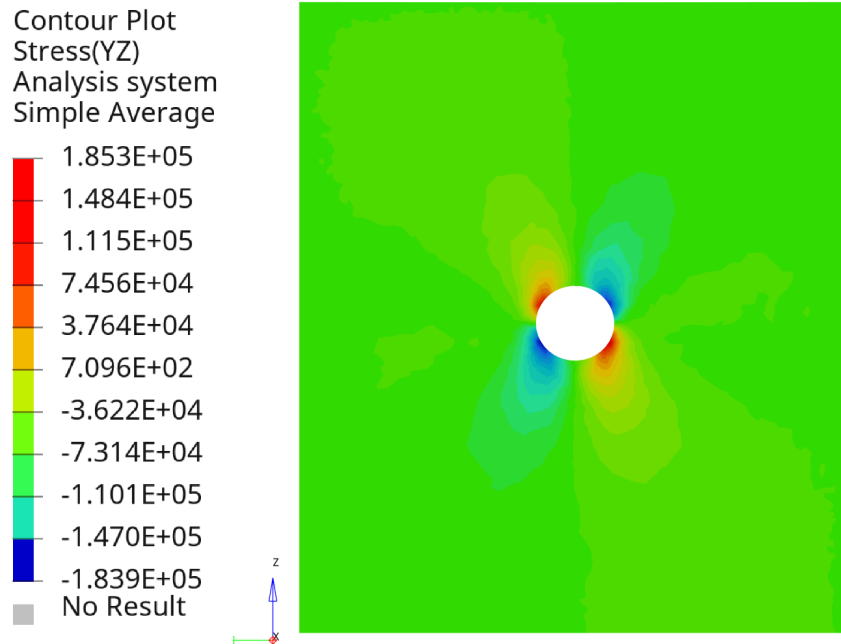


Figure 4.11. Shear stress distribution along cross-section at model midspan.



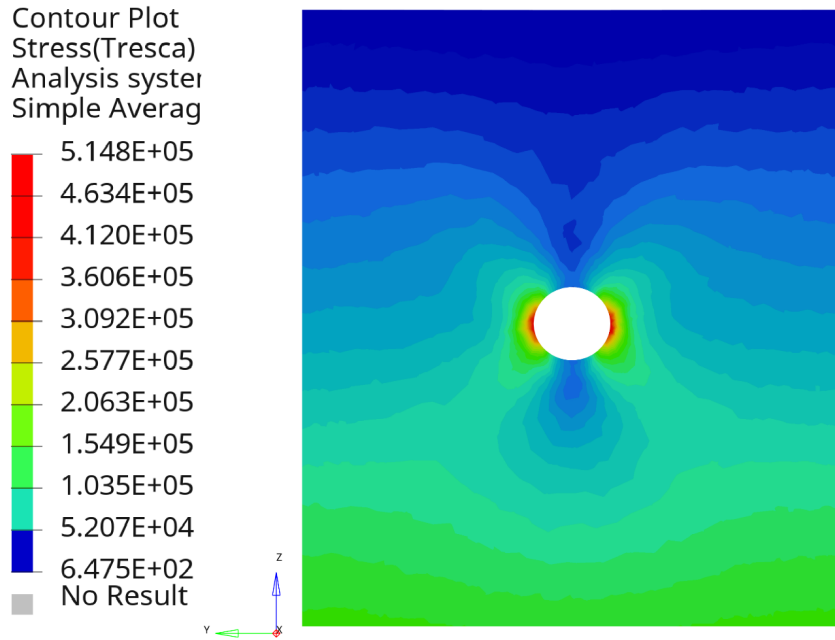


Figure 4.12. Tresca stress distribution along cross-section at model midspan.

#### 4.4.3 Closed-Form Solution Approximation for Stress Analysis

The stress distribution of a circular cavity surrounded by elastic infinite media was first investigated by Kirsch (1898) and resumed later by Timoshenko and Goodier (1970). For the case of a circular cavity uniformly loaded in both vertical and horizontal axes, the proposed closed-form solution was expressed in terms of the radial and tangential axis  $(x', y') = (r, \theta)$  as Figure 4.13 shows. Therefore, the radial and tangential stresses can be expressed by the following equations:

$$\sigma_r = \sigma_{vo} \left[ \frac{1+K_o}{2} \left( 1 - \left( \frac{R}{r} \right)^2 \right) + \frac{K_o-1}{2} \left( 1 + 3 \left( \frac{R}{r} \right)^4 - 4 \left( \frac{R}{r} \right)^2 \right) \cos 2\theta \right] \quad (4.1)$$

$$\sigma_\theta = \sigma_{vo} \left[ \frac{1+K_o}{2} \left( 1 + \left( \frac{R}{r} \right)^2 \right) - \frac{K_o-1}{2} \left( 1 + 3 \left( \frac{R}{r} \right)^4 \right) \cos 2\theta \right] \quad (4.2)$$

$$\tau_{r\theta} = \sigma_{vo} \left[ \frac{1-K_o}{2} \left( 1 - 3 \left( \frac{R}{r} \right)^4 + 2 \left( \frac{R}{r} \right)^2 \right) \sin 2\theta \right] \quad (4.3)$$

Where  $\sigma_{vo}$  is the media's vertical stress due to the vertical loading,  $R$  is the cavity's radius,  $r$  is the radial distance from the cavity's center to the point of interest, and  $\theta$  is the inclination angle with respect to the +X axis. Finally,  $K_o$  is the ratio between the media's vertical stress  $\sigma_{vo}$  to the media's horizontal stress  $\sigma_{ho}$ . Celada and Beniawski (2019) proved that when  $K_o = 1$  (hydrostatic loading condition) the media approaches the action of hydrostatic stress as the radial distance increases ( $r \gg 6R$ ). For elastic soils, the  $K_o$  factor is equivalent to the neutral state horizontal stress coefficient:

$$K_o = \frac{\mu}{1-\mu} \quad (4.4)$$

Finally, equations 4.5 to 4.8 can be used to derive the desired vertical and horizontal normal stresses as well as the shear stress. This is achieved by applying the following transformation relationships:

$$[\sigma]_{yz} = [T]^T [\sigma]_{r\theta} [T] \quad (4.5)$$

$$[\sigma]_{r\theta} = \begin{bmatrix} \sigma_r & \tau_{r\theta} \\ \tau_{r\theta} & \sigma_\theta \end{bmatrix} \quad (4.6)$$

$$[T] = \begin{bmatrix} \cos \theta & -\sin \theta \\ \sin \theta & \cos \theta \end{bmatrix} \quad (4.7)$$

$$[\sigma]_{yz} = \begin{bmatrix} \sigma_{yy} & \tau_{yz} \\ \tau_{yz} & \sigma_{zz} \end{bmatrix} \quad (4.8)$$

Where  $\sigma_{zz}$  and  $\sigma_{yy}$  are the vertical and horizontal stress fields along the cross-section, respectively, and  $\tau_{yz}$  is the cross-sectional in-plane shear stress. Finally, the Tresca stress  $\sigma_T$  can be obtained via:

$$\sigma_T = \sqrt{(\sigma_{yy} - \sigma_{zz})^2 + 4\tau_{yz}^2} \quad (4.9)$$

Equations 4.1 to 4.9 were used with the proposed cross-sectional dimensions, and girún input parameters to recreate a fringe profile of the expected stress profiles in MATLAB (2023). Figure 4.14 - Figure 4.17 show the obtained stress profiles of the proposed case-study's geometry.

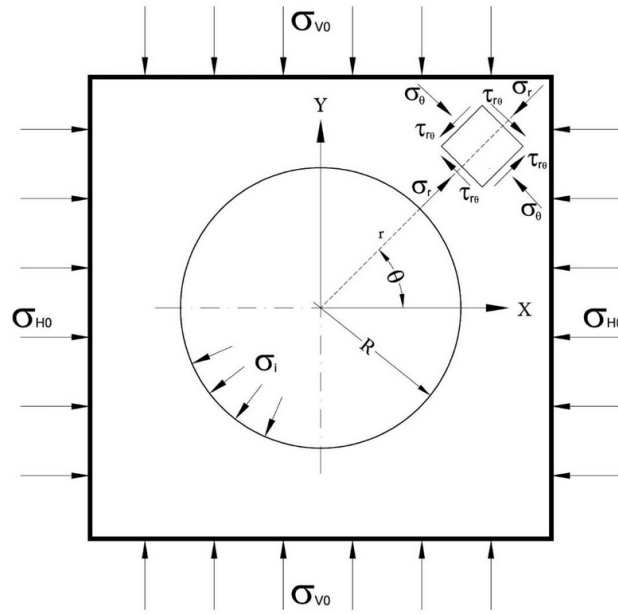


Figure 4.13. Analysis of circular cavity under hydrostatic loading (*Celada & Beniawski, 2019*).

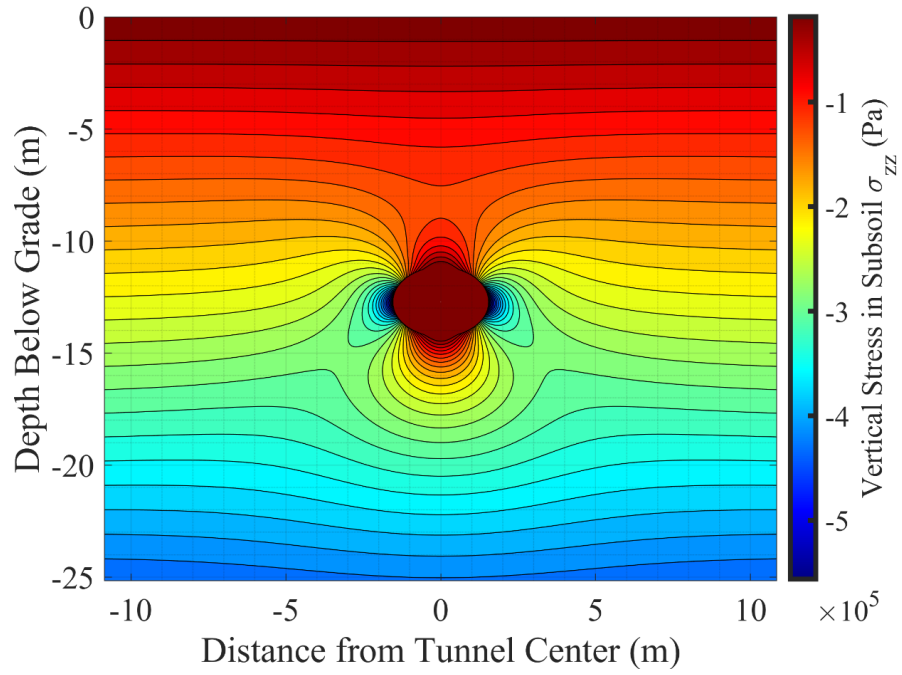


Figure 4.14. Closed-form solution vertical stress distribution.

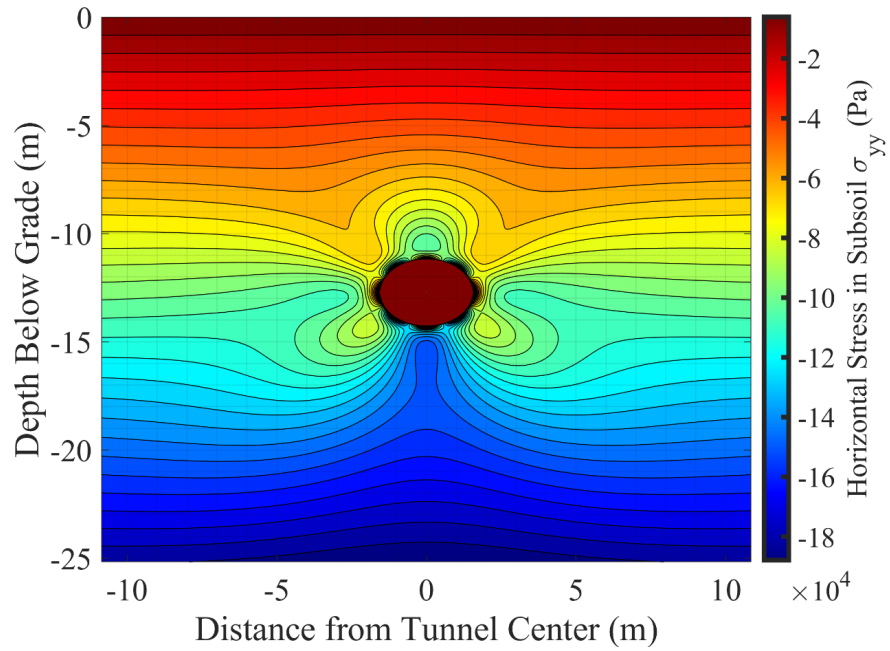


Figure 4.15. Closed-form solution horizontal stress distribution.

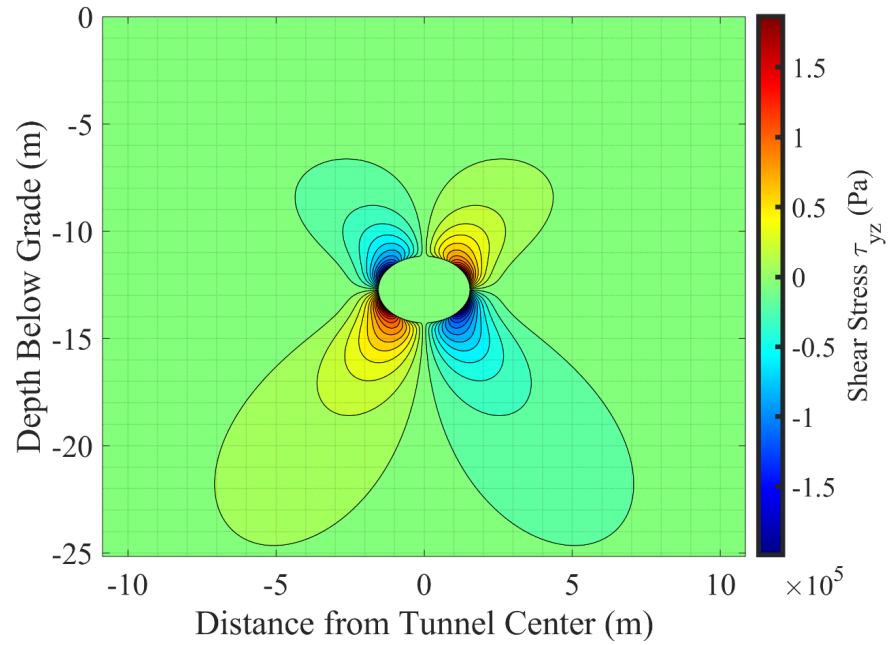


Figure 4.16. Closed-form solution shear stress distribution.

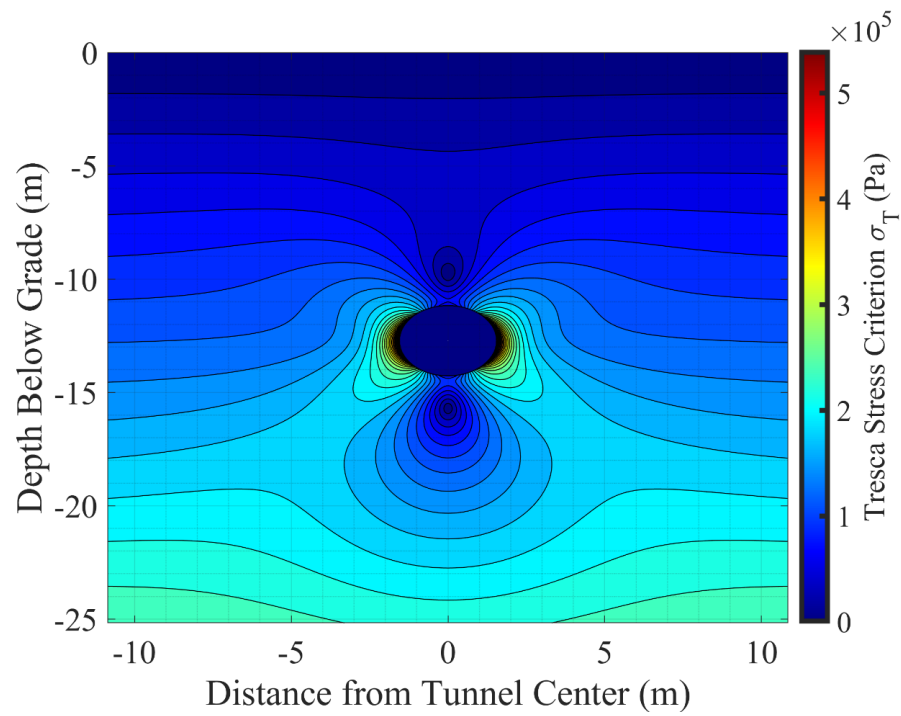


Figure 4.17. Closed-form solution Tresca stress distribution.

#### 4.4.4 Validation Study

Similar stress distributions can be seen when comparing the results from the finite element model (Figure 4.9 - Figure 4.12) and the closed-form solution (Figure 4.14 - Figure 4.17). For both approaches, the high-stress concentrations occur around the cross-section's perimeter which decreases to a rate proportional to  $\frac{1}{r}$ . Maximum stresses occur along the cavity's horizontal diameter (Figure 4.12 and Figure 4.17). The sign discrepancy between obtained and expected shear stresses in Figure 4.11 and Figure 4.16 is due to different sign conventions for shear, but the overall magnitudes and distribution pattern are the same for both figures. Overall, the maximum reported stresses in the finite element model differ by approximately 4 - 5% from the ones obtained from the assumed closed-form solution. This is considered to be an acceptable margin of error given that the selected theoretical background assumes a cavity surrounded by infinite continuous media under plain stress conditions while the finite element model is a discretized, three-dimensional system, with clearly defined boundaries.

Another goal for this proposed case study was to validate the boundary conditions of the system, especially the clearance distance required from the lowest-level tunnel to the bottom boundary of the system in order to fully capture the influence of a tunnel in the overall surrounding media. By considering the lowest point of the cavity perimeter, the vertical stress field increases with the inverse of the vertical radial distance  $r$ . The vertical stress  $\sigma_{zz}$  tends to reach the value  $\sigma_{vo}$  as the vertical clearance from the tunnel tends to infinity. By normalizing  $\frac{\sigma_{zz}}{\sigma_{vo}}$  and  $\frac{r}{R}$ , then:

$$\lim_{\frac{r}{R} \rightarrow \infty} \frac{\sigma_{zz}}{\sigma_{vo}} = 1 \quad (4.10)$$

A plot of  $\frac{\sigma_{zz}}{\sigma_{vo}}$  vs  $\frac{r}{R}$  is shown in Figure 4.18. By considering that the lowest tunnel elevation is at 588.89 m and the lower boundary is set at 578 m, and a diameter of 3.1 m ( $\frac{r}{R} \approx 7.03$ ) the vertical stress field is expected to differ by about 2.9% from the applied gravitational pressure at the selected clearance from the cavity. Given that the finite element model shows a deviation of 4% between these two parameters, the selected boundary conditions are considered to be adequate for the analysis.

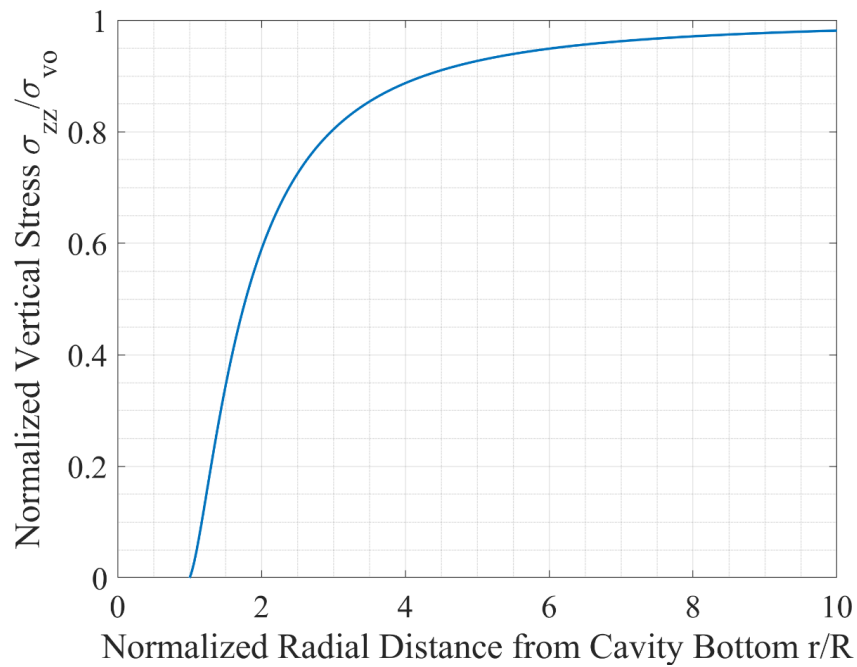


Figure 4.18. Normalized vertical stress vs normalized radial distance.

#### **4.5 Validation and Numerical Convergence of Exterior Geometry**

A geometric model representing Temple 16's exterior geometry was generated in order to investigate the effects of element size and element quality in the overall convergence and accuracy of the finite element solution. The surfaces that represent Temple 16's geometry were exported into Hypermesh where they were used to generate a solid model as shown in Figure 4.19. The solid was then divided into 3 layers that represent the three infill layers at their respective elevations as described in Table 4.1.

Five different meshes were generated from the proposed geometry by using 10-noded tetrahedral elements of different sizes. While a target element size is defined in Hypermesh, elements up to 10% of the target size may be generated to balance the need to mesh finer details of the complex geometry with expected computational expense. For this study, the target element size decreases for each mesh as Table 4.4 shows, leading to a finer mesh density for each model. All meshes are then assigned the same boundary conditions and input parameters to perform the linearly elastic static analysis.



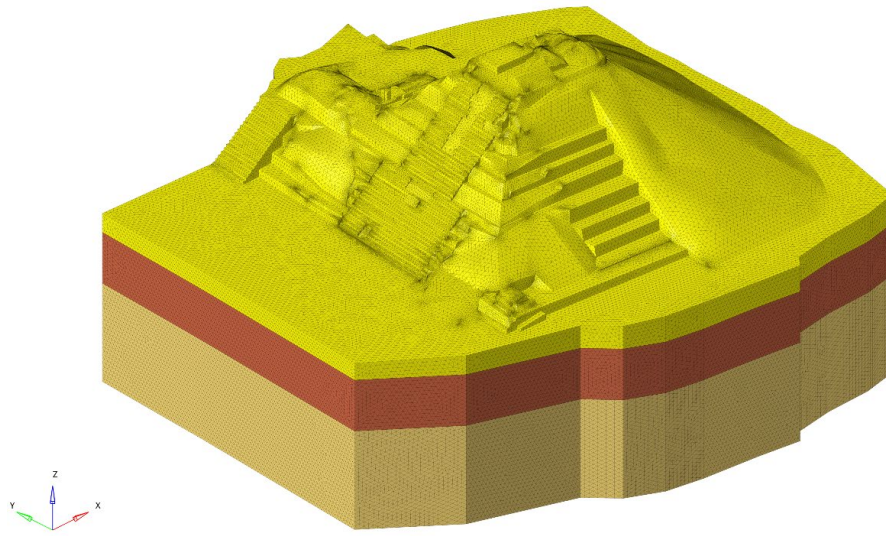


Figure 4.19. View from the southwest of exterior of Temple 16's finite element model.

Table 4.4. Generated mesh densities for convergence study.

<b>Mesh #</b>	<b>Target Element Size (m)</b>	<b>Minimum Element Size (m)</b>	<b>Total Number of Elements <math>N_{els}</math></b>
1	1.500	0.20	671099
2	0.900	0.12	1286967
3	0.750	0.10	1390196
4	0.600	0.08	2402863
5	0.375	0.05	5484847

#### 4.5.1 Convergence Study and Finite Element Results

Figure 4.20 - Figure 4.24 show the obtained vertical stress distribution at the midspan cross-section of the structure along its XZ plane. The fringe scale was set to 30 levels to a numeric precision of 6 significant figures in order to show the precision difference among different mesh densities.

The convergence criteria can be assessed by considering the error order of a given mesh. The error order  $O$  is a function of the characteristic length of an element  $h$ . This is  $O(h^q)$  where  $q$  is the difference between the element's highest complete polynomial order  $p$ , and the  $r$ th derivative of the field quantity:  $q = p + 1 - r$ . For this analysis, second order polynomials are used to approximate the displacement field within the system. Considering the stress and strain fields as first order derivatives of the displacement field, then  $q = 2$ . Finally, the element length can be approximated by the relationship:

$$h = (N_{els})^{-\frac{1}{n}} \quad (4.11)$$

Where  $N_{els}$  is the total number of elements that make up the mesh, and  $n$  is the dimensionality of the model. By considering this expression and  $n = 3$ , the error order is then a function of  $(N_{els})^{-\frac{2}{3}}$ . Furthermore, if convergence is achieved, this criterion can be utilized to approximate the exact solution of the system, or when the characteristic element size is 0 (continuous media condition). This is achieved by multi-mesh extrapolation, or Richardson's extrapolation formula (2001):

$$\phi_{\infty} = \frac{\phi_1 h_2^q - \phi_2 h_1^q}{h_2^q - h_1^q} \quad (4.12)$$

where  $\phi_{\infty}$  corresponds to the converged solution when  $h = 0$ . To test convergence, the obtained maximum compressive vertical stresses were recorded from each mesh and computed against  $h^q = (N_{els})^{-\frac{q}{n}}$ , as shown in Figure 4.25. A best-fit line was obtained via least-square methods. The vertical intercept of this line corresponds to  $\phi_{\infty}$ .

The R-squared value of 0.945 obtained for the best-fit line in Figure 4.25 shows that there is an acceptable level of correlation among the data points, and the linear trend confirms convergence of the model as a function of decreasing element size. Therefore, from this analysis, the converged exact solution for maximum vertical compressive stress is set to be at 632.745 KPa.

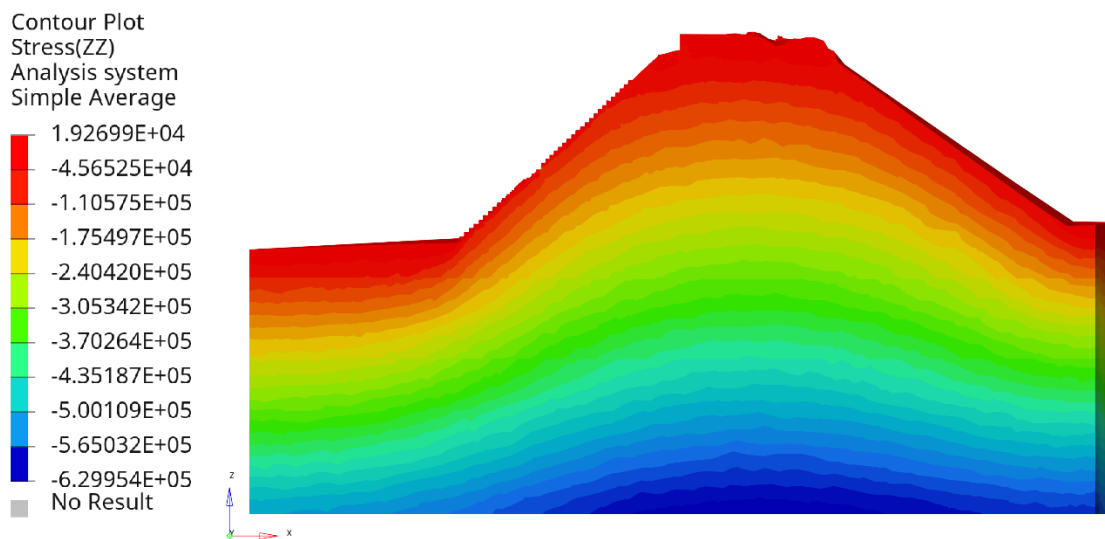


Figure 4.20. Vertical stress distribution of mesh #1 at the XZ plane.

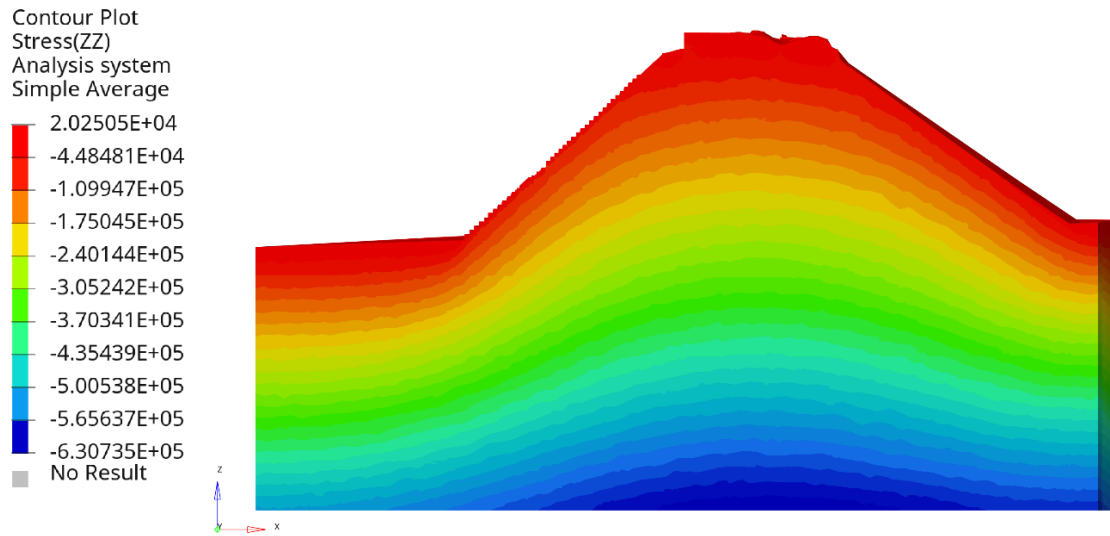


Figure 4.21. Vertical stress distribution of mesh #2 at the XZ plane.

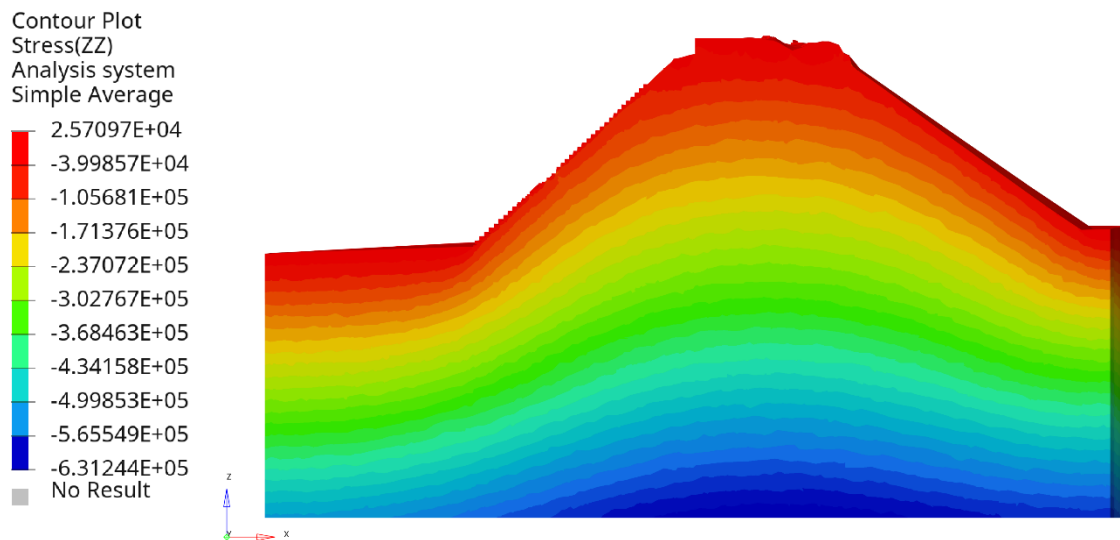


Figure 4.22. Vertical stress distribution of mesh #3 at the XZ plane.

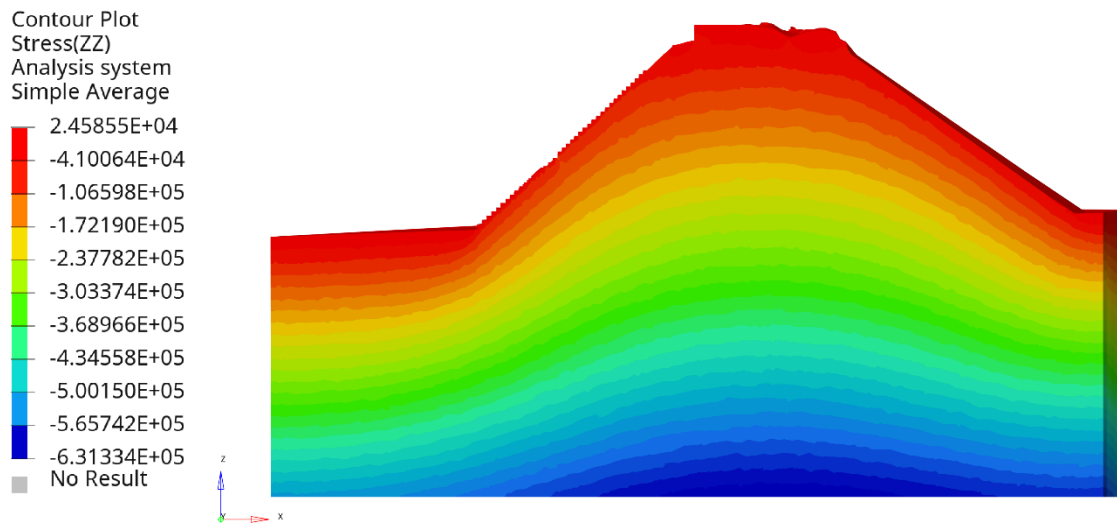


Figure 4.23. Vertical stress distribution of mesh #4 at the XZ plane.

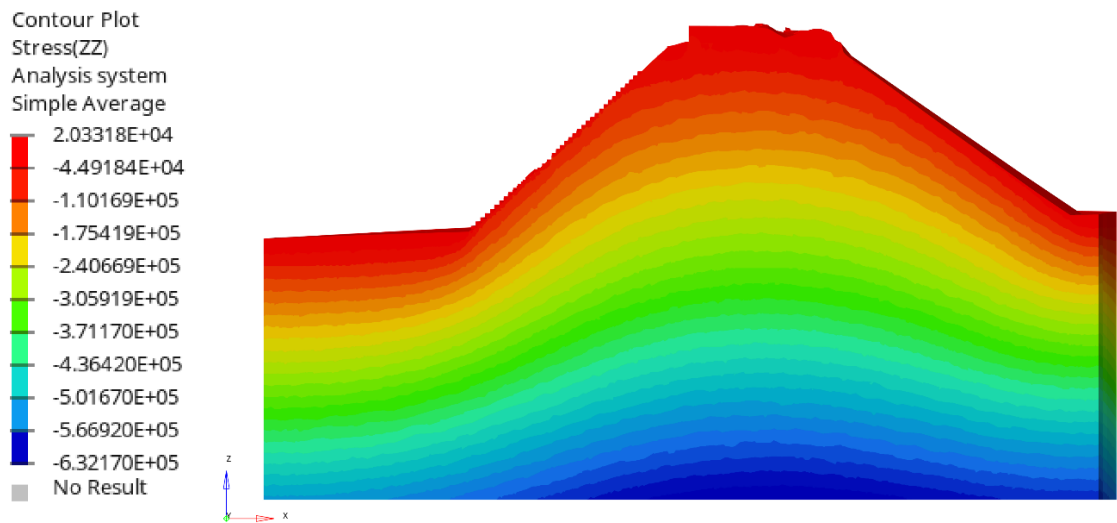


Figure 4.24. Vertical stress distribution of mesh #5 at the XZ plane.

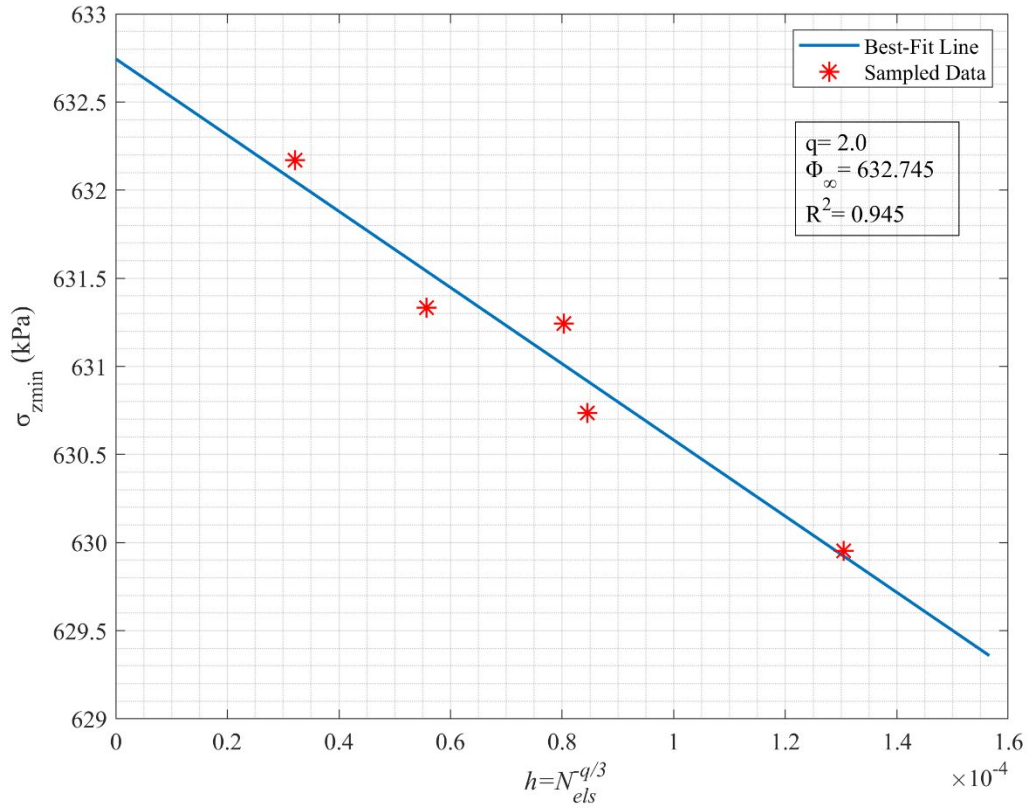


Figure 4.25. Convergence study of exterior of Temple 16's meshes.

#### 4.5.2 Closed Form Solution Approximation for Bearing Pressure

The vertical stress at any elevation level below grade can be approximated by the following equation:

$$\sigma_{zz}(z) = \sum \gamma_i \cdot (z - \Delta h_i) + \Delta \sigma_z(z) \quad (4.13)$$

where  $\sum \gamma_i \cdot (z - h_i)$  is the sum of the self-weight of the overlying infill layers above the elevation  $z$  of interest,  $\gamma_i$  is the unit weight for a given infill layer and  $\Delta h_i$  is the elevation where there is a change infill material.  $\Delta \sigma_z(z)$  is the stress contribution of the superstructure weight into the total applied vertical stress. For validation purposes,

Temple 16's cross-section can be approximated as an asymmetrical, infinitely long, embankment as shown in Figure 4.26.

The stress increase due to an asymmetrical embankment can be derived from Boussinesq's equations for triangular loading and by performing superposition. The final expression for the stress increase  $\Delta\sigma_z$  is:

$$\Delta\sigma_z = \frac{q}{\pi} \left[ (\alpha_1 + \alpha_2 + \alpha_3) + \left( \frac{b_1}{a_1} \right) (\alpha_1 + R\alpha_3) + \left( \frac{x}{a_1} \right) (\alpha_1 - R\alpha_3) \right] \quad (4.14)$$

where  $q$  is the embankment's self-weight,  $R = \frac{a_1}{a_2}$  and  $\alpha_1, \alpha_2$  and  $\alpha_3$  are inclination angles that are a function of location of the point of interest (Figure 4.27). By using Equations 4.13 and 4.14, a contour plot showing an approximated vertical stress distribution for the infill below grade was coded in MATLAB and shown below in Figure 4.28.

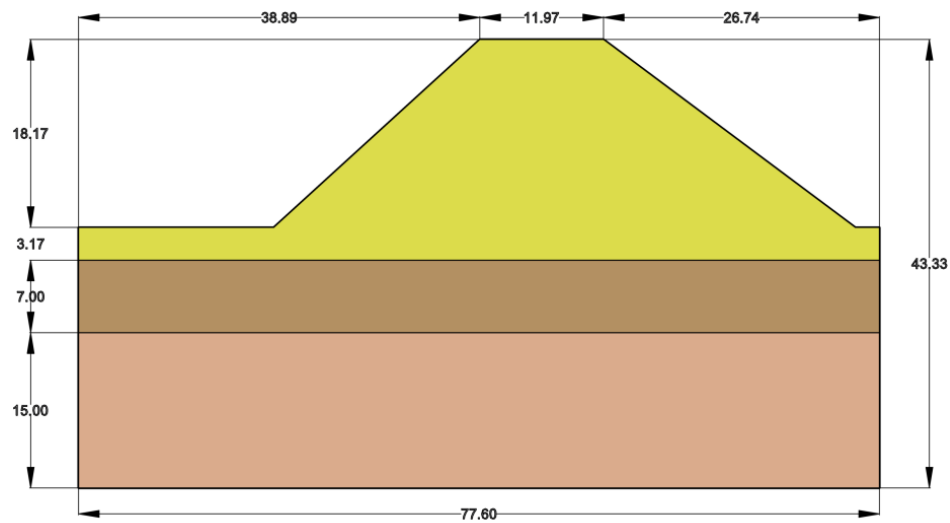


Figure 4.26. Proposed embankment profile for approximating closed-form solution (units in meters).

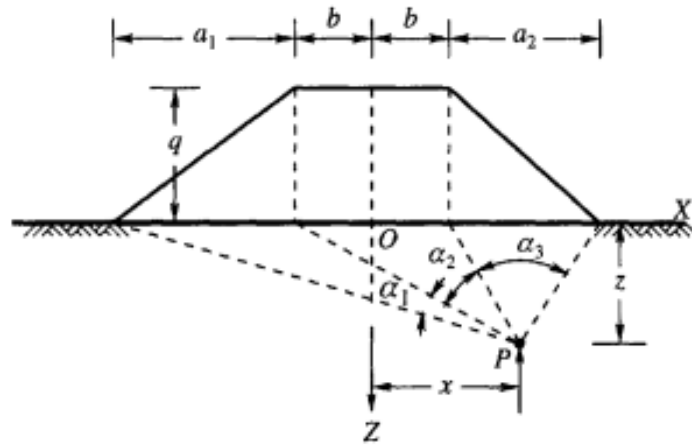


Figure 4.27. Stress increment due to asymmetric embankment at a point “P” (Murthy).

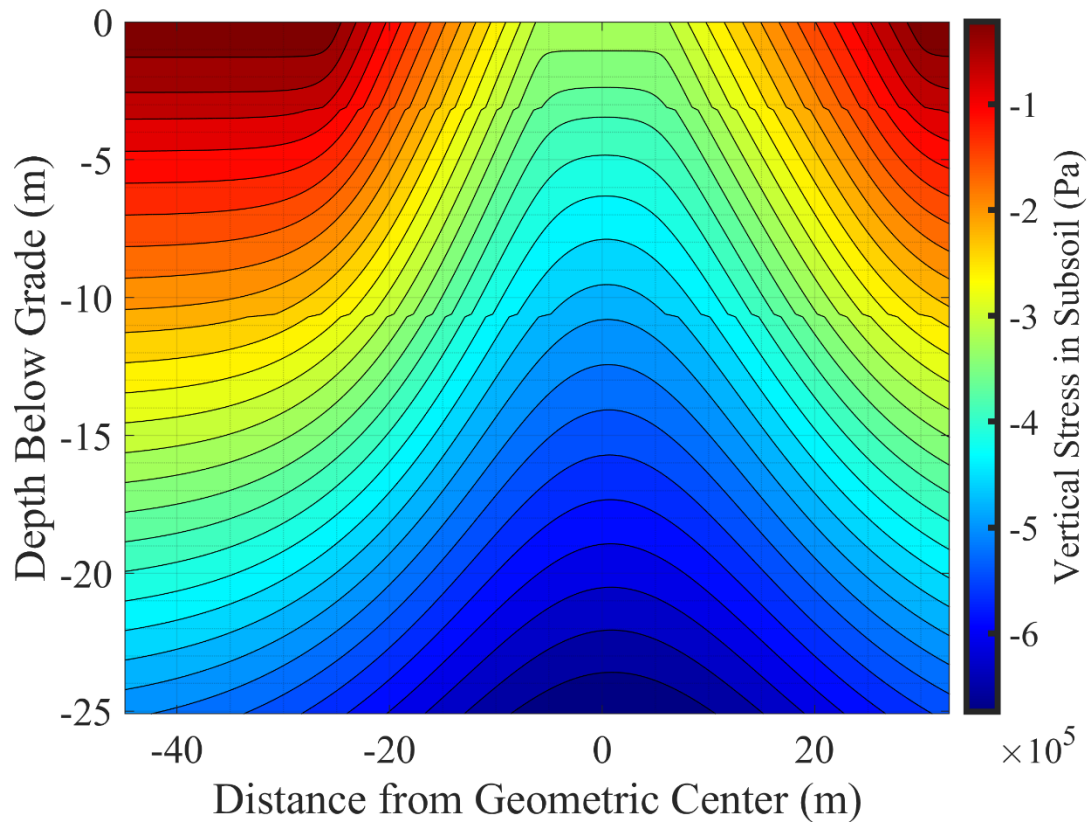


Figure 4.28. Vertical stress distribution in infill below grade of Temple 16.



### 4.5.3 Model Validation

From Equations 4.13 and 4.14, and Figure 4.28, the maximum compressive vertical stress computed via the assumed closed-form solution is 673.375 KPa. By comparing this result with the ones obtained from the generated meshes are within 6.11 and 6.44% of error with respect to the proposed closed form approximation. Furthermore, the approximated converged solution  $\phi_{\infty} = 632.745$  KPa is within 6% error with respect to the proposed closed-form approximation. These margins of error are acceptable considering the geometric oversimplifications made for deriving the closed-form approximation. Therefore, the proposed meshing procedures and system characterization are adequate to produce reliable results within an acceptable margin of convergence.

## CHAPTER 5 – RESULTS AND ANALYSIS

### 5.1 Chapter Overview

Previous chapters explored the process followed to generate the desired geometries based on collected field data (Chapter 3) and the process followed to generate and validate a finite element model of Temple 16 (Chapter 4). The present chapter aims to analyze this finite element model to identify areas of concern and to understand the influence of buried structures on each other and the overall tunnel system. Six configurations of Temple 16's finite element model are analyzed and discussed, which include variations of tunnel excavations and back-filling. The first pair of these configurations compare the influence of the tunnel system and include the current state of Temple 16, which includes Rosalila and existing tunnels, and the past state of Temple 16 before any tunnels were excavated. The second pair of configurations study the influence of lower-level and upper-level tunnels on their stress states by defining hypothetical scenarios where upper-level tunnels are filled and vice-versa. For these configurations, the elevation of 598 meters was selected as the dividing line between the upper and lower tunnels. Finally, the last pair of configurations study the impact of two proposed conservation actions to alleviate Rosalila's deterioration in its southern side and central room. Because of Copán's geographic location and the existing concerns of heavy rainy season affecting the stability of archaeological tunnels, all configurations were analyzed at three different extreme infill saturation levels (90%, 70%, 50%) to understand the influence of pore water pressure in areas of extreme stress concentration.

This chapter is divided into two main sections to present the proposed configurations and the obtained results and analysis of this investigation. The first half of this chapter explains the different model configurations and the goals behind the analysis of each selected configuration. This section also explains the general scope and capabilities behind the selected linearly elastic analysis approach and its limitations concerning the obtained results and their interpretation. Finally, the second half of this chapter summarizes the obtained results and analyzes the observations made based on the established goals of this investigation. The last section divides general observations regarding the general stress behavior of Temple 16 from the observations made on areas of concern along the tunnel system and within excavated areas of Rosalila. Finally, this section analyzes the effects of proposed conservation ideas on Rosalila and its stress behavior on the areas of interest and the surrounding tunnels.

## **5.2 Model Configuration**

### **5.2.1 Objectives**

As was explained in Section 2.2 of this thesis, the excavation process of the archaeological tunnels around Temple 16's buried structures had brought a series of technical and environmental problems that compromise the stability of excavated tunnels, and the conservation of exposed sections of underlying structures such as Rosalila and Oropéndola. As it was shown in Section 4.4, the presence of cavities within an elastic media, like tunnels with Temple 16, creates areas of stress concentration that are a function of the cavity's geometry, material, and surrounding conditions. With the collected lidar data, it was possible to generate high-fidelity geometries of the tunnel

system that are aligned in space with Temple 16 and Rosalila. By characterizing the system with the assumed infill parameters described in Section 4.3.1, it is possible to study and analyze the stability of the tunnel system, which can provide a better understanding of the current flow of stresses, the influence among existing structures, and identify areas of concern.

A current concern regarding Rosalila's deterioration is related to the current state of excavation at Rosalila's southern wall (Figure 5.1 & Figure 5.2), where excavation activity has impacted Rosalila's masonry façade at the southwest (Figure 5.3), and southeast ends (Figure 5.4). By comparing the aligned Replica's point cloud with Rosalila's exposed areas from the tunnels, it is possible to notice that excavation processes have created overhangs or depressed areas that are up to 28.8 cm and 56.6 cm deep with respect to the original exterior façade at the southwest (Figure 5.3) and southeast ends (Figure 5.4). Therefore, the three-dimensional nature of the generated geometries can provide a better understanding of how the proposed idea of filling Rosalila's center room can impact the stability of tunnels lying directly underneath this structure.



Figure 5.1. View from the south of Rosalila's southern side with surrounding tunnels.

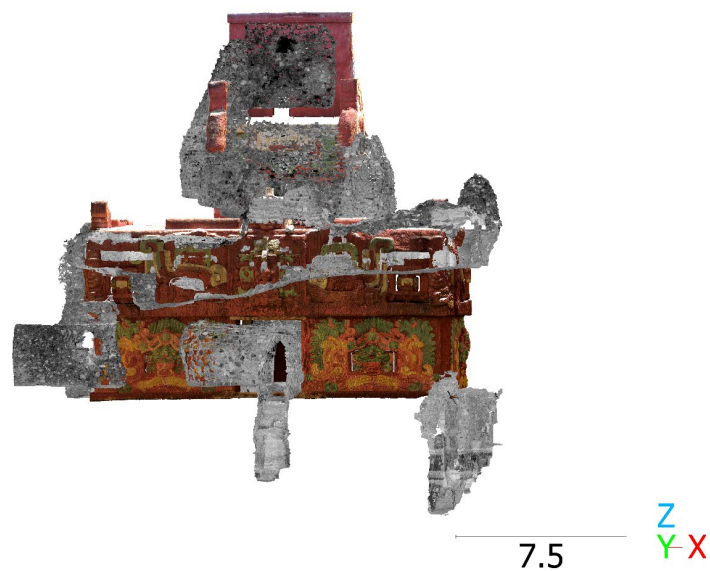


Figure 5.2. View from the south of Rosalila's southern side showing overlapped tunnels section on upper wall section.

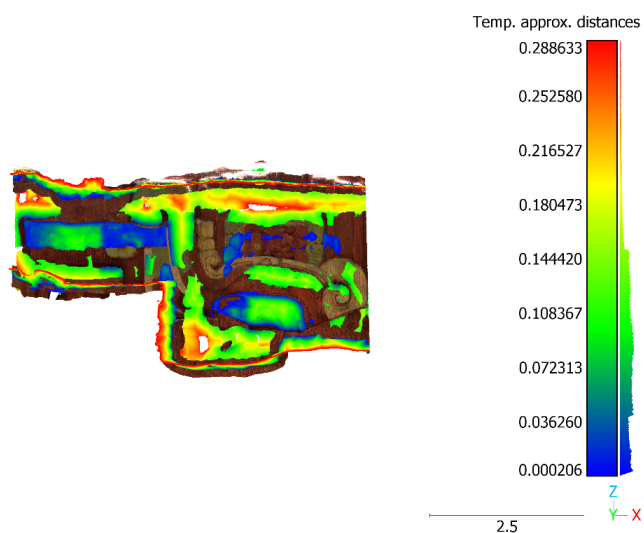


Figure 5.3. Rosalila's southwest corner: comparison between replica's exterior surface and Rosalila's current state due to tunnel excavation.

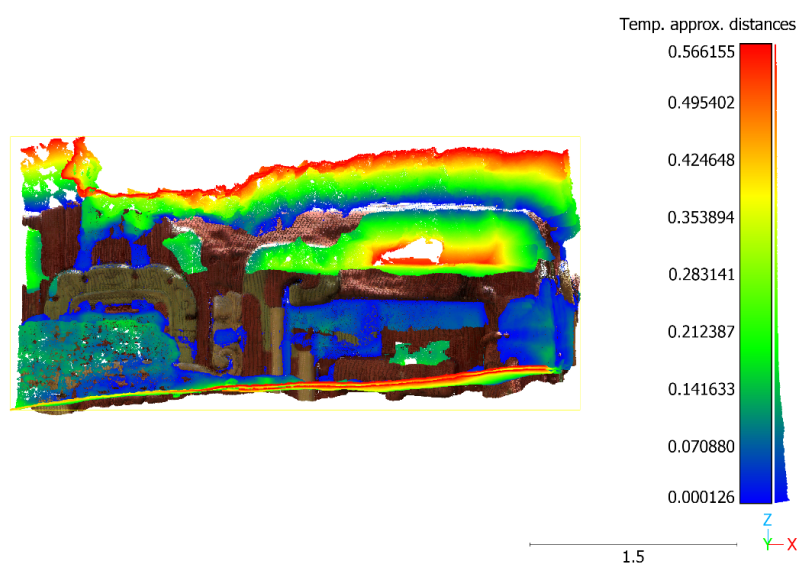


Figure 5.4. Rosalila's southeast corner: comparison between replica's exterior surface and Rosalila's current state due to tunnel excavation.

The six proposed configurations, or variations of Temple 16's finite element model, are listed in Table 5.1 and have been organized into pairs. The first pair (Configuration A and B) reflect the current state of Rosalila and its surrounding archaeological tunnels within Temple 16 (Configuration A), and the original state of Temple 16 prior to any tunnels being excavated (Configuration B). The second pair of the list (Configurations C and D) represent extreme hypothetical cases of tunnel filling. The goal of these configurations is to understand the influence of stress concentration levels between tunnels at elevations located below Rosalila (categorized as lower-level tunnels), and tunnels located at the same or higher elevations (categorized as upper-level tunnels). To separate tunnels into these two categories, the elevation of 598 meters was selected as the dividing line, given its relationship to Rosalila's elevation (601.7 meters) and the typical lowest elevation of its surrounding tunnels. In this sense, these pairs represent the hypothetical cases when only upper-level tunnels are excavated (Configuration C), and when only lower-level are excavated (Configuration D). Finally, the last pair of configurations (Configurations E and F) aim to analyze potential Rosalila-specific conservation efforts. Configuration E explores the scenario in which Rosalila's center room is backfilled to analyze the impact of this proposed into lower-level tunnels. Configuration F focuses on the benefits of backfilling overhanging areas of Rosalila's southern wall to the local stability and stress concentrations of this specific area. For configurations C to F, it is assumed that the backfilled areas will be filled with typical surrounding material corresponding to Rosalila (Configurations E and F) and the

respective infill material (Configurations C and D). More detailed illustrations of the geometries for each configuration can be found in Section 5.2.3 of this chapter.

Table 5.1. Proposed analysis configurations and comparison cases.

<b><i>Configuration</i></b>	<b><i>Description</i></b>	<b><i>Compared to</i></b>
A	General Case (As-Is)	All Other Configurations
B	Temple 16 prior to Any Tunnel Excavation	Configurations A,E,F
C	Only Tunnels Above 598 meters of Elevation	Configuration A
D	Only Tunnels Below 598 meters of Elevation	Configuration A
E	Rosalila's Center Room Backfilled	Configuration A and B
F	Rosalila's South Wall Façade Repaired	Configuration A, B and D

The proposed configurations listed in Table 5.1 will be used to generate finite element models for the analysis of Temple 16, Rosalila, and archaeological tunnels. The results obtained for each configuration will be compared with their relevant counterparts, as listed in Table 5.1. For analyzing the current state of the tunnel system and the influence among existing tunnel sections, Configuration A will be used as the general base case that will be compared to Configurations C, D, and E. Configuration B analysis will provide a general understanding of the native stress field and stress distribution within Temple 16 and Rosalila to establish a correlation between the existing stress field and the tunnel affected areas. Rosalila's stress concentration patterns observed in Configuration A will be compared with the results obtained in Configurations B, D, and E to understand better how the proposed conservation ideas can impact the current state of the structure.

As it was explained in Chapter 4, each generated finite element model would be analyzed with the inputs and boundary conditions specified in Sections 4.2 and 4.3 via a



linearly elastic static analysis approach performed by the LS-DYNA solver. Three saturation levels were defined based on the Pires et al. (2021) study to assess the influence of the extreme rainy season on the increase in stress in affected areas. These saturation levels correspond to 90%, 70%, and 50% water saturation levels in the upper (girún) and middle (tierra café oscuro) infill material layers. Due to its close proximity to the water table, the lower barro layer will be assumed to be under 100% saturation for all analysis purposes. The additional water weight due to the different levels of saturation is modeled via the following relationship:

$$\rho_{\text{sat}} = \rho_{\text{layer}} + c \cdot \rho_{\text{water}}$$

where  $\rho_{\text{sat}}$  is the total density of an infill layer at a given saturation level “c”,  $\rho_{\text{layer}}$  is the originally assumed infill material density (refer to Table 4.2 and  $\rho_{\text{water}}$  is the water density at ambient conditions ( $1,000 \frac{\text{kg}}{\text{m}^3}$ ). Table 5.2 summarizes the target densities of each infill layer at a target saturation level. Given the three proposed saturation levels, each configuration's generated finite element models will be used to perform linearly elastic analyses at each target saturation level, leading to 18 different LS-DYNA simulations.

Table 5.2. Considered saturation levels for analysis of each infill layer.

<i>Degree of Saturation</i>	<i>Girón (Yellow Sand)</i>	<i>Tierra Café Oscuro (Reddish-Brown Soil)</i>	<i>Barro (River Mud)</i>
0 % (No Saturation)	1733.63	1886.60	1937.59
50% Saturation	2233.63	2386.60	-
70% Saturation	2433.63	2586.60	-
90% Saturation	2633.63	2786.60	-
100% Saturation	-	-	2937.59

### 5.2.2 Analysis Approach Limitations

The current LS-DYNA input parameters are calibrated to perform a linearly elastic static analysis on each generated finite element model. This is a conservative assumption when considering that the infill material will also experience plastic deformations around the surrounding tunnels. From a theoretical point of view, two important differences arise between linearly elastic and elastic-plastic infill material assumptions: (1) location of maximum stress within the cavity's surrounding areas and (2) stress required to provide stability to avoid collapse. Figure 5.5 contrasts the obtained stress distributions around a circular cavity from a linearly elastic assumption (top) and an elastic-plastic media. As it was explained in section 4.4, the maximum stress concentration for a linearly elastic cavity occurs around its cross-section, which decreases as a function of the ratio between the radial distance and the cavity's radius. For an elastic-plastic cavity, media surrounding the cavity's cross-section would reach yielding and decrease its strength, creating an aureole of yielded ground (Figure 5.5, bottom). The decrease in strength will cause the maximum stress to be shifted to the outside of this

aureole into the surrounding media. Finally, the second implication between elastic and elastic-plastic approaches implies that cavities under elastic conditions will not need additional supporting stress to avoid collapse. As the media surrounding the cavity exceeds its yielding capacity, the overall strength reduction will trigger collapse mechanisms that can only be avoided by including supporting elements with enough strength to balance the applied radial stress.

These two main contrasts imply that results from the linear elastic analysis described herein are sufficient to identify areas of concern based on stress concentration levels. Based on the first implication, areas that exhibit stress concentrations in the results are expected to represent areas at risk of collapse due to local overload. However, the results will not reflect any local failure due to material instability and collapse mechanisms. The decision to perform a linearly elastic analysis instead of an elastic-plastic analysis (also known as non-linear analysis) is based on computational efficiency and in light of the uncertainties regarding properties of infill and tunnel consolidation materials, as well as the lack of information regarding actual infill distribution through Temple 16. Therefore, the obtained results are expected to provide a qualitative understanding of the current state of Rosalila and Temple 16 tunnels and the contributing mechanical factors creating areas at risk of failure due to stress concentrations. Due to these limitations, the obtained results will be reported as relative quantities (stress increases) that are the product of the proposed comparisons. These results will be accompanied by figures showing the respective areas of concern.

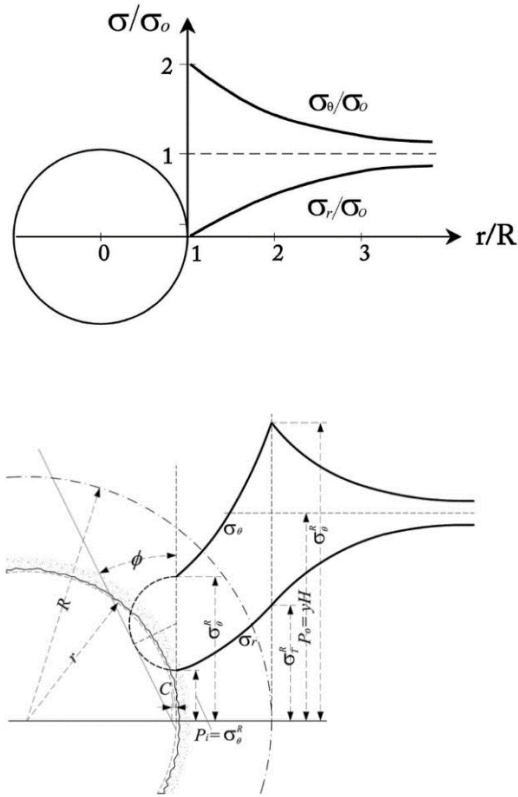


Figure 5.5. Comparison of expected stress distributions around a circular cavity surrounded by media modeled as linearly elastic (top) and elastic-plastic (bottom).

### 5.2.3 Configuration Geometry

Six different finite element models were created based on the configurations listed in Table 5.1 and described in Section 5.2.1. As explained in Section 4.2, the solid meshes for each configuration are made of second-order tetrahedral elements. To minimize computational costs while still being able to represent key geometric features, meshes were generated with an average element size of 1.0 meter and a minimum element size of 10 cm (0.1 meters). From Section 4.5, it was shown that this selected element size range will still provide results within a 10% deviation from the converged solution. Therefore,

the generated results from the finite element method are expected to be within an acceptable margin of confidence.

The typical exterior layout of Temple 16's mesh is shown in Figure 5.6 and Figure 5.7. Given that the proposed configurations do not affect the exterior geometry of Temple 16, all the meshes generated for each configuration show the same exterior outlook with minimal changes in the element distribution due to the meshing algorithm. Figure 5.8 and Figure 5.9 show the typical exterior look of Rosalila for Configurations A, C, and E. As Figure 5.9 shows, the southern wall geometry has been modified to match the current state of this area due to the excavation activities. This was not the case for Configurations B, D, and F. From the definitions provided in Table 5.1, Configuration B does not include any tunnels (Figure 5.10 & Figure 5.11). Configuration D simulates that upper tunnels have been filled. Finally, the southern wall geometry in Configuration F was not modified to simulate the scenario where this wall part is backfilled (Figure 5.12 & Figure 5.13). Finally, Figure 5.14 shows transparent views of Rosalila after incorporating its inner tunnels. This configuration is typical except for Configuration B and D, where no upper-level tunnels are included, and Configuration E, where the center room is filled (Figure 5.15).

Transparent views of Configuration A are shown in Figure 5.16, Figure 5.17 and Figure 5.18. Section 5.2 explains that this case includes all current tunnels that surround and are directly below Rosalila. These views also represent Configurations E and F since those cases do not account for hypothetical tunnel backfilling scenarios. Tunnels included for Configuration C are shown in Figure 5.19 and Figure 5.20. These configurations only

include upper-level tunnels that lie above 598 meters of elevation. However, if a continuous section of these tunnels lies partially below this elevation line, the underlying section was still accounted for in this configuration for continuity purposes. Finally, Figure 5.21 and Figure 5.22 show the tunnels included for Configuration D, which correspond to lower-level tunnels that lie completely below the diving elevation line.

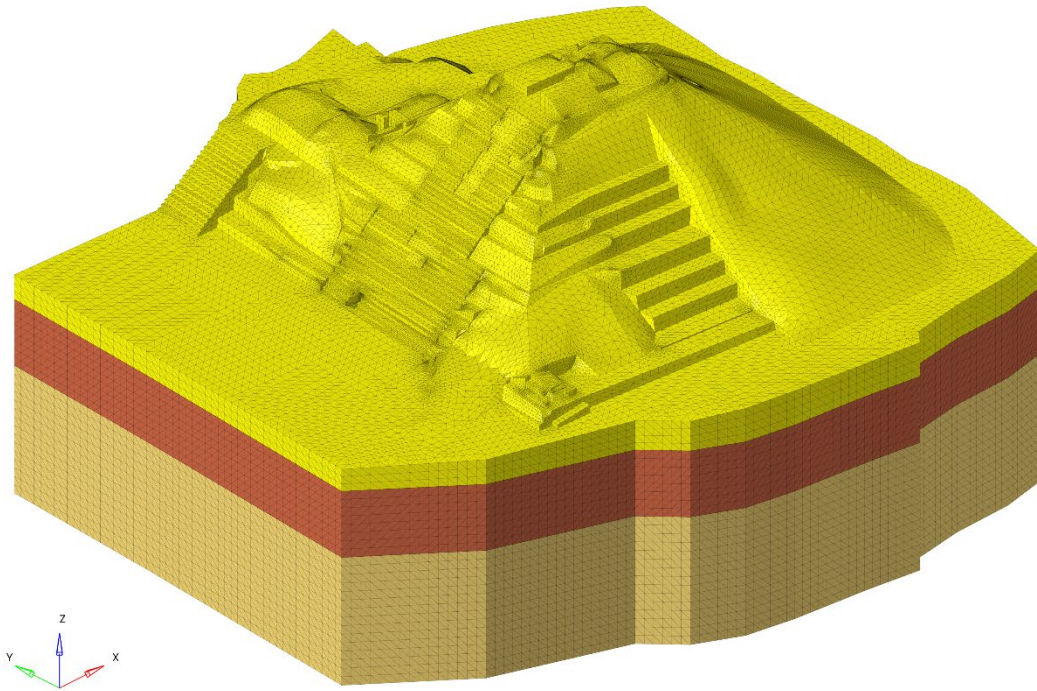


Figure 5.6. View from the southwest of Temple 16's exterior mesh (typical for all proposed configurations).

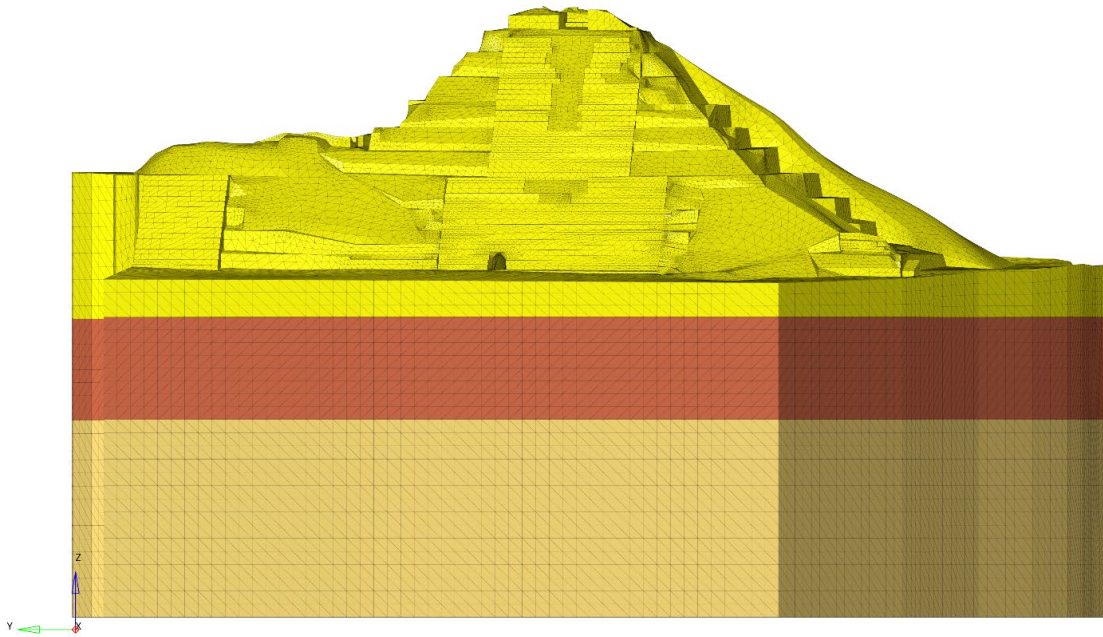


Figure 5.7. View from the west of Temple 16's exterior mesh (typical for all proposed configurations).

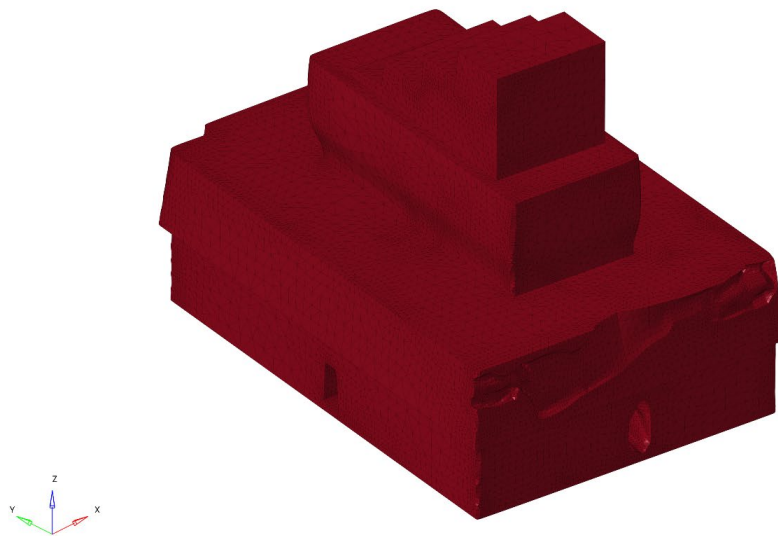


Figure 5.8. View from the southwest of Rosalila's exterior mesh (typical for configurations A, C, E).



Figure 5.9. View from the south of Rosalila's exterior mesh (typical for configurations A, C, E).

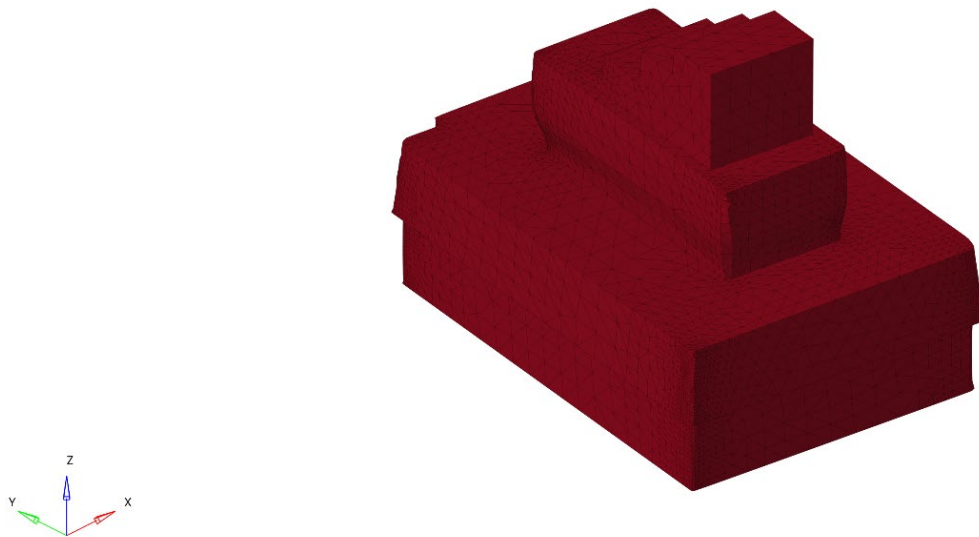


Figure 5.10. View from the southwest of Rosalila's exterior mesh for configurations B and D.



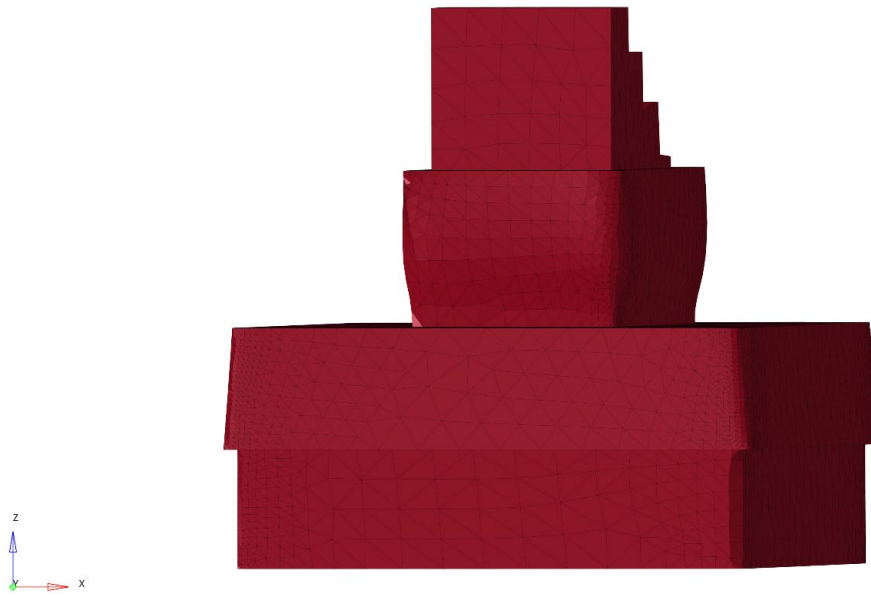


Figure 5.11. View from the south of Rosalila's exterior mesh for configurations B and D.

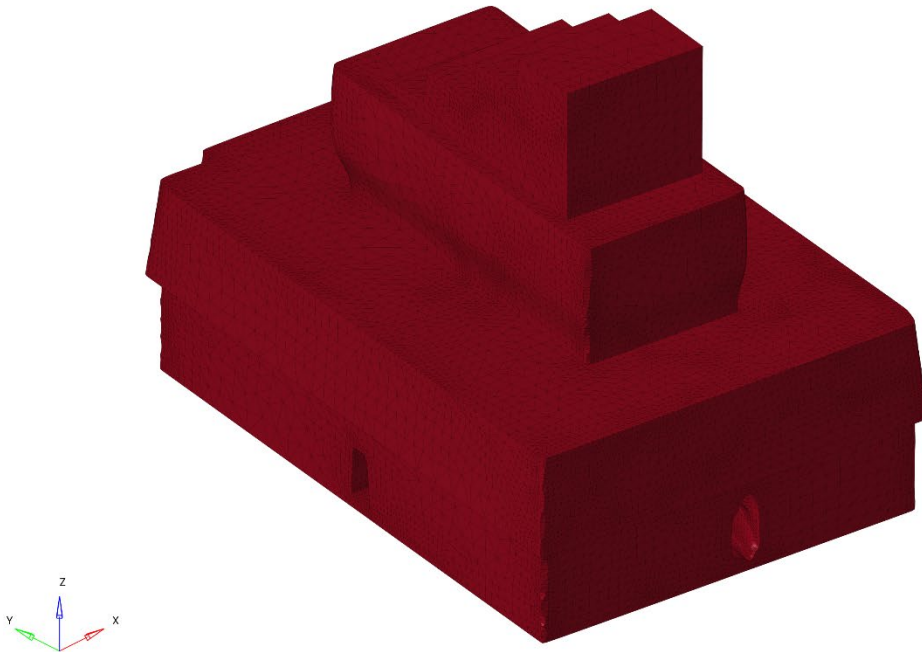


Figure 5.12. View from the southwest of Rosalila's exterior mesh for configuration F.

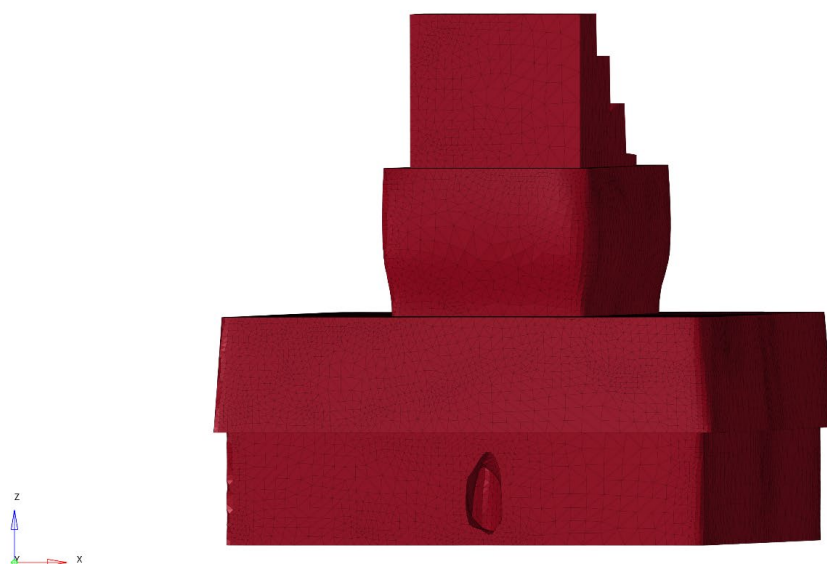


Figure 5.13. View from the south of Rosalila's exterior mesh for configuration F.

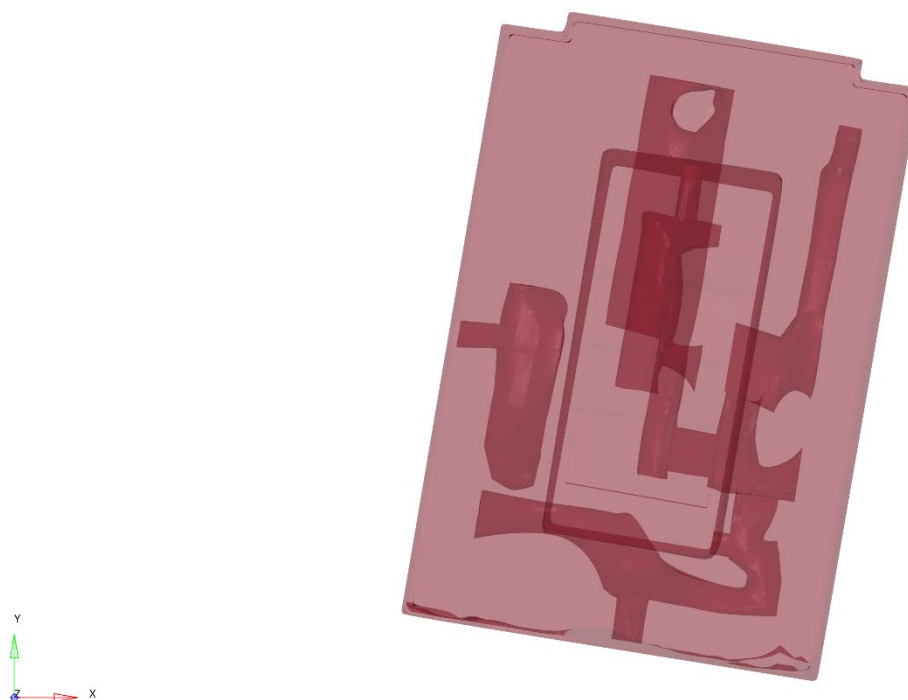


Figure 5.14. Plan view showing excavated areas within Rosalila (typical for configurations A, C, F).

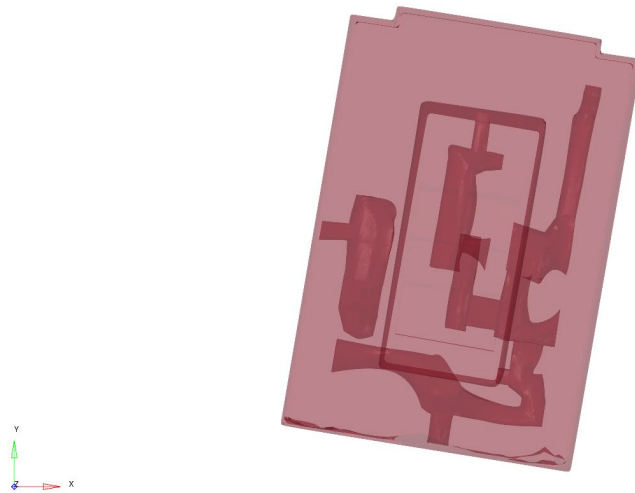


Figure 5.15. Plan view showing excavated areas within Rosalila for configuration E  
(center room has been filled).

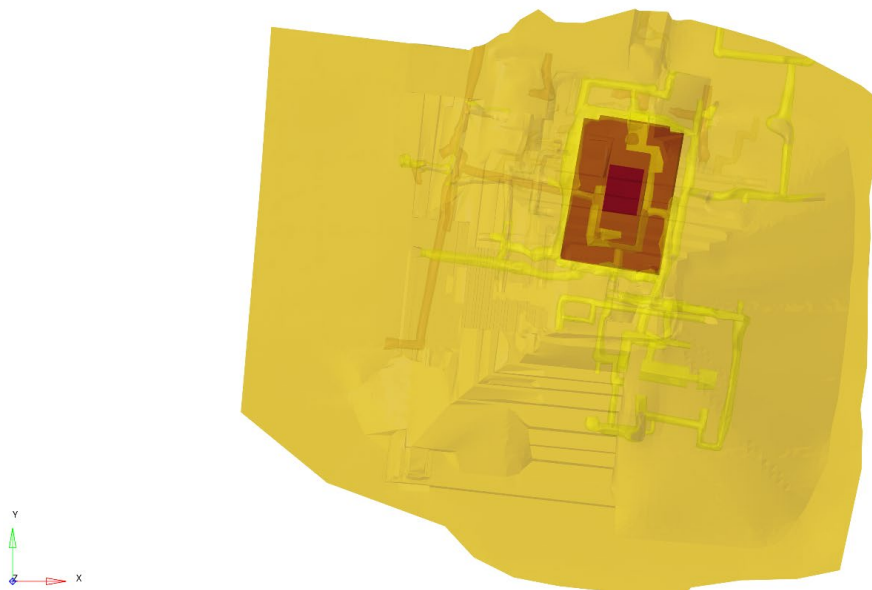


Figure 5.16. Plan view showing tunnel system modeled for configuration A.

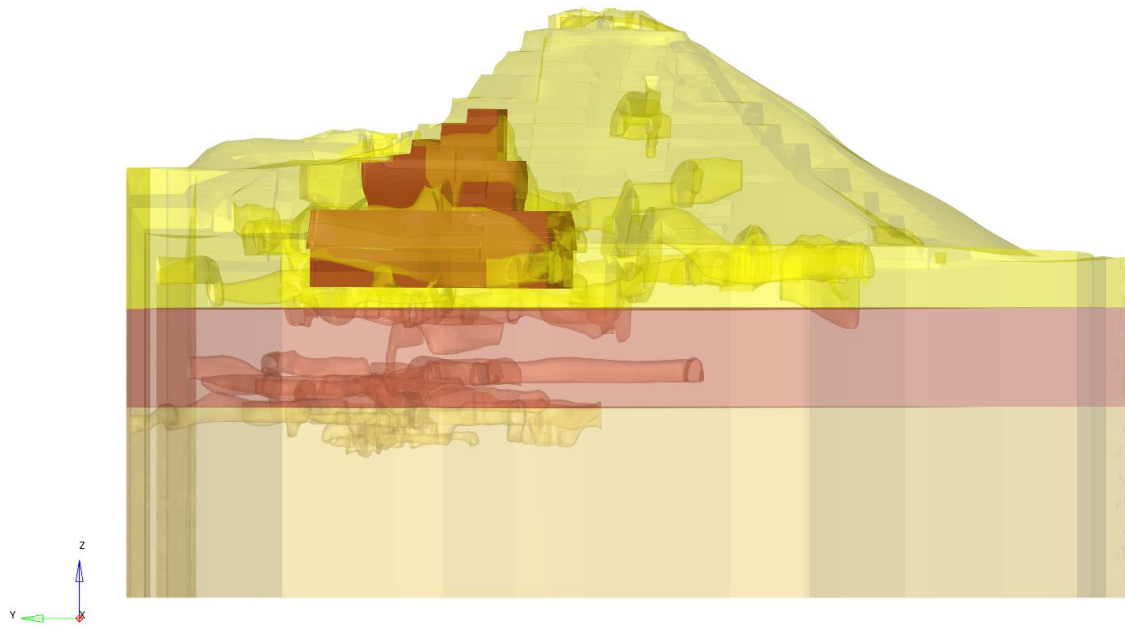


Figure 5.17. View from the west showing tunnel system modeled for configuration A.

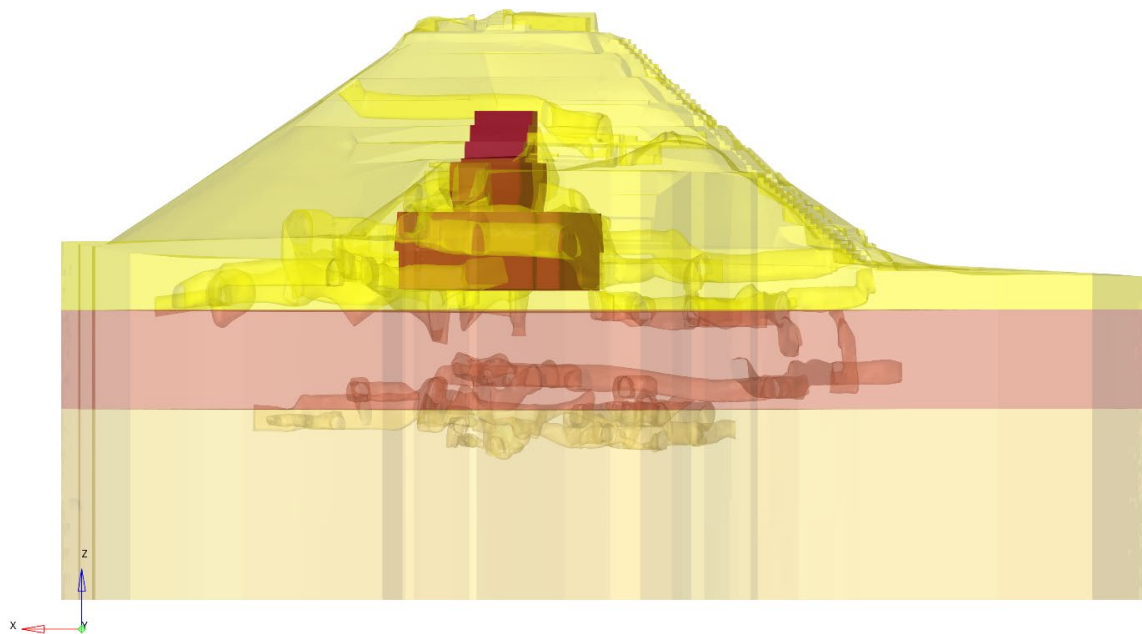


Figure 5.18. View from the north showing tunnel system modeled for configuration A.

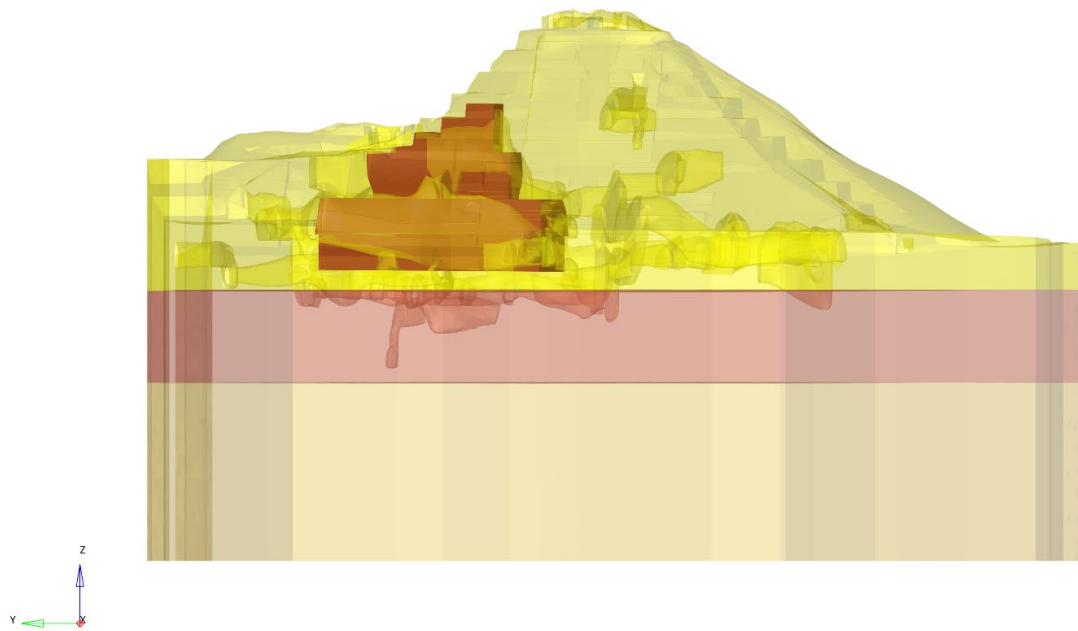


Figure 5.19. View from the west showing tunnel system modeled for configuration C.

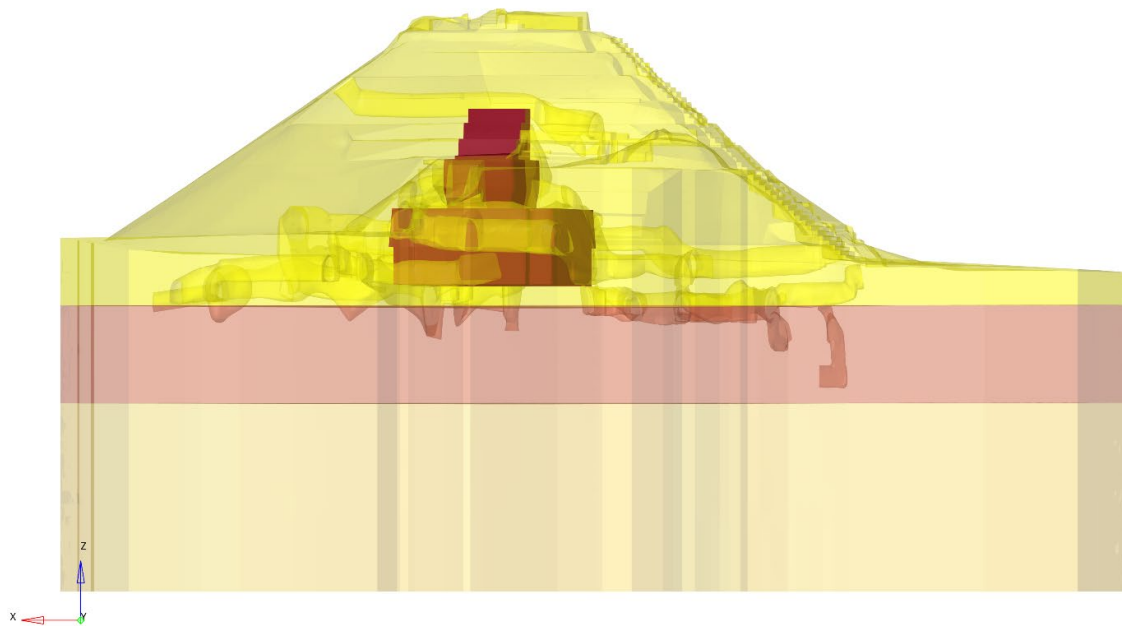


Figure 5.20. View from the north showing tunnel system modeled for configuration C.

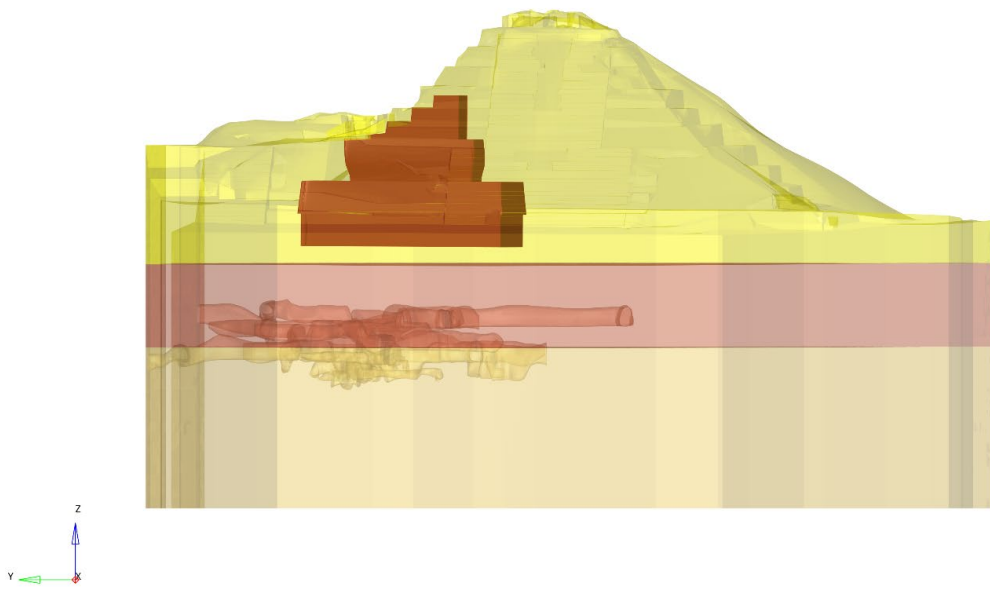


Figure 5.21. View from the west showing tunnel system modeled for configuration D.

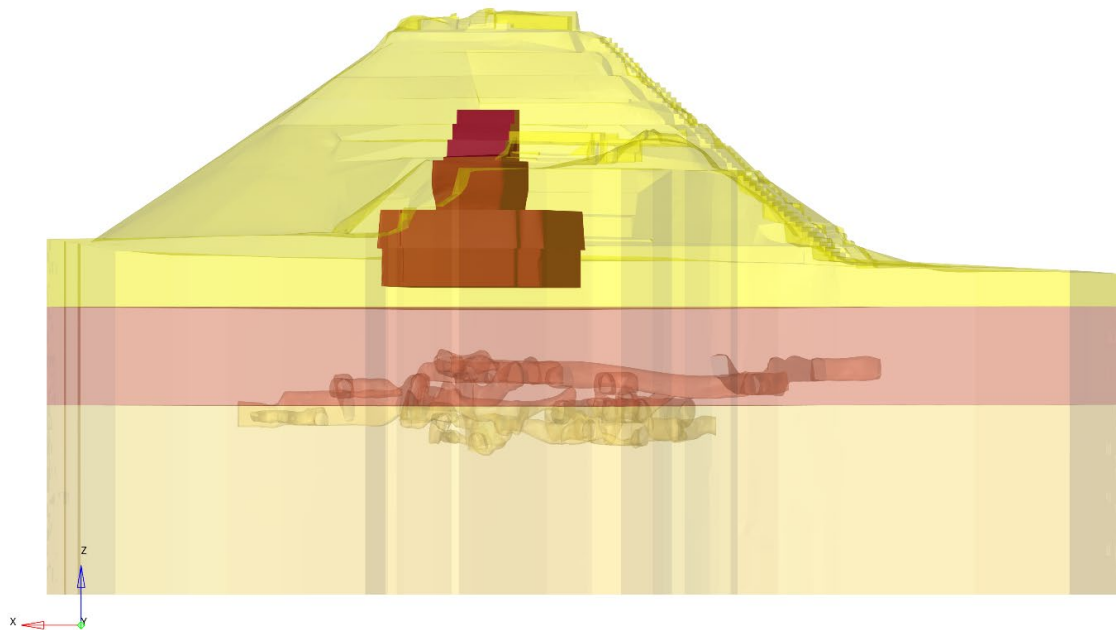


Figure 5.22. View from the north showing tunnel system modeled for configuration D.

## 5.3 Results and Discussion

### 5.3.1 General Remarks on Temple 16 without Tunnels

Eighteen different finite element models representing each geometric configuration and saturations levels were analyzed via LS-DYNA's MPP solver under the linearly elastic analysis approach. Configuration B results can be used to obtain a general understanding of Temple 16's stress field without the influence of the tunnels. Figure 5.23, Figure 5.24 and Figure 5.25 present contour plots of the stress distribution within Temple 16 cross-sections. In general, and as expected, the stress increases as a function of depth; however, the buried Rosalila structure impacts the general load flow. As seen in the contour plots, the presence of Rosalila causes a shift of the peak stress from the geometric centroid of Temple 16 to the southern portion of Rosalila on the upper and middle infill layers.

The stress concentrations agree with the assumption that Rosalila's material has a higher stiffness than the surrounding infill, which creates stress concentrations at the locations with sharp geometric changes, such as corners or edges of the structure. In addition, the southern side of Rosalila is expected to show higher stress concentrations due to its proximity to the geometric centroid. The offset between Rosalila and Temple 16's centroidal axis greatly influences the stress concentrations observed in the second and third levels of Rosalila.

The effect of mass accumulation as a function of depth can be observed at the base of Rosalila. The southern corners of Rosalila transmit higher stress to the infill than the northern ones (Figure 5.26). The combined effect of the supported infill's weight and

Rosalila's self-weight (surcharge load) creates an influence region that mainly affects the upper and middle infill layers. The effect of the surcharge load is uniformly spread throughout the lower infill layer, and its influence decreases as a function of depth, which matches with field observations regarding the mechanical stability of this infill material. Figure 5.27 and Figure 5.28 show isosurfaces of the areas that are influenced by the surcharge load on the upper and middle infill layer regions. These isosurfaces represent regions with stress levels that are equal or higher than the median Tresca stress value reported for Temple 16 contour scale (Figure 5.23 to Figure 5.25) when no tunnels are accounted for in the geometry (Configuration B). The median value was selected for the isosurface threshold to isolate the areas primarily affected by the presence of Rosalila in the upper and middle infill layers. Figure 5.27 and Figure 5.28 show that the effects of the load transferred from the southern side of Rosalila spread up to radial distances of 15 and 16 meters for the upper and middle layers. These radial distances are constant for all saturation levels as they solely depend on the system's geometry.



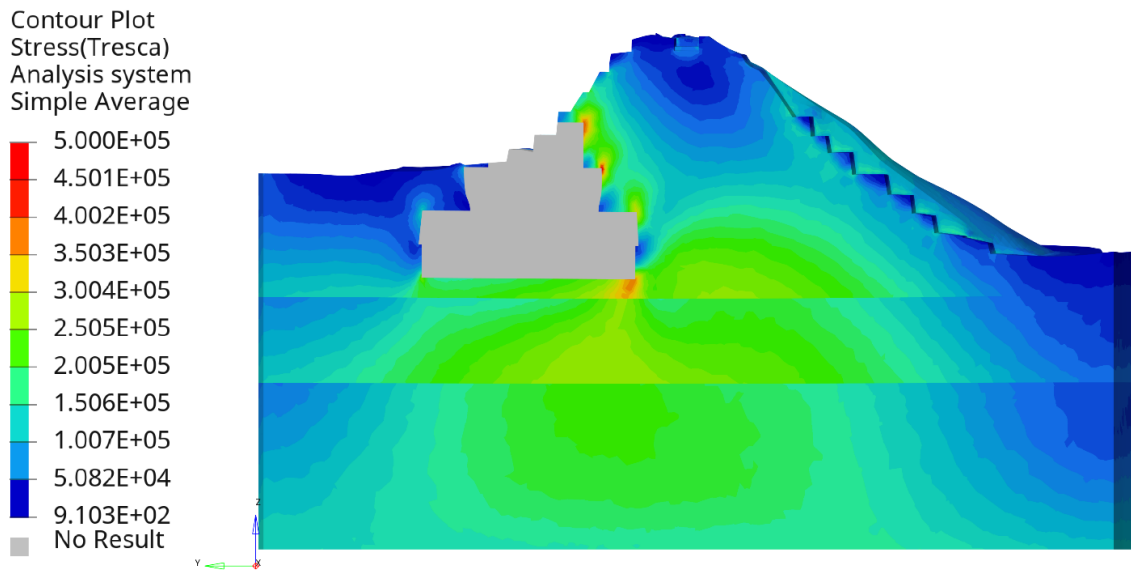


Figure 5.23. Cross-sectional cut at YZ plane of configuration B stress results at midspan (90% saturation level).

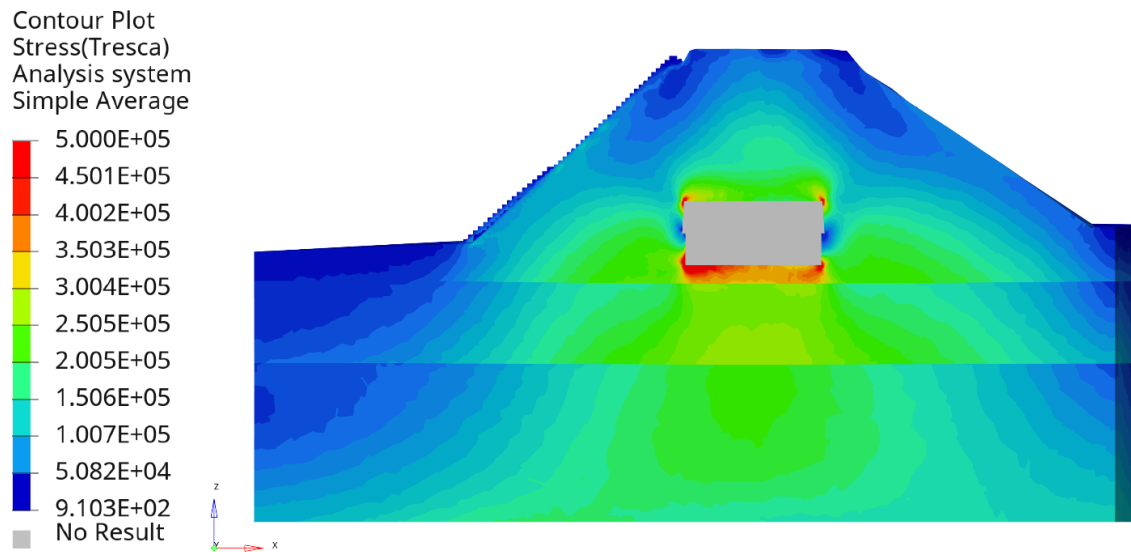


Figure 5.24. Cross-sectional cut at XZ plane of configuration B stress results showing Rosalila's southern profile (90% saturation level).

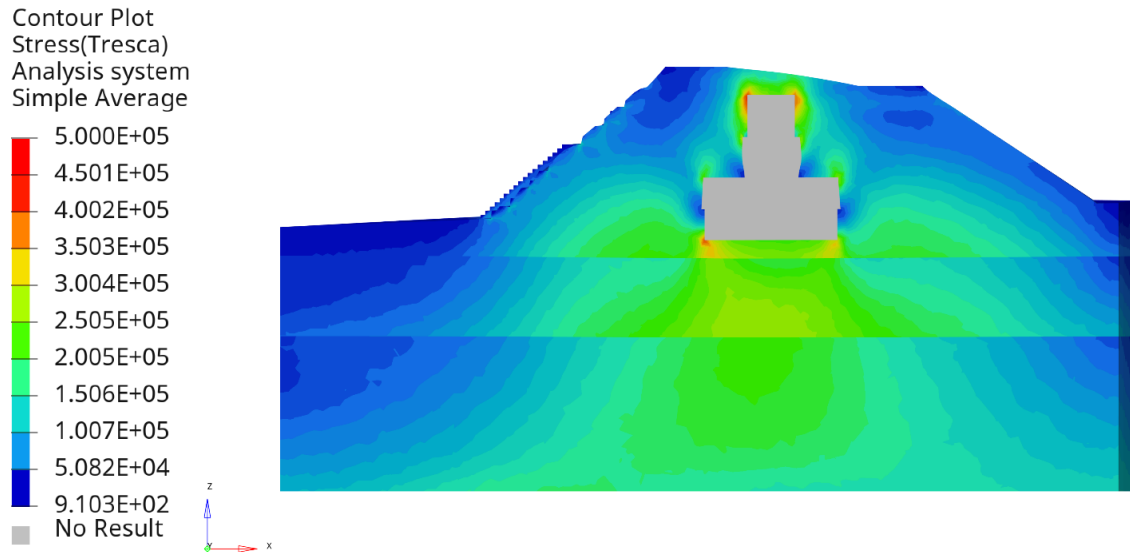


Figure 5.25. Cross-sectional cut at XZ plane of configuration B stress results showing Rosalila's southern profile (90% saturation level).

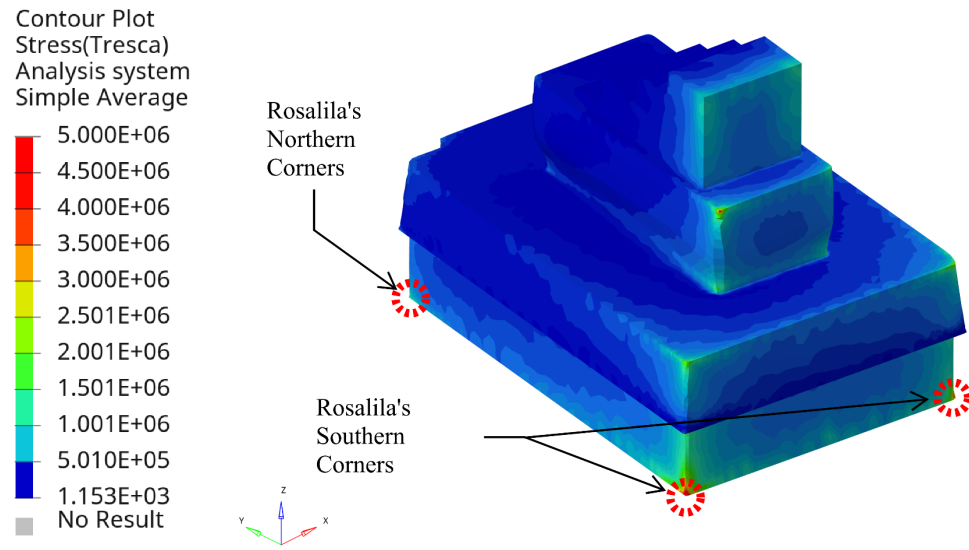


Figure 5.26. View from the southwest of configuration B stress results of Rosalila (90% saturation level).

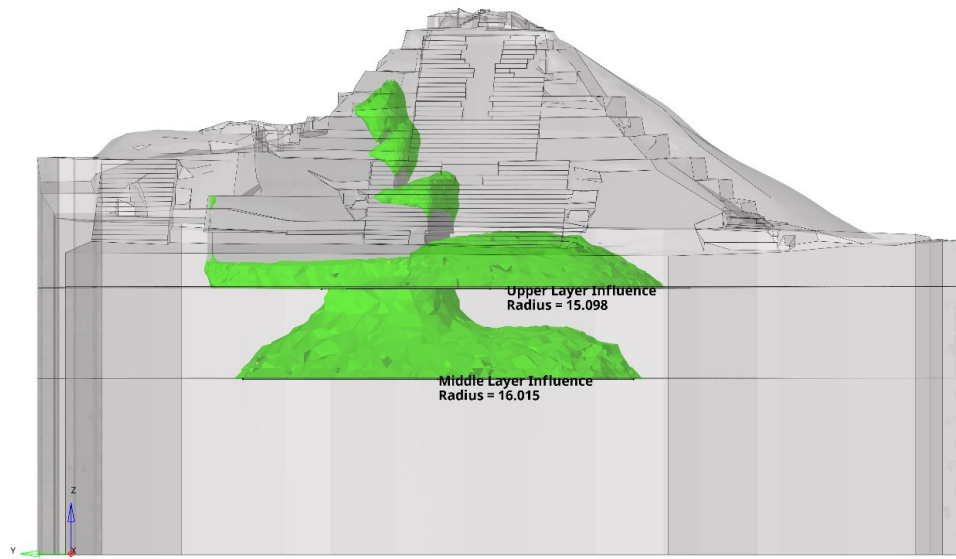


Figure 5.27. View from west of isosurface showing areas influenced by Rosalila's loading for configuration B stress results (90% saturation level).

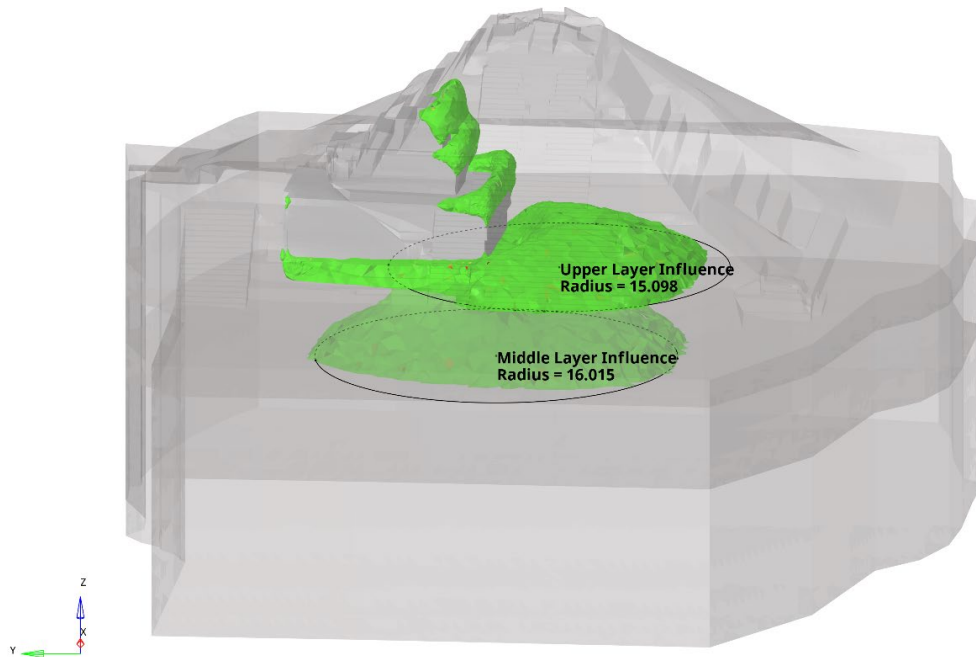


Figure 5.28. Tilt-up view from west of isosurface showing areas influenced by Rosalila's loading for configuration B stress results (90% saturation level).

### 5.3.2 Temple 16 Tunnels

#### 5.3.2.1 Current State of Tunnels

Figure 5.29 and Figure 5.30 show transparent views of the stress distribution of Temple 16 and Rosalila when the current tunnel geometry is included (configuration A). From these contour plots, it can be observed that the tunnels surrounding and just below Rosalila exhibit the highest levels of stress (i.e., red areas in the plot). The regions with high stress levels become more apparent in the isosurfaces shown in Figure 5.31 and Figure 5.32. These isosurfaces isolate stress regions higher than the median Tresca stress value for this model (i.e., the median value of the contour plot scale in Figure 5.29 and Figure 5.30). This median value is selected to isolate the stress concentrations observed along the entire tunnel system. The locations of highly stressed areas on the upper levels of Temple 16 match the general stress field that was observed in configuration B (geometry with no tunnels included, Figure 5.27 & Figure 5.28), with the highest stress concentration at tunnels nearby the southern corners of Rosalila and Rosalila's upper levels on its southern side (Figure 5.33). Figure 5.33 also shows high stress in tunnels that are near to the buried Oropéndola structure and that fall within Rosalila's region of influence, as defined in Section 5.3.1. This claim is further shown in Figure 5.34 where the upper layer influence radius observed in Figure 5.27 is overlaid on the isosurface. Finally, typical tunnel sections that exhibit high levels of stress correspond to areas with sharp geometric features, such as tunnel junctions (Figure 5.35), or sharp turns in tunnel orientation, such as re-entrant corners (Figure 5.36). These sections are expected to show high stress levels as these regions have high stiffness due to their geometry and the way

their geometries influence the stress field at a local level according to St. Venant's principle. Figure 5.35 and Figure 5.36 are representative only, and other tunnel sections with sharp geometric features or turns in tunnel orientation have similarly high stresses.

Figure 5.31 and Figure 5.32 also show that lower-level tunnels are typically exposed to higher stress levels compared to those at higher levels. This is partially due to the lower elevations of the tunnels, which require them to support more weight from the upper areas of Temple 16. Figure 5.37 and Figure 5.38 show the stress concentrations on lower-level tunnels only (with the upper infill layer hidden for clarity) after generating a new isosurface that shows stress equal or higher than 95% of the maximum reported Tresca stress value in this model. From these figures, lower-level tunnels that are directly below Rosalila are typically with the highest levels of stress concentrations in this region.

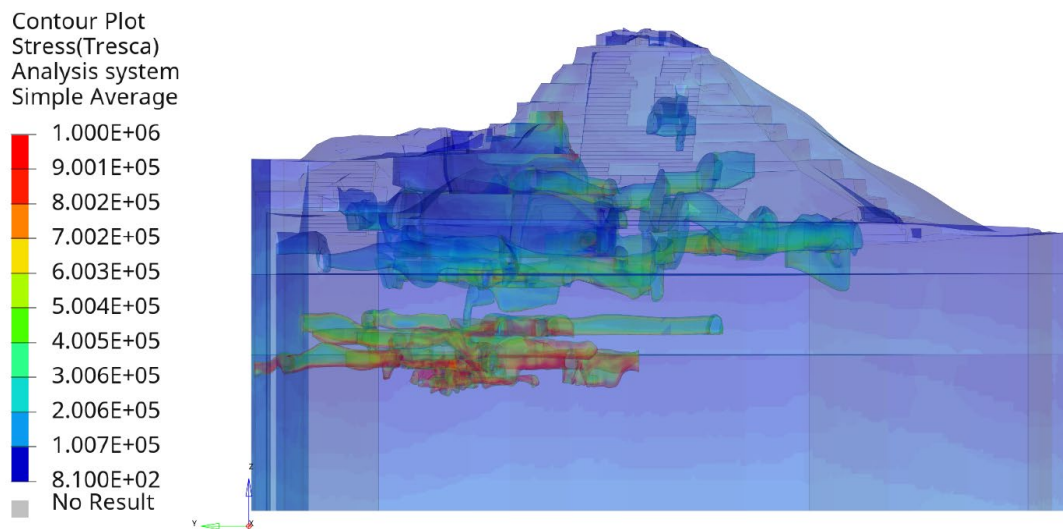


Figure 5.29. Transparent view from the west showing tunnel stress results for configuration A (90% saturation level).

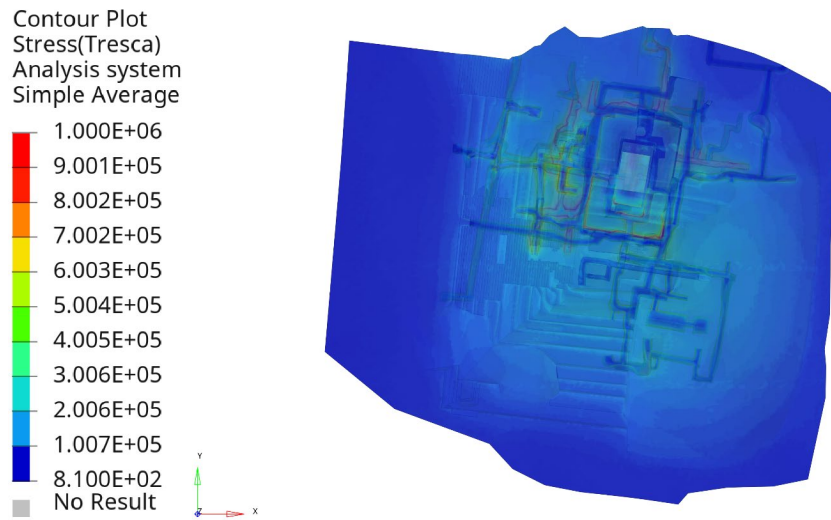


Figure 5.30. Transparent plan view showing tunnel stress results for configuration A (90% saturation level).

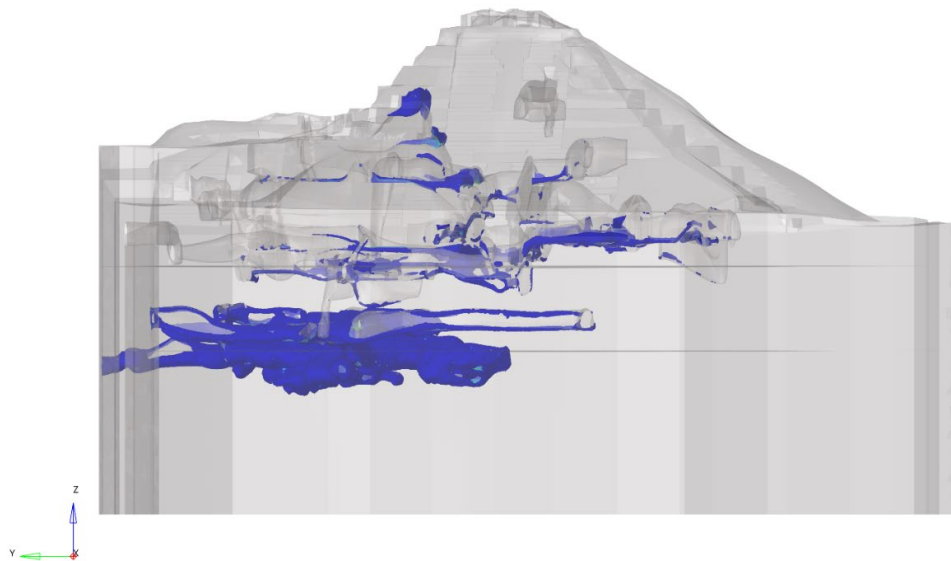


Figure 5.31. Front view of isosurface showing areas with stress levels higher than the median Tresca stress around tunnels for configuration A.

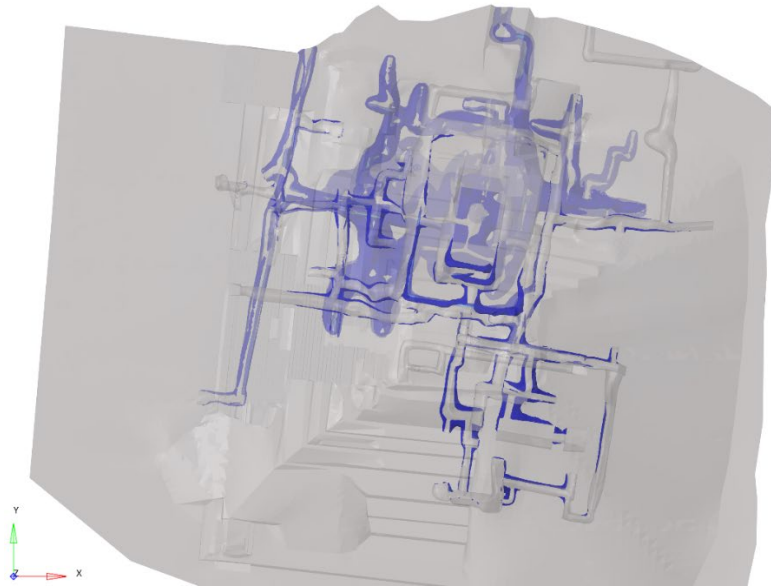


Figure 5.32. Plan view of isosurface showing areas with stress levels higher than the median Tresca stress around tunnels for configuration A.

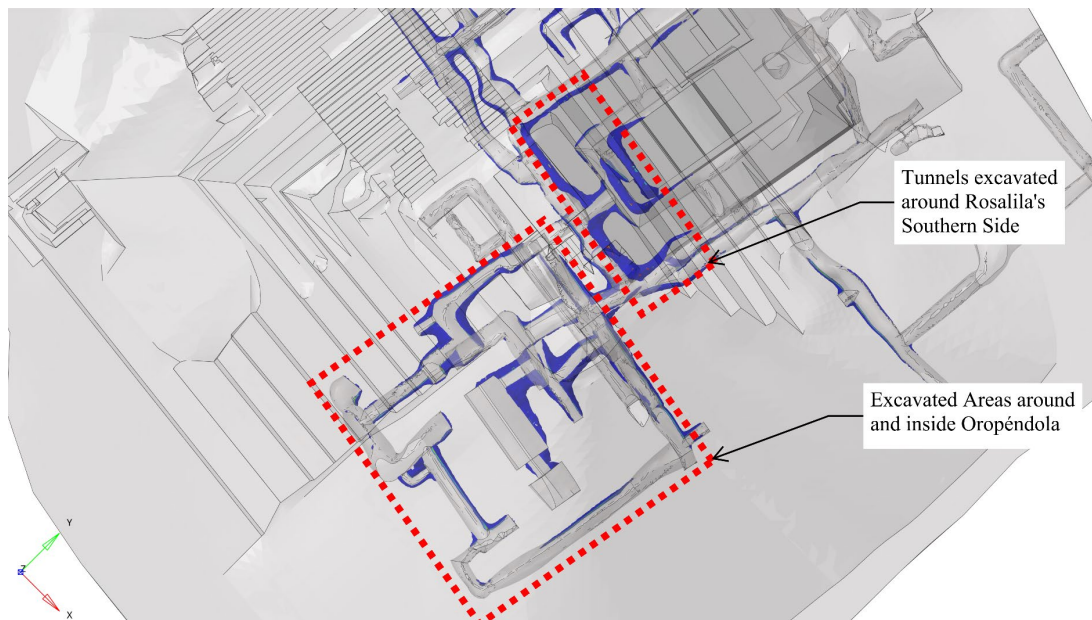


Figure 5.33. Plan view of isosurface showing areas with stress levels higher than the median Tresca stress around tunnels surrounding southern side of Rosalila and tunnels around Oropéndola for configuration A.



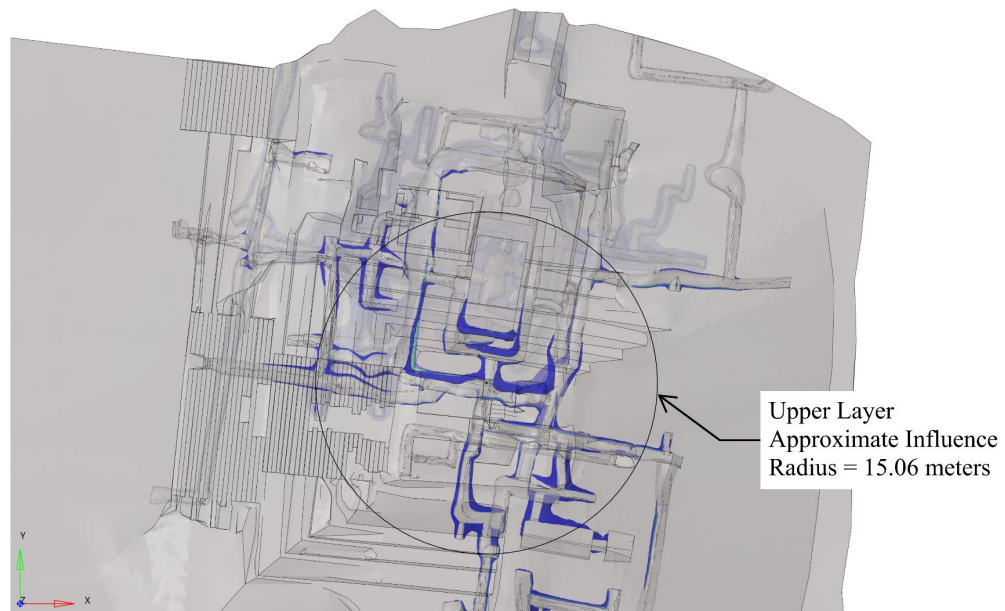


Figure 5.34. Plan View of isosurface showing areas showing approximated radius of areas influenced by Rosalila for configuration A stress results.

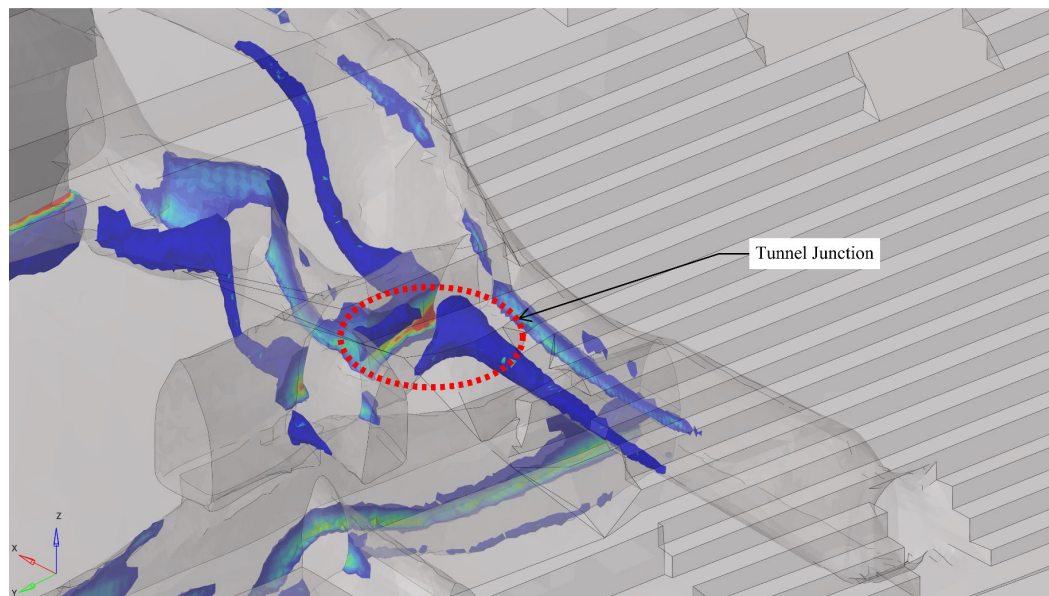


Figure 5.35. Close-up view of isosurface showing areas with stress levels higher than the median Tresca stress around a tunnel junction near west entrance.



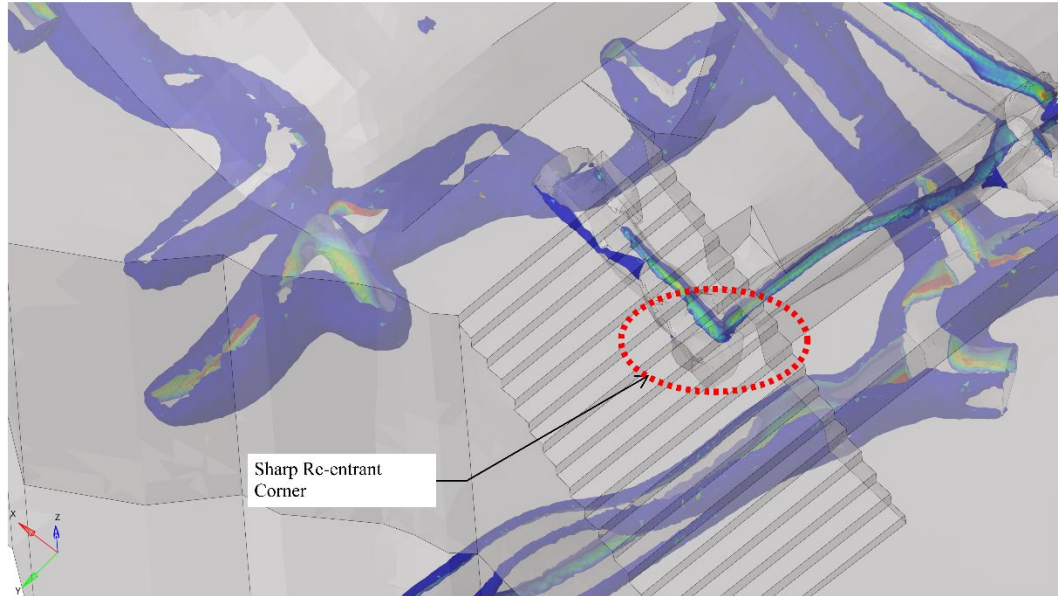


Figure 5.36. Close-up view of isosurface showing areas with stress levels higher than the median Tresca stress around a tunnel sharp corner.

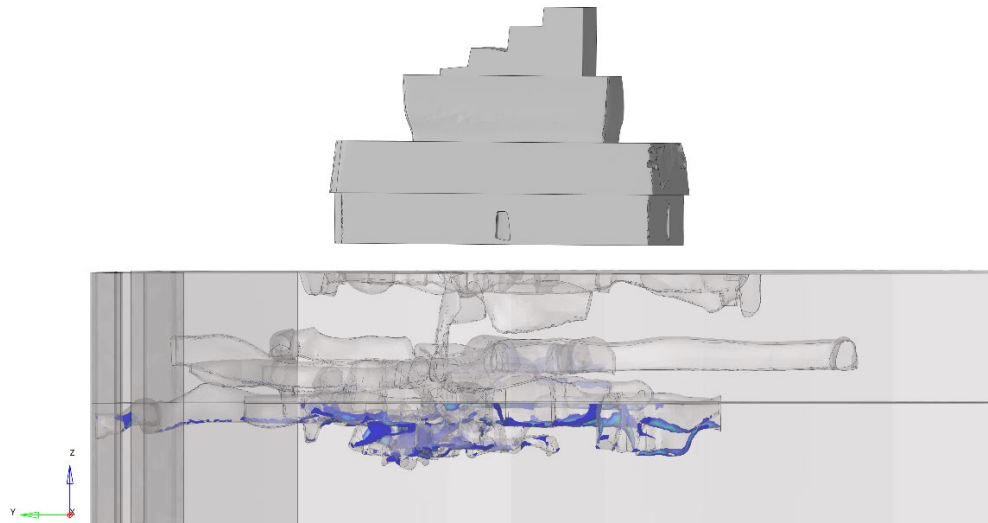


Figure 5.37. Front view of isosurface showing areas with stress levels higher than the median Tresca stress around lower-level tunnels for configuration A (upper infill layer hidden for clarity).



Figure 5.38. Plan view of isosurface showing areas with stress levels higher than the median Tresca stress around lower-level tunnels for configuration A (upper infill layer hidden for clarity).

#### 5.3.2.2 Overview of Stress Changes for Other Scenarios

Results obtained from Configuration A (geometry with all current tunnels) were compared with the ones obtained for Configurations C (geometry with upper-level tunnels only), D (geometry with lower-level tunnels only), and E (geometry with Rosalila's center room backfilled). For this, 63 stress concentration areas were identified from Configuration A at the critical areas discussed in Section 5.3.2.1 Current State of Tunnels. Stress values at these locations were also recorded for the other configurations, and they were respectively compared with the values observed in Configuration A to obtain a comparison percentage change under the following relationship:

$$\text{Change in Stress} = \frac{\text{Stress at Configuration X} - \text{Stress at Configuration A}}{\text{Stress at Configuration A}} \cdot 100\%$$

From this relationship, a positive change in stress corresponds to a stress increase of a hypothetical configuration “X” with respect to the general configuration case (Configuration A) for the same location in both models. Similarly, a negative change in stress corresponds to a stress decrease with respect to Configuration A for a common stress concentration area. A summary of these comparisons can be found in Table 5.3, Table 5.4 and Table 5.5 for 90%, 70% and 50% Saturation Levels, respectively. The summary tables indicate the maximum change in stress at a stress concentration, the minimum change in stress at a stress concentration, and the average change in stress considering all 63 stress concentrations. A more detailed report that lists the geospatial locations and a brief description of the selected areas, including commonly used tunnel names and descriptions, can be found in Table B.1 to Table B.8 of Appendix B.

Table 5.3. Stress changes at identified locations at 90% saturation level.

<i>Results Comparison at 90 % Saturation</i>					
Comparison Case	Configuration Selected for Comparison	Reference Configuration	Max. Stress Change (%)	Min.Stress Change (%)	Average Stress Change (%)
Config. A vs C	C	A			
	"Only Tunnels Above 598 meters of Elevation"	"General As-Is Case"	15.79%	-39.23%	-5.50%
Config. A vs D	D	A			
	"Only Tunnels Below 598 meters of Elevation"	"General As-Is Case"	27.71%	-11.09%	6.19%
Config. A vs E	F	A			
	"Rosalila's Center Room Backfilled"	"General As-Is Case"	10.84%	-4.05%	1.06%

Table 5.4. Summary of results comparison at 70% saturation level.

<b>Results Comparison 70 % Saturation</b>					
Comparison Case	Configuration Selected for Comparison	Reference Configuration	Max. Stress Change (%)	Min. Stress Change (%)	Average Stress Change (%)
Config. A vs C	C "Only Tunnels Above 598 meters of Elevation"	A "General As-Is Case"	15.81%	-39.31%	-5.47%
Config. A vs D	D "Only Tunnels Below 598 meters of Elevation"	A "General As-Is Case"	27.82%	-10.91%	6.20%
Config. A vs E	F "Rosalila's Center Room Backfilled"	A "General As-Is Case"	10.75%	-3.98%	1.11%

Table 5.5. Summary of results comparison at 50% saturation level.

<b>Results Comparison 50 % Saturation</b>					
Comparison Case	Configuration Selected for Comparison	Reference Configuration	Max. Stress Change (%)	Min. Stress Change (%)	Average Stress Change (%)
Config. A vs C	C "Only Tunnels Above 598 meters of Elevation"	A "General As-Is Case"	15.82%	-39.41%	-5.43%
Config. A vs D	D "Only Tunnels Below 598 meters of Elevation"	A "General As-Is Case"	27.93%	-10.74%	6.19%
Config. A vs E	F "Rosalila's Center Room Backfilled"	A "General As-Is Case"	10.66%	-3.92%	1.13%

### 5.3.2.3 Impact on Upper-Level Tunnels

Figure 5.39 and Figure 5.40 show isosurfaces generated from the configuration case where lower-level tunnels are not included in the model (Configuration C). These isosurfaces were generated by isolating stresses that were equal or higher than the median Tresca stress reported for the general configuration case (Configuration A, refer to

Section 5.3.2.1). Figure 5.41 and Figure 5.42 compare these generated isosurfaces with those generated for Configuration A (general case), in which it is observed that completely filling one tunnel level while the other remains open does not significantly change the areas where stress concentrations are present in the current state of the tunnels. In order to provide a reference for visual comparison between both configurations, Figure 5.41 the generated isosurfaces for both configurations when viewing from the west. Similarly, Figure 5.42 shows a close-up plan view of the generated isosurfaces on a portion of the tunnels, which happen to be in the vicinity of Oropéndola. From these figures, the areas with high stress concentrations for both configurations are nearly identical for the upper-level tunnels when viewing both configuration models from the west (Figure 5.41) and in plan view (Figure 5.42).

The absence of lower-level tunnels in Configuration C causes stress concentrations to increase or decrease depending on their location within the model. Upper-level tunnels that are close in elevation to lower-level tunnels experience an overall decrease in the observed peak stress when a complete shutdown of lower-level tunnels is considered (Configuration C). From the first rows of Table 5.3 to Table 5.5, this geometric change causes a drop in peak stress up to 40% for upper-level tunnel sections that are partially below the 598 meters elevation limit (see representative stresses shown in Figure 5.43). This is not necessarily the case for tunnels surrounding Rosalila's southern corners, where there is an overall increase in peak stress since more underlying infill mass is pushing against the structure. This effect causes a stress increase of up to

16% at Rosalila's southern corners (first rows of Table 5.3 to Table 5.5). These corners are highlighted in Figure 5.44.

Finally, when averaging the stress changes recorded from comparing Configuration C with Configuration A, it is possible to approximate the overall influence of lower-level tunnels into the upper-level ones. The first rows of Table 5.3 to Table 5.5 indicate that the lower-level tunnel has an overall influence of -5.5% in the stress level experienced on the upper-level tunnels. This value indicates that removing or backfilling lower-level tunnels while keeping the upper-level ones causes an average stress decrease of 5.5% on the remaining tunnels. This value is approximately constant for all tested saturation levels, with an overall decrease of 0.03% to 0.04% drop on average stress for a 20% drop in water saturation level.

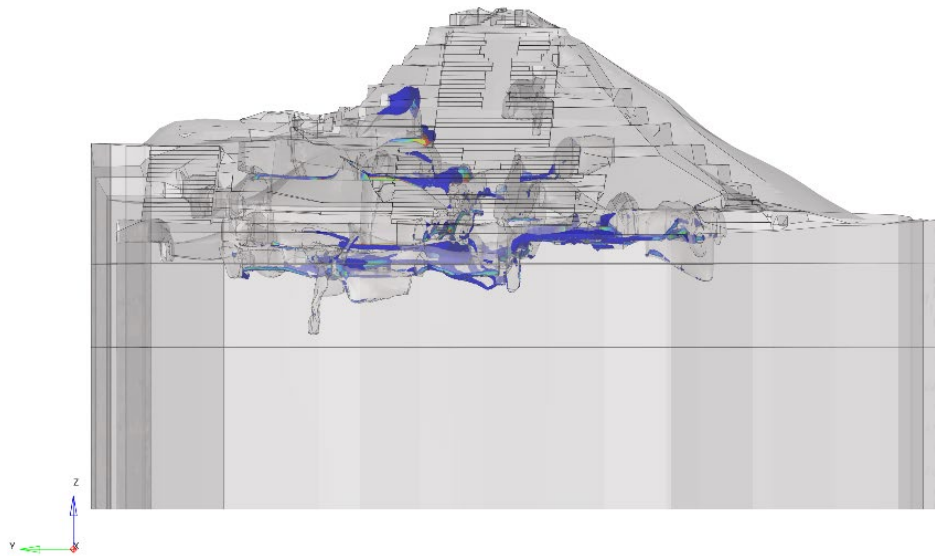


Figure 5.39. Front view of isosurface showing areas with stress levels higher than the median Tresca stress around upper-level tunnels for configuration C.

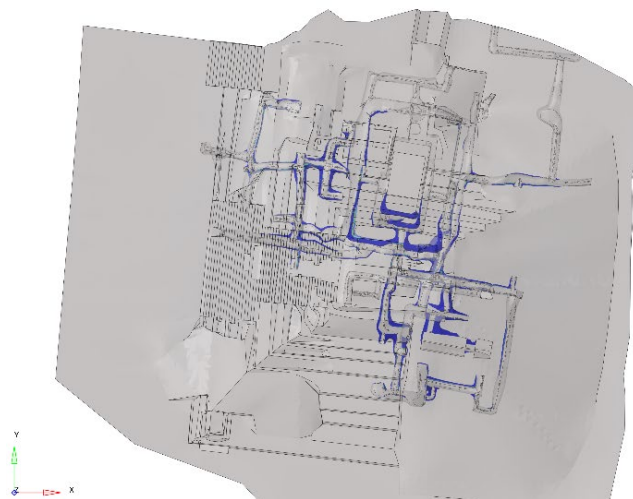


Figure 5.40. Plan view of isosurface showing areas with stress levels higher than the median Tresca stress around upper-level tunnels for configuration C.

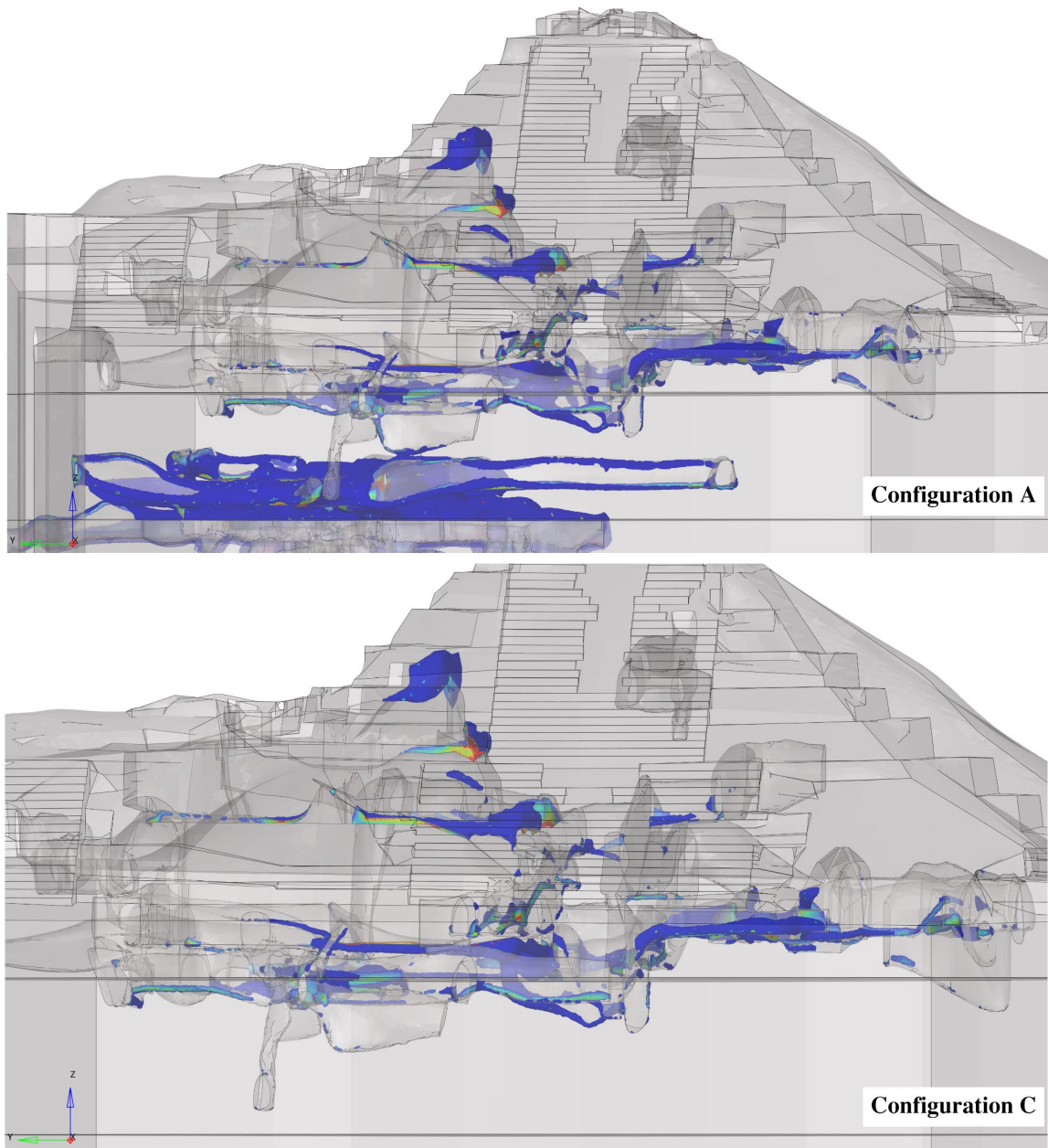


Figure 5.41. Comparison of areas with stress levels greater than the median Tresca stress at upper-level tunnels between configuration A (all tunnels included) and configuration C (upper-level tunnels only) (view from the west).



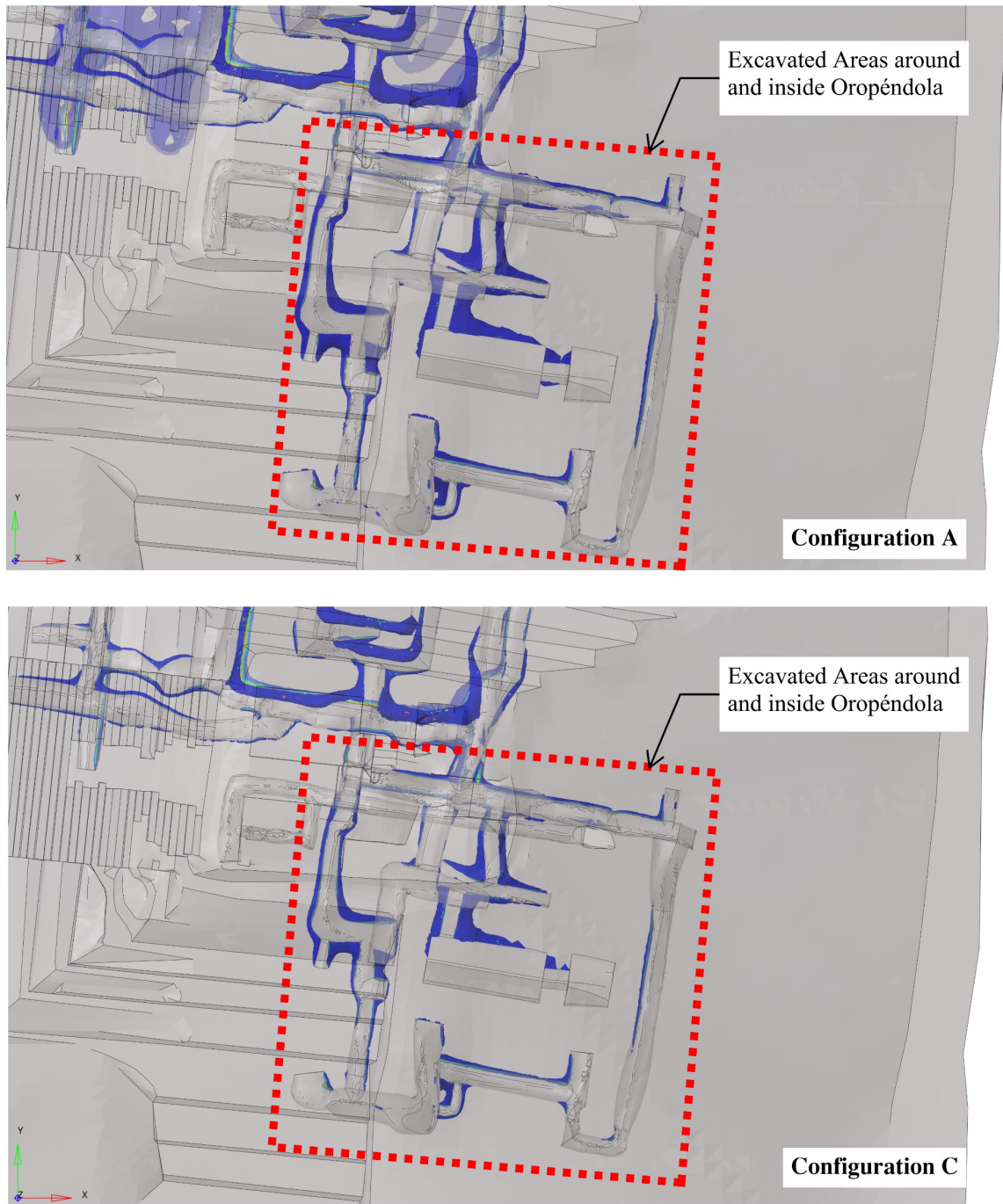


Figure 5.42. Comparison of areas with stress levels greater than the median Tresca stress between configuration A (all tunnels included) and configuration C (upper-level tunnels only) (plan view).

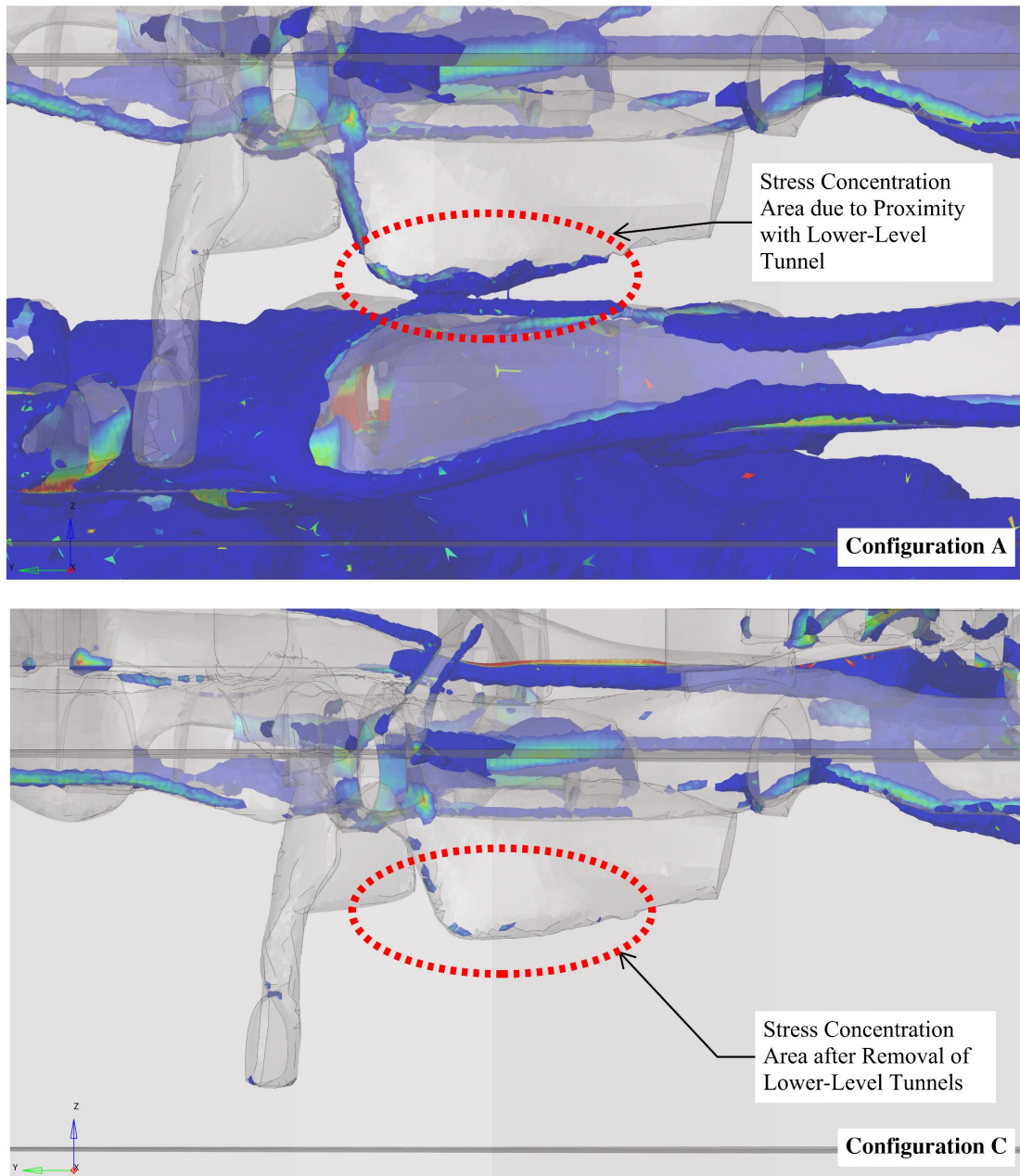


Figure 5.43. Comparison of area with stress levels greater than the median Tresca stress of upper-level tunnel section that is close to lower-level tunnels in configuration A (all tunnels included) with configuration C (upper-level tunnels only) (view from west).

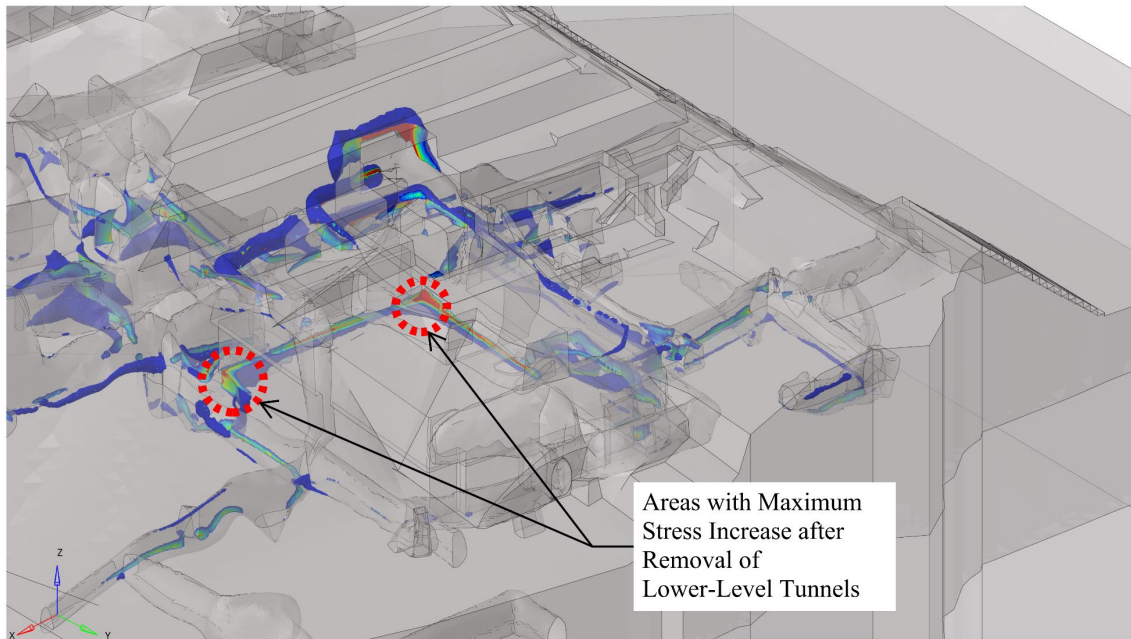


Figure 5.44. View from the northeast of rosallila surrounding areas with stress levels greater than the median Tresca stress for configuration C (upper-level tunnels only ).

#### 5.3.2.4 Impact on Lower-Level Tunnels

Figure 5.45 and Figure 5.46 show the isosurfaces generated for the configuration case where upper-level tunnels have been disregarded from the geometry (Configuration D). These isosurfaces were generated by isolating stress concentrations that were equal or higher than 95% of the highest Tresca stress value for the general configuration case (Configuration A, refer to Section 5.3.2.1). When comparing this configuration with the general case (Configuration A), it is observed that the stress concentrations remain largely unchanged, as Figure 5.47 shows. When upper-level tunnels are filled, there is an average stress increase observed in the lower-level tunnels, as shown in the second row of Table 5.3 to Table 5.5. This average stress increase is about 6.20% for all tested saturations levels since the lower infill layer was assumed to be completely saturated for

all cases. Tunnels that lie directly below Rosalila experience the highest levels of stress increase. Considering the absence of upper-level tunnels, tunnels of Configuration D that are directly below Rosalila experience a stress increase as high as 28% with respect to their current state (Configuration A) (second rows of Table 5.3 to Table 5.5). These areas are highlighted in Figure 5.48 . A more detailed numerical comparison between stress concentrations between configurations A and D can be found on Table B.3 to Table B.8 of Appendix B. This stress increase between configurations is due to the added mass that is now covering the upper-level tunnels. Some minor tunnel sections experience decreased stress due to the change in geometry and stress flow. These sections are commonly outside the influence radius and are closer to the 598 meters elevation limit. Finally, a similar trend can be observed when Rosalila's Center Room is filled (Configuration F). The third rows of Table 5.3 and Table 5.5 show that the stress increase for the lower-level tunnel section that lies directly underneath Rosalila experiences a stress increase of up to 10.8% at the same locations identified for Configuration D. However, the effects of Rosalila's center room's added mass to the lower-level tunnels drastically decrease for lower-tunnel sections that are away from Rosalila's bearing area. This causes the average stress increase to be of about 1.10% when comparing this configuration with the general case (Configuration A) for the lower-level tunnels (third rows of Table 5.3 to Table 5.5).

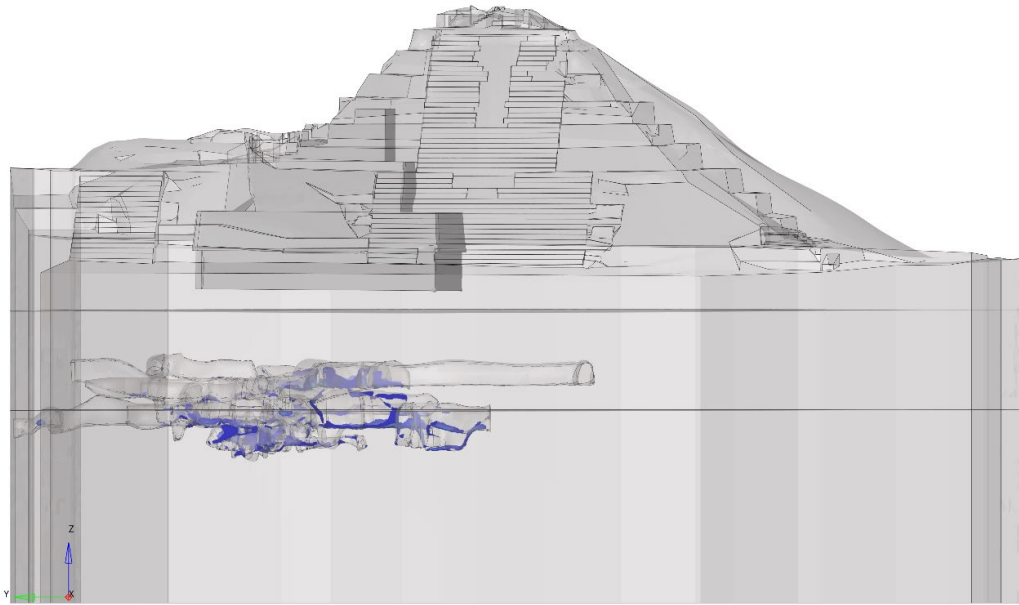


Figure 5.45. View from the west of isosurface showing areas with stress levels higher than 95% of maximum Tresca stress around upper-level tunnels for configuration D.



Figure 5.46. Plan view of isosurface showing areas with stress levels higher than 95% of maximum Tresca stress around upper-level tunnels for configuration D.





Figure 5.47. Comparison of areas with stress levels higher than 95% of maximum Tresca stress at lower-level tunnels between configuration A (all tunnels included) and configuration D (lower-level tunnels only) (plan view).

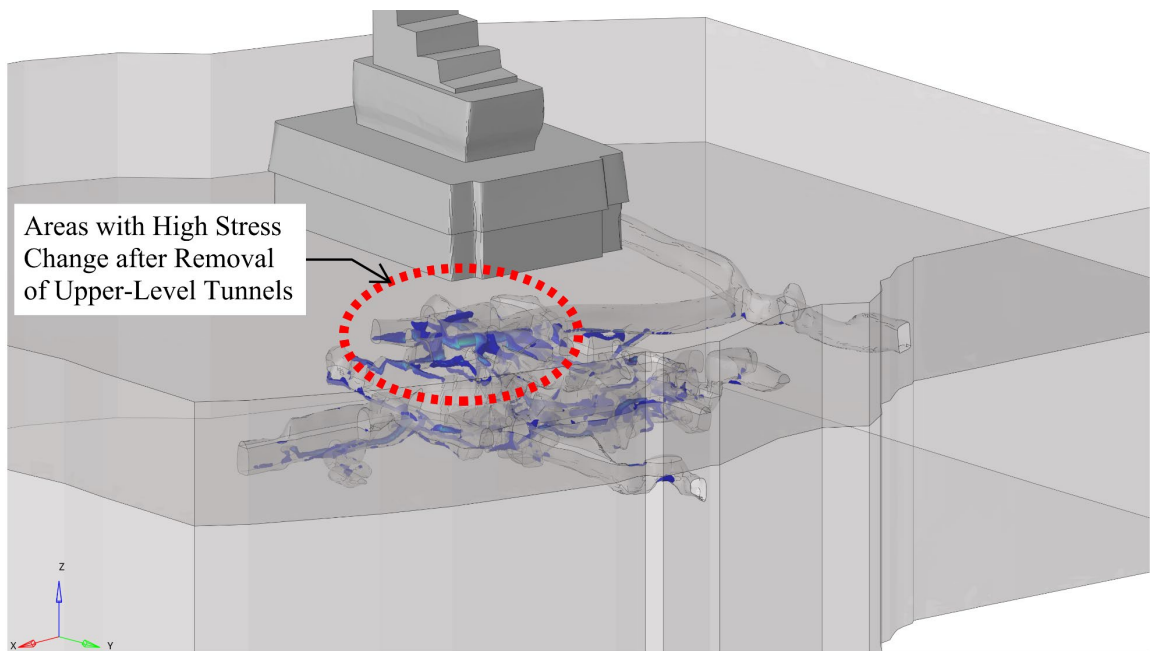


Figure 5.48. View from northeast of areas with stress levels higher than 95% of maximum Tresca stress at tunnels underneath rosalia configuration D (lower-level tunnels only).

### 5.3.3 Rosalila

#### 5.3.3.1 Current State of Rosalila

The stress distribution observed within Rosalila yields similar conclusions to those drawn from the overall Temple 16 and tunnel system. Figure 5.49 and Figure 5.50 show the stress results of the exterior of Rosalila when the current tunnel system is accounted for in the geometry (Configuration A). The southern side of the structure is exposed to higher stress levels that tend to concentrate at the corners of this side of the structure. As it was discussed previously for the configuration where no tunnels are accounted for in the geometry (Configuration B, Section 5.3.1), these stress concentrations occur in this area since it is closer to the Temple 16's centroidal axis. This pre-established stress path is conserved once tunnels are added and seem to play a major role when tunnels are excavated around this area of the structure. This is shown in Figure 5.51 and Figure 5.52 when comparing Configuration A results with Configuration B. From these figures, it is observed that both Rosalila configurations show high stress levels on the southern side of the structure. However, there is a stress change around the excavated areas of the structure. From Figure 5.51 and Figure 5.52, the excavated walls experience stress increase when they are used as support for the excavated tunnel areas. This is shown in the circled areas for Configuration A where the contour plot shows brighter areas (i.e., higher stress levels) around exposed wall sections of Rosalila. As Rosalila is built with a stiffer material with respect to its surrounding infill, most of the load that is affecting the surrounding tunnels is supported by Rosalila's excavated areas.



The resulting stress spreads radially outwards with relation to the tunnel cross-section, causing the surrounding unexcavated areas to also experience a stress increase.

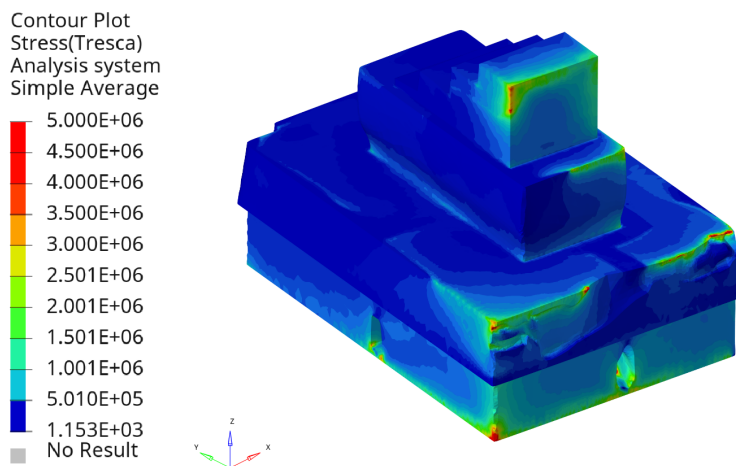


Figure 5.49. View from the southwest of Rosalila stress results for configuration A (90% saturation level).

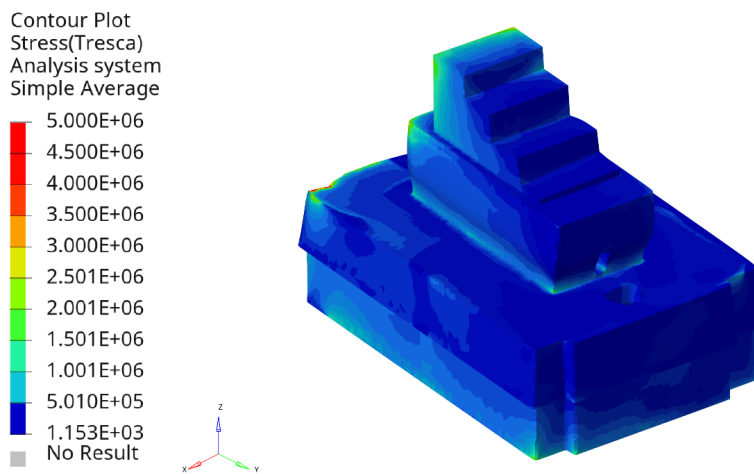


Figure 5.50. View from the northeast of Rosalila stress results for configuration A (90% saturation level).

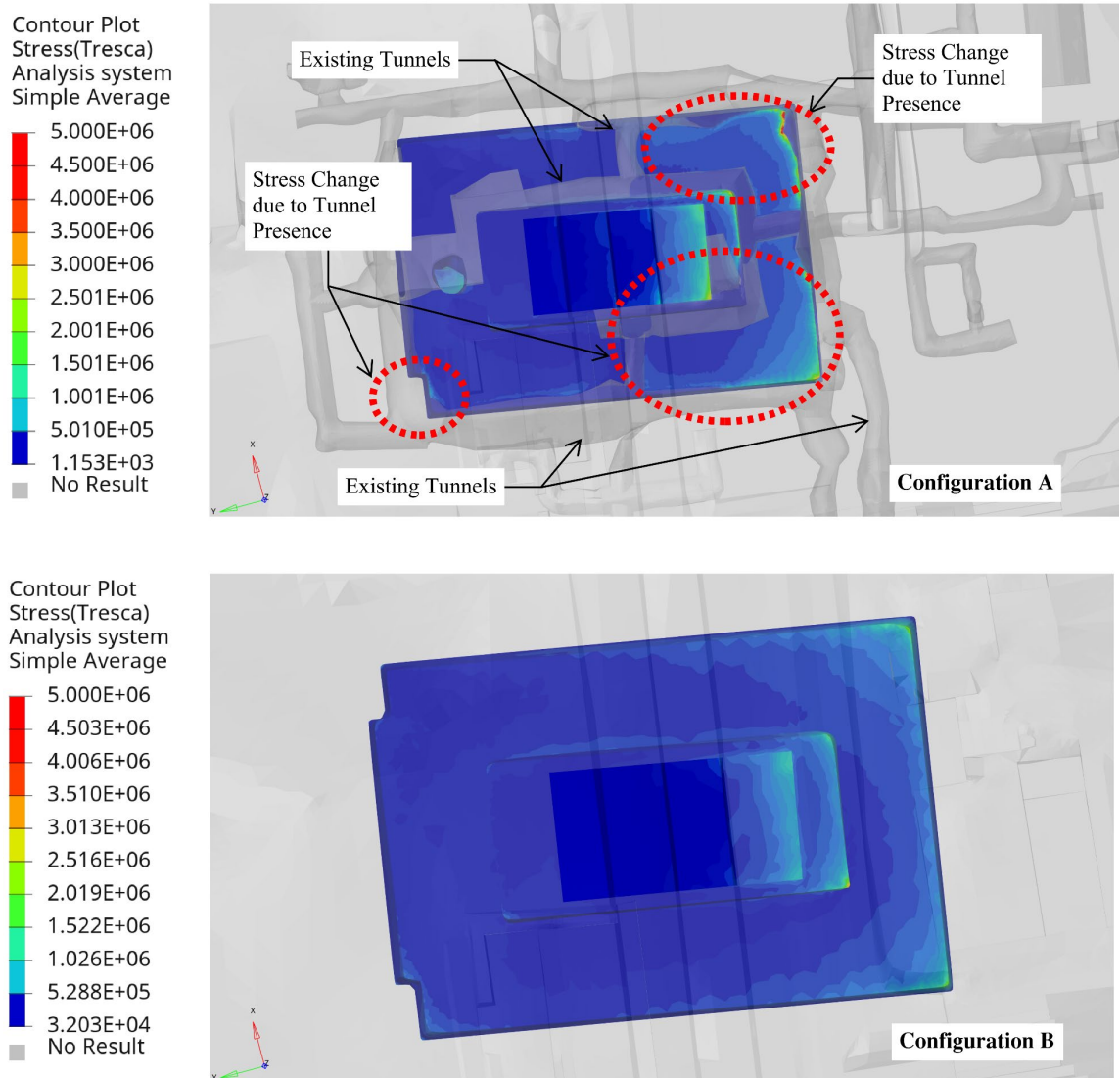


Figure 5.51. Comparison of stress concentrations level at areas surrounding Rosalila between configuration A (all tunnels included) and configuration B (no tunnels included) (plan view).

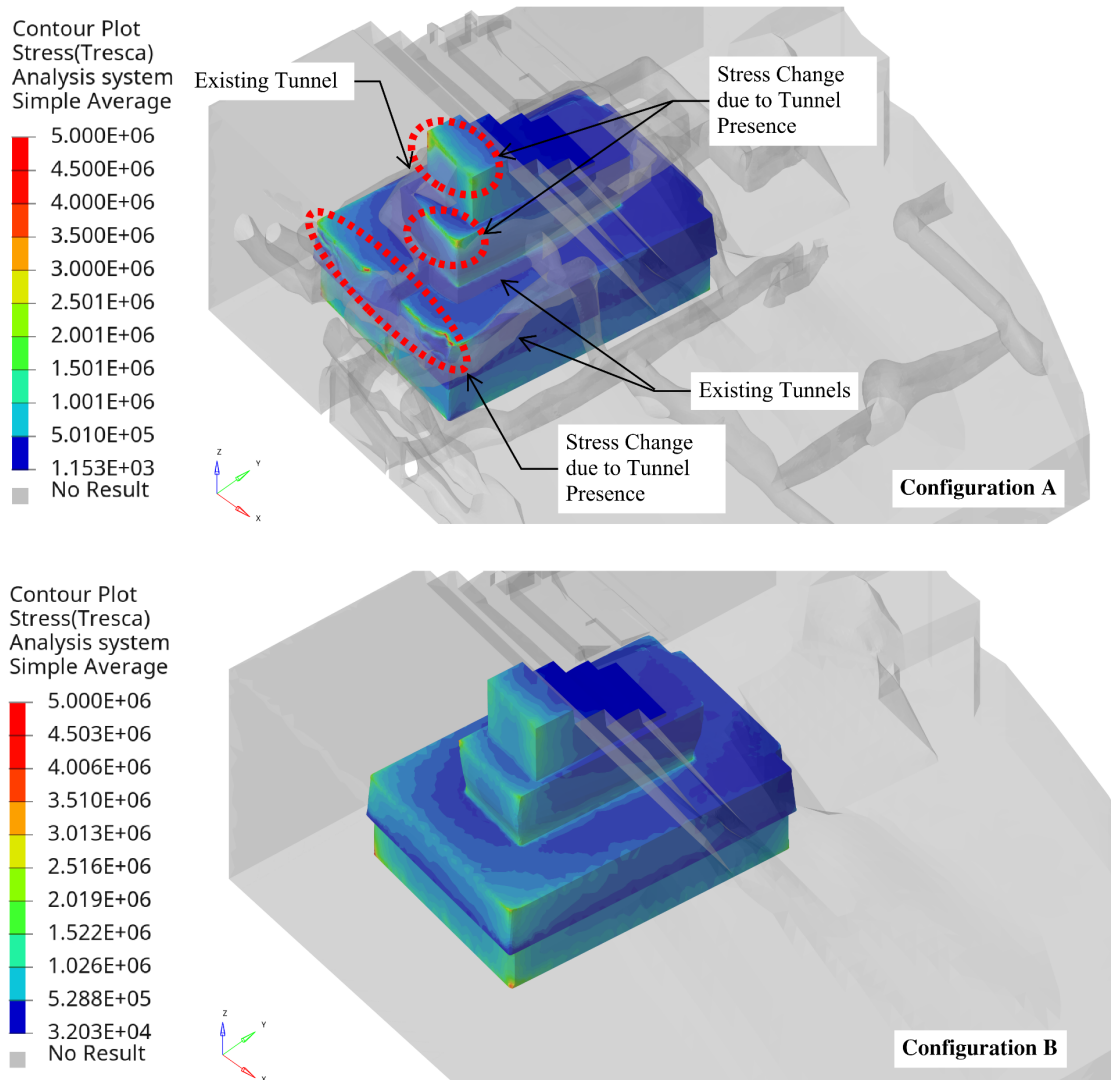


Figure 5.52. Comparison of stress concentrations level at areas surrounding Rosalila between configuration A (all tunnels included) and configuration B (no tunnels included) (view from the southeast).

### 5.3.3.2 Backfilling of Rosalila's Center Room

The excavated rooms within Rosalila show higher stresses on the southern side of the structure compared to the northern half (Figure 5.53 and Figure 5.54). As it was discussed in previous sections, Configuration A (current tunnel system) results show high-stress concentrations at the base of tunnel sections that connect to the southern and western entrances to the structure, which can be seen in Figure 5.53 and Figure 5.54. The location of these stress concentrations suggests that they are also a result of proximity to the structure's base. As expected, cross-sections taken on the northern side of the structure show lower stress concentrations due to their location within the model and their higher distance from the base, as shown in Figure 5.55 and Figure 5.56. The stress concentrations at the base of the center room increase from north to south as the base of these excavated areas get closer to the base of the structure (Figure 5.55 and Figure 5.56). These stress concentrations are local, and their close proximity to the structure's base significantly limits the impact to other areas of the structure. This is the case observed for configuration E, in which the model was analyzed considering the center room of Rosalila to be filled. Figure 5.57 and Figure 5.58 compare the resulting stress fields when Rosalila's center room is open (Configuration A) and when it is filled (Configuration E). As shown, the stress concentrations in the center room itself are reduced when the room is filled, but the high-stress levels in the southern areas of Rosalila are not appreciably changed. The filling of the center room improves the stress flow on the northern side of the structure, which allows a better stress re-distribution on the northern side of the structure only.

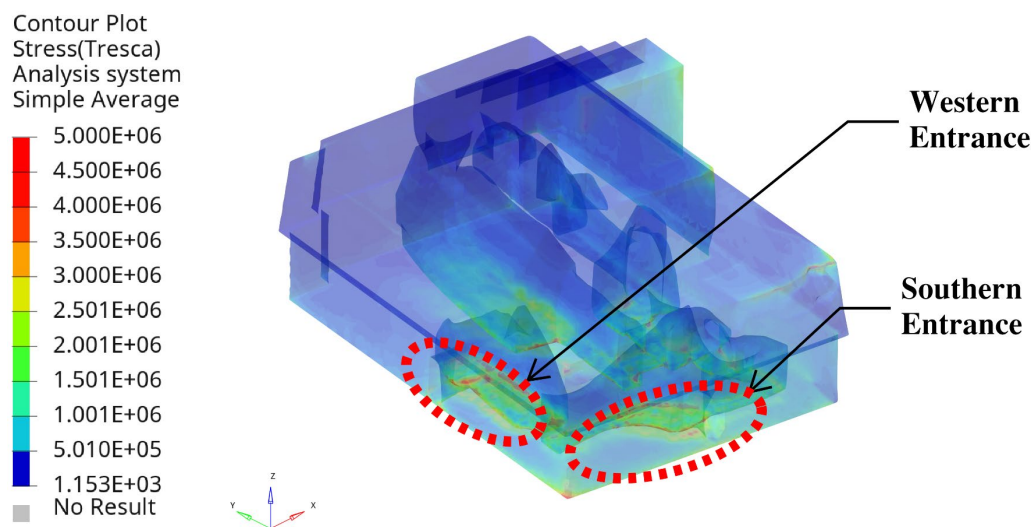


Figure 5.53. Transparent view from the southwest of Rosalila stress results for configuration A (90% saturation level).

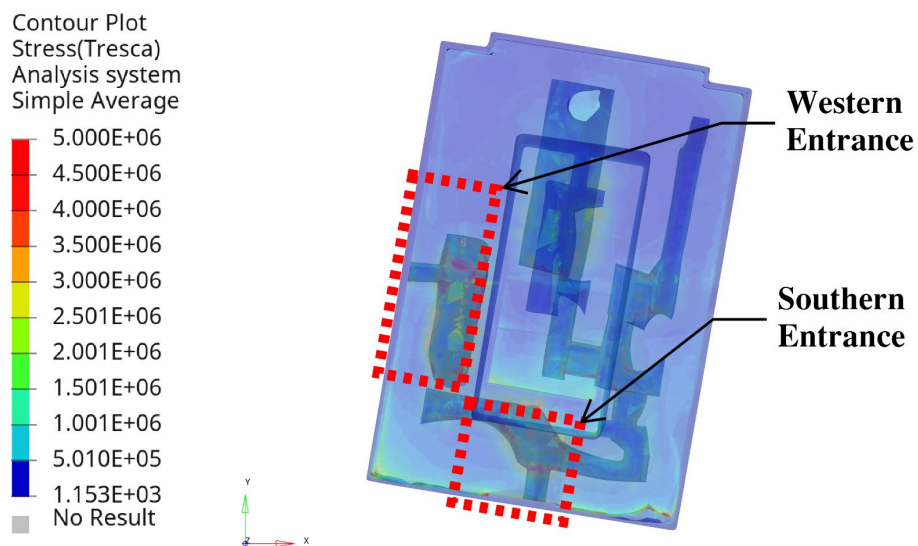


Figure 5.54. Transparent plan view of Rosalila stress results for configuration A (90% saturation level).

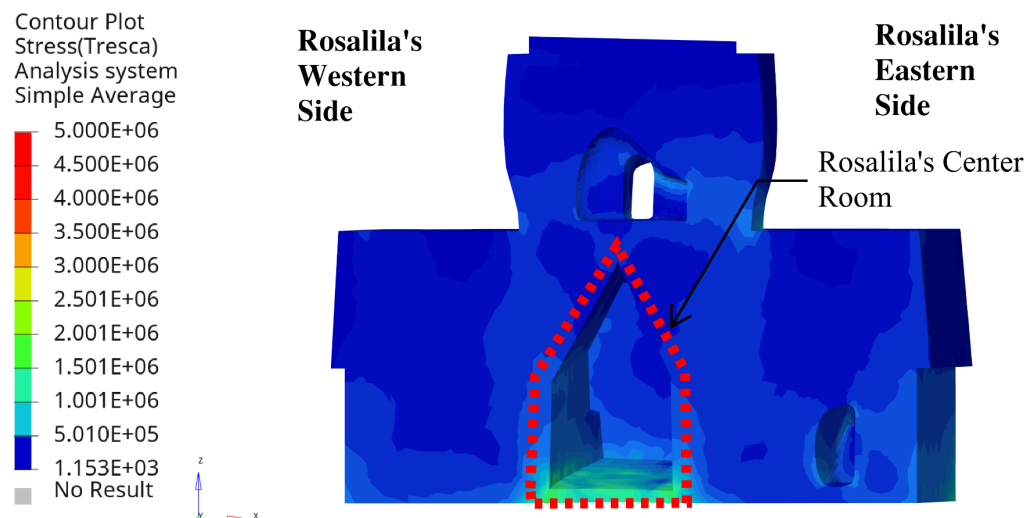


Figure 5.55. View from the south of cross-sectional cut of configuration A Rosalila stress results at Rosalila's center room midspan (90% saturation level).

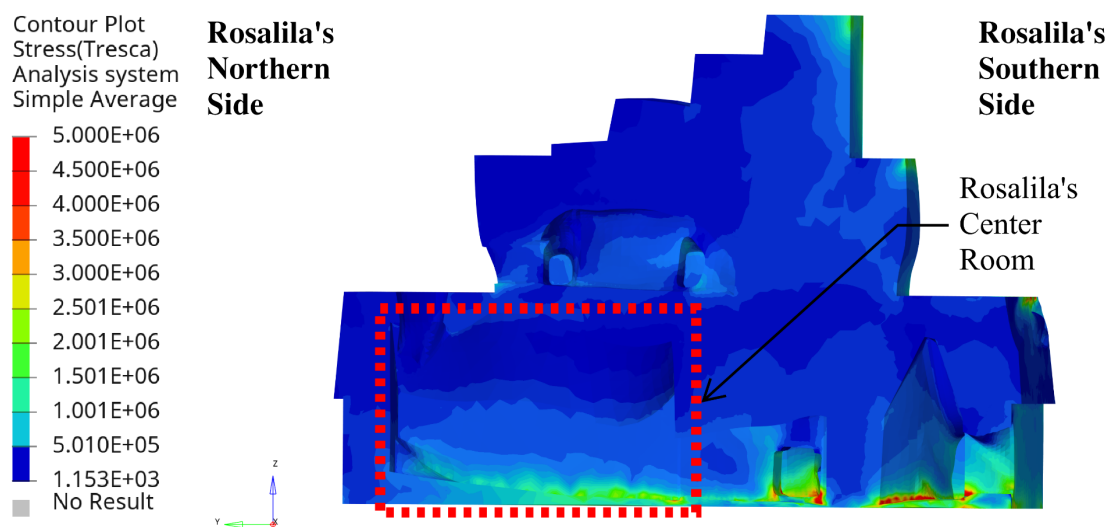


Figure 5.56. View from the west of cross-sectional cut of Configuration A Rosalila stress results at Rosalila's center room midspan (90% saturation level).

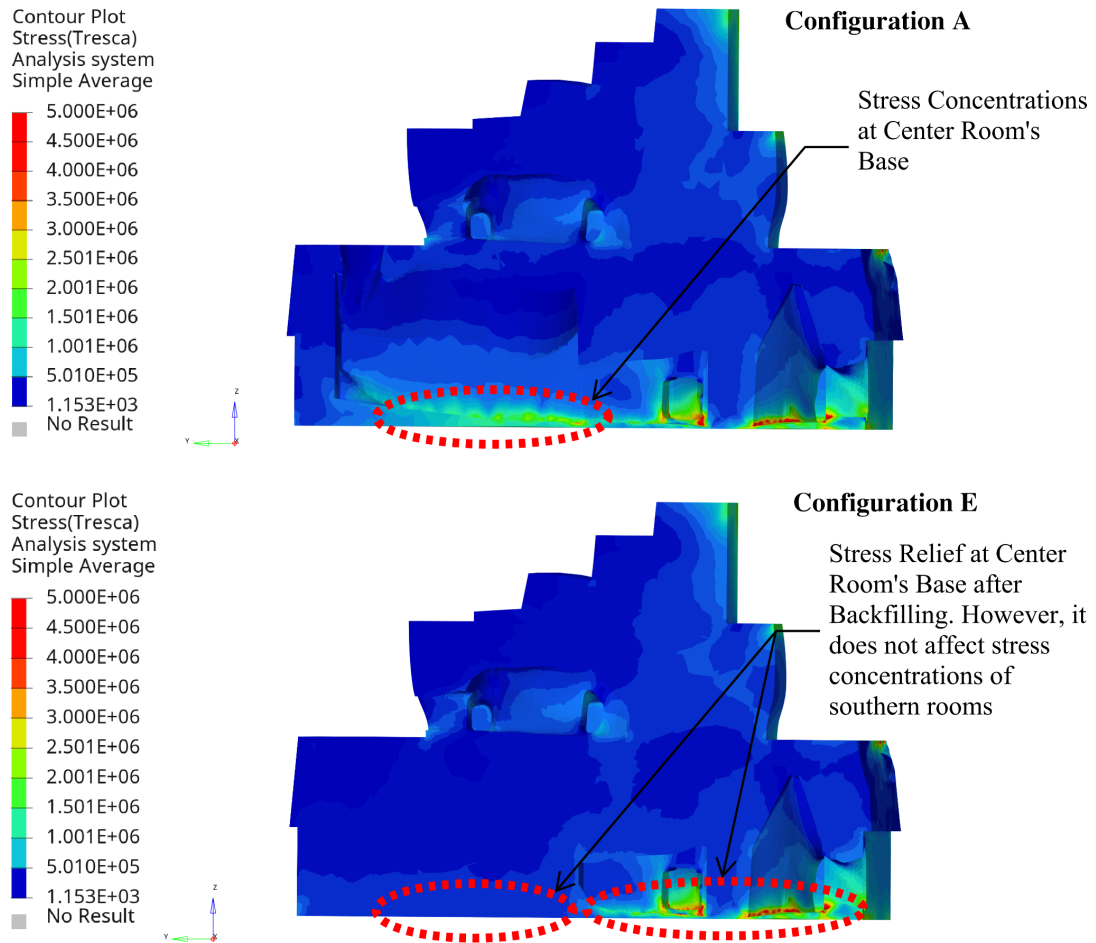


Figure 5.57. Comparison of stress concentrations levels at areas surrounding Rosalila's center room between configuration A (all tunnels included) and configuration E (center room filled) (view from the west).

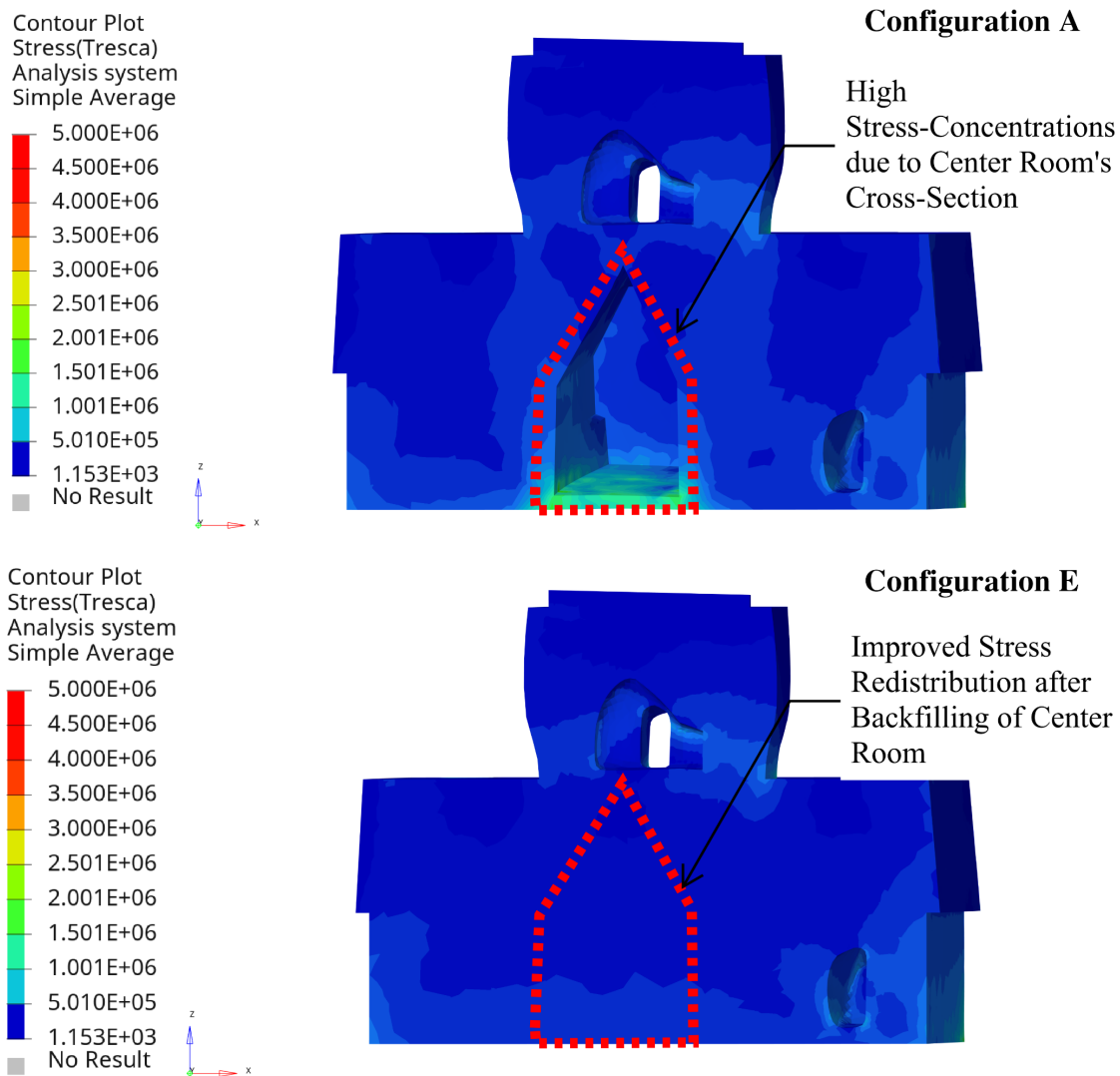


Figure 5.58. comparison of stress concentrations levels at areas surrounding Rosalila's center room between configuration A (all tunnels included) and configuration E (center room filled) (view from the south).



### 5.3.3.3 Rosalila's Southern Wall Repair

Figure 5.59 compares the stress distribution of Rosalila's southern wall in its current state (Configuration A) with the hypothetical configuration where the overhangs on each end of the southern wall are filled or repaired (Configuration F). As originally shown in Figure 5.49, the western portion of Rosalila's southern wall show high levels of stress. High-stress levels are observed in areas of sharp geometry along the first level's roof due to the tunnel excavation in this region. These stress concentrations reach a peak as the tunnels approach the corners of the roof. The current overhangs on each end of the wall experience high stress levels, with the western overhang exposed to the highest stresses (Figure 5.59, top). On the other hand, Configuration F results show a significant improvement in these areas when the southern wall is repaired (Figure 5.59, bottom). When comparing the stress distribution of Rosalila in Configuration F with that in Configuration A (current state) in Figure 5.59, it can be seen that repairing the first-level roof from the current overhangs can significantly improve the local stress flow in these areas. Results show that stress levels are reduced by half in the surrounding overhang regions when they are backfilled with material.

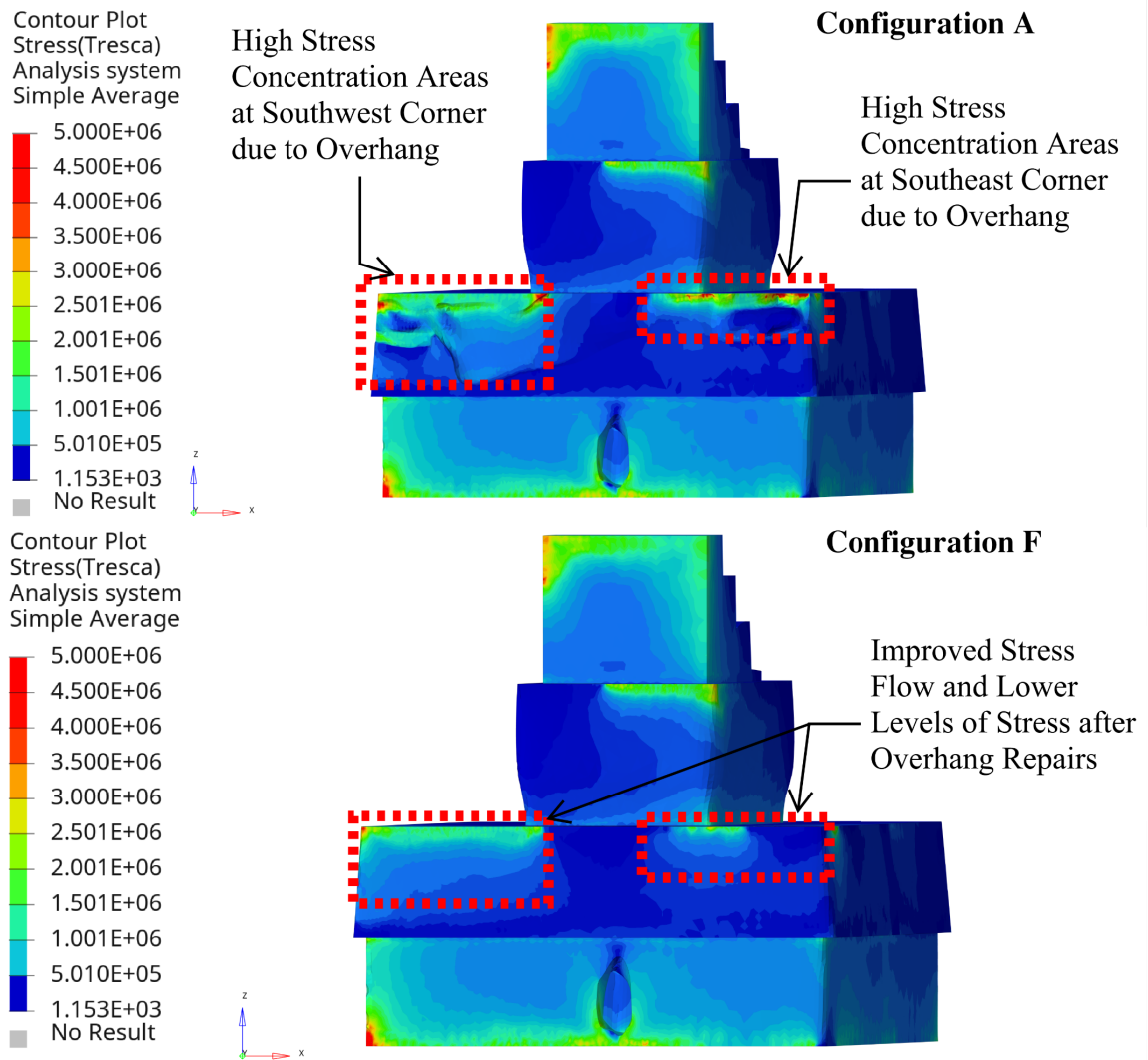


Figure 5.59. Comparison of stress concentrations levels at Rosalila's southern wall between configuration A (current state) and configuration E (southern wall fixed) (view from the south).

## CHAPTER 6 – CONCLUSIONS AND FUTURE WORK

### 6.1 Research Findings

Temple 16 is an ancient Maya structure located at the heart of the Copán Acropolis in Copán Ruinas. Due to its archaeological and historical relevance, a system of archaeological tunnels was excavated inside this structure. This has led to several conservation issues within Temple 16's underlying structures, such as Rosalila, due to the stability and collapse of the excavated areas. The overall goal of this thesis was to conduct a detailed structural assessment of Temple 16, accounting for the complex 3D tunnel system and the impact on Rosalila, to understand the leading causes of tunnel collapse and structural deterioration. For this, high-fidelity geometries of Temple 16, the buried Rosalila structure, and the complex archaeological tunnel system were generated leveraging three-dimensional point clouds from both ground-based lidar and unmanned aerial systems. These point clouds were vectorized to capture relevant geometric details of the system and regenerate high-fidelity three-dimensional CAD geometric models, which were ultimately meshed for finite element analysis.

Finite element analyses were conducted for six configurations to investigate questions including the overall influence of excavated tunnels on Temple 16, the influence of specific tunnels and excavations on the overall tunnel system, and the influence of current excavations on the buried Rosalila structure and its currently deteriorating state. The generated finite-element meshes for each configuration were analyzed by considering three infill saturation levels (90%, 70%, and 50%) to represent variations in the water table and water intrusion throughout the seasons. Therefore, a total

of 18 different finite-element models were generated and analyzed in an implicit linearly elastic static analysis in LS-DYNA.

The obtained results were grouped according to the saturation level used for a generated model. Models analyzed under the same saturation level were used to draw qualitative conclusions based on configuration comparisons. When no tunnels are included in the model, the results show high stress concentrations at the southern half of Rosalila due to its proximity to Temple 16's center axis. The load transferred from this area of Rosalila to lower areas of Temple 16 creates high-stress zones within an influence radius of up to 16 meters. The tunnels that were then excavated near these areas show regions with high stress concentrations, as expected. In total, sixty-three highly stressed tunnel locations were identified within Temple 16 based on its current state of excavation. These high stress concentrations include the tunnels excavated in close proximity to the buried Rosalila and Oropéndola structures as well as the tunnels that lie directly below Rosalila's southern portion. The locations of stress concentrations were the same in all saturation levels.

Results show that backfilling certain tunnel sections can improve or worsen the stress state of others. The impact of backfilling a tunnel section depends on the location of the section and its surrounding conditions. From the considered configurations, a complete backfill of tunnels laying below 598 meters of elevation (below the buried Rosalila structure) can alleviate the applied stress concentrations in upper tunnels by an average of 5.5%. On the other hand, complete backfill of tunnels laying above this elevation can increase the applied stress concentrations in lower tunnels by an average of

6.0%. The impact of these hypothetical backfilling scenarios was approximately the same for all considered saturation levels element analysis.

Results further show that the excavated center room of Rosalila has relatively little impact on the rest of the tunnel system. When the center room is backfilled, tunnels below Rosalila had an average stress increase of only 1.1% with the highest stress increase of 11% occurring at affected areas that lie directly below the center room. Furthermore, the backfilling of Rosalila's center room does not appreciably affect the stresses within Rosalila itself. It is noted that most of the stress concentrations that are observed within Rosalila occur at the base of excavated rooms on the southern side of the structure. Backfilling the center room does not alleviate these stresses since most of the center room is located on the northern side of the structure. Finally, results show a further increase in the stress concentrations observed in the southern side of Rosalila due to the existing tunnels excavated around this region. It was shown that the existing excavated overhangs at the western and eastern ends of Rosalila's southern wall façade are currently exposed to high stress levels due to the pre-established load path around this area. It was observed that there is a 100% stress decrease around these areas when these areas of the façade are fixed.

## **6.2 Future Work**

The current conclusions drawn from this thesis serve as a precedent and a resource for future conservation efforts to preserve Temple 16, Rosalila, and the Copán Acropolis for future generations. The presented pipeline for finite element model generation can be used for more complex models that include future states of the tunnel system. However, it

is worth noting that the current analysis approach presents some uncertainties and limitations due to limited knowledge about actual infill distribution within Temple 16 and limited knowledge about the mechanical properties of these materials. Without proper knowledge of how these materials behave and are distributed along the structure, obtaining representative results of each tunnel section's stability and local behavior is challenging. In this sense, the performed analysis and obtained results were based on the assumption that the idealized infill layers behave elastically, given the limited mechanical understanding of how these layers behave. While this approach effectively identifies areas of high-stress concentrations, the current results do not incorporate the inelastic behavior of material that ultimately triggers tunnel collapse. Furthermore, tunnel consolidation material should also be tested, calibrated, and incorporated into the model to provide a comprehensive risk assessment of which tunnel sections need additional reinforcement. Therefore, the obtained results serve as a starting point for detecting areas of concern within the tunnel system based on the applied demands since more information is required in order to assess the actual system's capacity.

The obtained results show the level of geometric sensitivity that the system has when buried structures such as Rosalila are accounted for within Temple 16's model. This thesis relied on collected geometric information to study the influence of the excavated tunnels on the deterioration of Rosalila and vice versa. However, the results indicate that accounting for the rest of the buried structures within Temple 16 will change how the load is distributed within the system. Furthermore, obtained results also showed the correlation between tunnel areas affected by high stress due to their proximity to other

tunnel sections. Because this thesis mainly accounted for tunnels excavated near Rosalila, incorporating the rest of the tunnel system into the model will also provide a broader understanding of affected areas due to tunnel excavation, as was shown in the results. Therefore, incorporating the structures such as Oropéndola and the rest of Temple 16's tunnel system will improve the accuracy of obtained results.

In conclusion, future work may include:

- Calibrating and incorporating material infill properties and infill distributions along the system that are the result of proper geomechanical testing and analysis.
- Conducting a non-linear analysis to verify and compare the accuracy of obtained results derived from the linear approach.
- Incorporating geometric models of Oropéndola, other buried structures, and the rest of the tunnel system that were not acknowledged during geometric modeling.
- A more robust case study should be conducted incorporating seismic and water saturation effects into the tunnel system.

## REFERENCES

- Agurcia Fasquelle, R. (2004). Rosalilla, Temple of the Sun-King. In Understanding Early Classic Copan. (E. E. Bell, M. A. Canuto, & R. J. Sharer, Eds.) *University of Pennsylvania Museum of Archaeology and Anthropology*, 101-111.
- Agurcia Fasquelle, R., & Fash, B. W. (2005). The evolution of Structure 10L-16, heart of the Copán Acropolis. *Copán. The history of an ancient kingdom*, 201-237.
- Agurcia Fasquelle, R., Bell, E. E., & Sharer, R. J. (2004). Rosalila, Temple of the Sun-King. In Early Classic Copan. *Understanding Classic Copan*, 101-112.
- Alejano, L., & Bobet, A. (2012, July). Drucker-Prager Criterion. *Rock Mechanics and Rock Engineering*, 995-999. doi:10.1007/s00603-012-0278-2
- Altair. (2023). *Altair Products*. Retrieved from Altair Hyperworks:  
<https://altair.com/hyperworks>
- ANSYS. (2023). *ANSYS Products*. Retrieved from ANSYS LS-DYNA:  
<https://www.ansys.com/products/structures/ansys-ls-dyna>
- Asociación Copán. (2019). *Rosalila Temple Preservation Progress*. Retrieved from Asociación Copán: <https://asociacioncopan.org/rosalila-temple-preservation-progress/>
- Asociación Copán. (2019). *The Importance of Rosalila*. Retrieved from Asociación Copán: <https://asociacioncopan.org/the-importance-of-rosalila/>



AutoDesk. (2022). *AutoDesk*. Retrieved from AutoCAD:

[https://www.autodesk.com/products/autocad/overview?mktvar002=4256055%7CSEM%7C848920971%7C40773794622%7Caud-308487391399:kwd-14891210&utm\\_source=GGL&utm\\_medium=SEM&utm\\_campaign=GGL\\_ACA D\\_AutoCAD\\_AMER\\_US\\_eComm\\_SEM\\_BR\\_RMKT\\_EX\\_0000\\_4256055\\_General&utm\\_id=42560](https://www.autodesk.com/products/autocad/overview?mktvar002=4256055%7CSEM%7C848920971%7C40773794622%7Caud-308487391399:kwd-14891210&utm_source=GGL&utm_medium=SEM&utm_campaign=GGL_ACA D_AutoCAD_AMER_US_eComm_SEM_BR_RMKT_EX_0000_4256055_General&utm_id=42560)

Barazzetti, L., Banfi, F., Raffaella, B., Oreni, D., Previtali, M., Roncoroni, F., . . .

Schiantarelli, G. (2015). BIM from Laser Clouds and Finite Element Analysis combining Structural Analysis and Geometric Complexity. *The International Archives of the Photogrammetry, Remote Sensing and Spatial Information Sciences*, 40, 345-350. Retrieved from <https://re.public.polimi.it/handle/11311/982125>

Baudez, C.-F. (1983). Introducción a la Arqueología de Copán, Honduras. Proyecto Arqueológico. *Secretaria de Estado en el Despacho de Cultura y Turismo*.

Beheshti, S. (2015). 3D Model Generation and FEM analysis of Santa Maria Novella.

*Politecnico Di Milano, Civil Engineering Department - Master Thesis*. Retrieved from <https://www.politesi.polimi.it/bitstream/10589/112889/3/Santa.Maria.Novella.The.sis.pdf>

Bell, E. E. (2004). Understanding Early Classic Copan. (M. A. Canuto, & R. J. Sharer, Eds.) *University of Pennsylvania Museum of Archaeology and Anthropology*.

- Brune, P., & Perucchio, R. (2012). Roman Concrete Vaulting in the Great Hall of Trajan's Markets: Structural Evaluation. *Journal of Architectural Engineering*, 18(4), 332-340. Retrieved from [https://ascelibrary.org/doi/abs/10.1061/\(ASCE\)AE.1943-5568.0000086](https://ascelibrary.org/doi/abs/10.1061/(ASCE)AE.1943-5568.0000086)
- Castellazzi, G., Maria D' Altri, A. B., Selvaggi, I., & Lambertini, A. (2015). From Laser Scanning to Finite Element Analysis of Complex Buildings by Using a Semi-Automatic Procedure. *Sensors*, 18360-18380. doi:10.3390/s150818360
- Celada, B., & Beniaowski, Z. (2019). *Ground Characterization and Structural Analyses for Tunnel Design*. CRC Press.
- Chácará, C., Zvietcovich, F., Carolina, B., Marques, R., Perucchio, R., Castañeda, . . . Aguilar, R. (2014). On-Site Investigation and Numerical Analysis for Structural Assesment of the Archeological Complex of Huaca de la Luna. *Proceedings of the SAHC2014: 9th international conference on structural analysis of historical constructions*. Mexico City. Retrieved from <http://www.hms.civil.uminho.pt/sahc/2014/topic04-fullpaper009.pdf>
- Chase, A. F., Chase, D. Z., Morris, J. M., Awe, J. J., & Chase, A. S. (2020). Archaeology and Heritage Management in the Maya Area: History and Practice at Caracol, Belize. *Heritage* 3(2), 436-456. Retrieved from <https://doi.org/10.3390/heritage3020026>
- Chun, K., & Kemeny, J. (2017). From LIDAR Scanning to 3d FEM Analysis for Complex Surface and Underground Excavations. *American Geophysical Union*

*Fall Meeting Abstracts*, (pp. IN43D-0095). Retrieved from  
<https://ui.adsabs.harvard.edu/abs/2017AGUFMIN43D0095C/abstract>

CloudCompare. (2019, February 20). *CloudCompare Wiki*. Retrieved from Global Shift and Scale:

[https://www.cloudcompare.org/doc/wiki/index.php/Global\\_Shift\\_and\\_Scale](https://www.cloudcompare.org/doc/wiki/index.php/Global_Shift_and_Scale)

CloudCompare. (2022). *CloudCompare*. Retrieved from CloudCompare Home Site:

<https://www.danielgm.net/cc/>

Cook, R. D., Malkus, D. S., Plesha, M. E., & Witt, R. J. (2001). *Concepts and Applications of the Finite Element Method* (4th ed.). New York: Wiley.

Das, B. M., & Sobhan, K. (2017). *Principles of Geotechnical Engineering* (9th ed.). United States: Cengage.

DYNAmore. (2011). Review of Soild Element Formulations in LS-DYNA. *LS-DYNA Forum 2011*. Stuttgart: DYNAmore.

Ebolese, D., Lo Brutto, M., & Dardanelli, G. (2019). THE INTEGRATED 3D SURVEY FOR UNDERGROUND ARCHEOLOGICAL ENVIRONMENT. *The International Archives of the Photogrammetry, Remote Sensing and Spatial Information Sciences*, XLII(2).

Fash, B. W., Larios Villalta, R. C., & Lopez, F. (2004). Cross-Section of the Copán Acropolis on the central axis of Structure 10L-16. *Reconstruction Drawings by B. Flash after R. Larios and F. Lopez*. Copán, Honduras.

Fash, W. (2001). *Scribes, Warriors, and Kings: The City of Copan and the Ancient Maya*.

*Thames and Hudson*.

Fash, W., & Agurcia Fasquelle, R. (2005). Contributions and Controversies in the Archaeology and History of Copán. In Copán: The History of an Ancient Maya Kingdom. (E. Andrews, & W. Fash, Eds.) *School of American Research Advanced Seminar Series*, 3-32.

Flickr User. (2019, December 18). *Copán: Temple 10L-16*. Retrieved from Flickr:

<https://www.flickr.com/photos/zug55/49701092637/in/photostream/>

Google Earth. (2023). *Satellite Location of Copan Ruinas*. Retrieved from

<https://earth.google.com/web/>: <http://www.maphill.com/honduras/copan/copan-ruinas/location-maps/satellite-map/>

Gordon, G. (1896). *Prehistoric Ruins of Copan, Honduras. A preliminary Report of the Explorations by the Museum, 1891-1895* (Vol. I). Harvard University.

Guarnieri, A., Pirotti, F., Pontin, M., & Vettore, A. (2005). Combined 3D surveying techniques for structural analysis applications. *The International Archives of the Photogrammetry, Remote Sensing and Spatial Information Sciences*, 36.

Retrieved from <https://www.isprs.org/proceedings/xxxvi/5-W17/pdf/28.pdf>

Hemeda, S. (2021). Geo-environmental monitoring and 3D finite elements stability analysis for site investigation of underground monuments. Horemheb tomb (KV57), Luxor, Egypt. *Heritage Science*(9). doi:<https://doi.org/10.1186/s40494-021-00487-3>

- Hemeda, S. (2022). Finite Element Assesment FEA of polymer anti-seismic piling techniques for protection of the underground culture heritage. *Heritage Science*, 10-35. Retrieved from <https://doi.org/10.1186/s40494-022-00677-7>
- Hohmann, H., & Kostka, R. (1995). Geodetic and Photogrametric Survery of Monuments and Sides. Cuadernos de Arquitectura Mesoamericana número 29. *Seminario de Arquitectura Prehispánica* (pp. 21-28). Mexico D.F: Facultad de Arquitectura, Universidad Nacional Autónoma de México.
- Hohmann, H., & Vogrin, A. (1982). *Die Architektur Von Copan* (Vol. III). Graz: Academic Publishers.
- Kaartinen, E., Dunphy, K., & Sadhu, A. (2022). LiDAR-Based Structural Health Monitoring: Applications in Civil Infrastructure Systems. *Sensors*, 1-32. doi:10.3390/s22124610
- Kirsch, E. (1898). Die Theorie der Elastizitat und die Bedurfnisse der Festigkeitslehre. *Zeitschrift des Vereines deutscher Ingenieure*, 797-907.
- Labuz, J., & Zang, A. (2012, July). Mohr-Cuolomb Failure Criteria. *Rock Mechanics and Rock Engineering*, 975-979. doi:10.1007/s00603-012-0281-7
- Lacombe, L. (2017). *Informe Interino y Resultados Preliminares a tomar en cuenta*. Instituto Hondureño de Antropología e Historia .
- Lacombe, L., Fash, W. L., & Fash, B. W. (2020). *Plan for Long-Term Conservation of the Copan Acropolis Tunnels*. Copán: Peabody Museum of Archeology and

Ethnology Santander Program for the Research and Conservation of Maya Sculpture - Harvard University in collaboration with Instituto Hondureño de Antropología e Historia.

Lacombe, L., Flash, W., & Flash, B. (2020). *Plan for Long-Term Conservation of the Copan Acropolis Tunnels*. Copán: Santander Program for Research and Conservation of Maya Sculpture - Harvard University in collaboration with Instituto Hondureño de Antropología e Historia.

Larios Villalta, R. C. (2018). *Túneles de la Acrópolis de Copán y su Conservación*. Copán: Copan Acropolis Conservation Committee.

Larios Villalta, R. C. (2020). Copan Acropolis sections W50 and W54 facing West. *PAAC Drawing Set*. Proyecto Arqueológico de la Acrópolis de Copán, Copán, Honduras.

Lercari, N., Campiani, A., Stuardo, L., & Rodrigo. (2018). Intra-site Digital Documentation of the Ancient Maya city of Palenque, Mexico. *2018 24th International Conference on Virtual Systems & Multimedia (VSMM 2018)* (pp. 1-8). San Francisco: 3rd Digital Heritage International Congress (DigitalHERITAGE). doi:10.1109/DigitalHeritage.2018.8810003

Livermore Software Technology Corporation (LSTC). (2018). *LS-DYNA Keyword User's Manual* (Vol. I). Livermore, California, United States of America: LSTC.  
Retrieved from <https://www.dynasupport.com/manuals>

Livermore Software Technology Corporation (LSTC). (2018). *LS-DYNA Keyword User's Manual* (Vol. II). Livermore, California, United States of America: LSTC.

Lowiecka, I., Armesto, J., Arias, P., & Lorenzo, H. (2009). Historic bridge modelling using laser scanning ground penetrating radar and finite element methods in the context of structural dynamics. *Engineering Structures*, 31(11), 2667-2676.  
Retrieved from <https://doi.org/10.1016/j.engstruct.2009.06.018>

Mark, R., & Hutchinson, P. (1986, March). On the Structure of the Roman Parthenon. *The Art Bulletin*, 68(1), 24-34. Retrieved from  
<https://www.jstor.org/stable/3050861>

MathWorks. (2023). *MATLAB*. Retrieved from MathWorks :  
<https://www.mathworks.com/products/matlab.html>

Milani, G., Casolo, S., Andrea, N., & Tralli, A. (2012). Seismic Assesment of a Medieval Masonry Tower in Northern Italy by Limit Nonlinear Static, and Full Dynamic Analyses. *International Journal of Architectural Heritage: Conservation, Analysis, and Restoration*, 6(5), 489-524. Retrieved from  
<https://doi.org/10.1080/15583058.2011.588987>

Murthy, V. (n.d.). *Geotechnical Engineering: Principles and Practices of Soil Mechanics and Foundation Engineering*. New York: Marcel Dekker.

Pires, F., Bilotta, E., Flora, A., & Lourenco, P. (2021). Assessment of Excavated Tunnels Stability in the Maya Archeological Area of Copan, Honduras. *International Journal of Architecture Heritage*, 1-19.

- Pires, F., Bilotta, E., Flora, A., & Lourenco, P. B. (2021). Assesment of Excavated Tunnels Stability in the Maya Archeological Area of Copán, Honduras. *International Journal of Architectural Heritage*, 1-19. Retrieved from <https://doi.org/10.1080/15583058.2021.1931730>
- Pix4D. (2023). *Pix4DSurvey*. Retrieved from Pix4D: <https://www.pix4d.com/product/pix4dsurvey/>
- Proskouriakoff, T. (1946). *Reconstruction of Copan Acropolis as it would have looked like in the late 8th century*. Washington DC: Carnegie Institute. doi:50-63-20/18487
- Remondino, F. (2014). *3D Recording and Modelling in Archaeology and Cultural Heritage (BAR International Series)*. (S. Campana, Ed.) BAR International Series.
- Remondino, F., Gruen, A., Von Schwerin, L., Eisenbeiss, H. R., Giardi, S., Sauerbier, M., & Richards-Rissetto, H. (2009). Multi-Sensor 3D Documentation of the Maya Site of Copán. *22nd CIPA Symposium*. Kyoto: Commission, V, WGV/4.
- Richards-Rissetto, H. (2007). Exploring Social Dynamic at rhe Ancient Site of Copán. *ESRI Professional Papers*.
- Richards-Rissetto, H. (2010). Exploring social interaction at the ancient Maya city of Copán, Honduras: A multi-scalar Geographic Information Systems (GIS) analysis of access and visibilty. Retrieved from <https://www.proquest.com/openview/4351084eb1c6d260f75ee507fb982d66/1?pq-origsite=gscholar&cbl=18750>



- Sapirstein, P. (2016). Accurate measurement with photogrammetry at large sites. *Journal of Archaeological Science*, 137-145. doi:<https://doi.org/10.1016/j.jas.2016.01.002>
- Sharer, R. D., Sedat, D. W., Traxler, L. P., Bell, E. E., Canuto, M. A., & Powell, C. (1999). "Early Classic Architecture Beneath the Copan Acropolis: A Research Update. *Ancient Mesoamerica*(10), 3-23.
- Sharer, R. J., Miller, J. C., & Traxler, L. P. (1992). Evolution of Classic Period Architecture in the Eastern Acropolis, Copan: A Progress Report. *Ancient Mesoamerica*(3), 145-159.
- Stephens, J. (1841). *Incidents of Travel in Central America, Chiapas and Yucatan*. New York.
- Stromsvik, G. (1946). *Actividades arqueológicas desarrolladas en Copán por el Gobierno de Honduras en Colaboración con la Institución Carnegie de Washington*. Mexico City: Secretaría de Educación Pública, Carnegie Institution of Washington & Conferencia Internacional de Arqueólogos del Caribe.
- Stromsvik, G. (1947). *Guidebook to the Ruins of Copan*. Washington D.C, USA: Carnegie Institution of Washington.
- Stuart, D. (2004). The Beginnings of the Copan Dynasty: A Review of the Hieroglyphic and Historical Evidence. In Understanding Early Classic Copan. (E. E. Bell, & R. J. Sharer, Eds.) *University of Pennsylvania Museum Press*, 215-247.
- Timoshenko, S., & Goodier, J. (1970). *Theory of Elasticity* (3rd ed.). McGraw-Hill.

- Traxler, L. P. (2004). Redesigning Copan: Architecture of the Polity Center at the Time of the Dynastic Founding.” In *Understanding Early Classic Copan*. (E. E. Bell, M. A. Canuto, & R. J. Sharer, Eds.) *University of Pennsylvania Museum Press*.
- Turner, B. L., Johnson, W., Mahood, G., & Jackie, P. (1983). Hábitat y Agricultura en la región de Copán. In *Introducción a la arqueología de Copán, Honduras* (Vol. 1, pp. 42-58). Tegucigalpa: Secretaría de Estado, Despacho de Cultura y Turismo.
- Ustundag, C., Sesigur, H., Cili, F., & Yazici, G. (2012). Finite Element Analysis of the Seismic Performance of a Historical Masonry Cistern. *15th World conference of Earthquake Engineering, paper, 2178*.
- von Schwerin, J. (2011). THE SACRED MOUNTAIN IN SOCIAL CONTEXT. SYMBOLISM AND HISTORY IN MAYA ARCHITECTURE: TEMPLE 22 AT COPAN, HONDURAS. *Ancient Mesoamerica*(22(2)), 271-300.
- Windward, J. D., & Eileen, H. S. (2013). *Soils Climate and Society*. Boulder: University Press of Colorado.
- Wood, R. L., Mohammadi, M. E., Abdulrahman, L. M., Barbosa, A. R., Olsen, M. J., Kawan, C. K., & Shakya, M. (2017, December 1). Damage Assessment and Modeling of the Five-Tiered Pagoda-Style Nyatapola Temple. *Earthquake Spectra, 118*. doi:10.1193/121516eqs235m

[illegible]

```

$#                                     title
Solid_Lower_Layer
$#   pid      secid      mid      eosid      hgid      grav      adpopt      tmid
    1107      1         1         0         10         0         0         0
*PART
$HWCOLOR COMPS      1109      27
$NAME
$#                                     title
Solid_Middle_Layer
$#   pid      secid      mid      eosid      hgid      grav      adpopt      tmid
    1109      1         2         0         10         0         0         0
*DEFINE_CURVE_TITLE
Gravity Loading Curve
$#   lcid      sidr      sfa      sfo      offa      offo      dattyp      lcint
    1         0         1.0      1.0      0.0      0.0      0         0
$#
    al         ol
    0.0        0.0
    4.0        1.0
    100.0      1.0
*LOAD_BODY_Z
$#   lcid      sf      lciddr      xc      yc      zc      cid
    1      9.806      0      0.0      0.0      0.0      0
*CONTROL_ACCURACY
$#   osu      inn      pidosu      iacc
    1         4         0         1
*CONTROL_BULK_VISCOSITY
$#   q1      q2      type      btype      tstype
    1.5      0.06      1         0         0
*CONTROL_ENERGY
$#   hgen      rwen      slnten      rylen      irgen
    2         2         2         2         2
*CONTROL_HOURLGLASS
$#   ihq      qh
    6         0.1
*CONTROL_IMPLICIT_DYNAMICS
$#   imass      gamma      beta      tdybir      tdydth      tdybur      irate      alpha
    0         0.6      0.38      0.0      10.0      15.0      1         0.0
*CONTROL_IMPLICIT_GENERAL
$#   imflag      dt0      imform      nsbs      igs      cnstn      form      zero_v
    1         1.0      2         1         2         0         0         0
*CONTROL_IMPLICIT_SOLUTION
$#   nsolvr      ilimit      maxref      dctlol      ectol      rctlol      lstol      abstol
    1         11      151.00000E-51.00000E-41.00000E10      0.91.00000E-20
$#   dnorm      diverg      istif      nlprint      nlnorm      d3itctl      cpchk
    2         1      99999      0         0         0         0
$#   arcctl      arcdir      arcrlen      arcmtth      arcdmp      arcpsi      arcalf      arctim
    0         0         0.0         1         2         0         0         0
$#   lsmtld      lsdir      irad      srad      awgt      srad      srad
    4         2         0.0         0.0         0.0         0.0
*CONTROL_IMPLICIT_SOLVER
$#   lsolvr      lprint      negev      order      drcm      drcprm      autospc      autotol
    2         3         2         0         4         0.0      1         0.0
$#   lcpack      mtxdmp      iparm1      rparm1      rparm2
    2         0      5001.00000E-9      0.001
$#   emxdmp      rdcmem
    0         0.85
*CONTROL_OUTPUT
$#   npopt      neecho      nrefup      iaccop      opifs      ipnint      ikedit      iflush
    1         3         0         0         0.0         0         100      5000
$#   iprtf      ierode      tet10s8      msgmax      ipcurv      gmdt      ipldblt      eocs
    0         0         1         50         0         0.0         0         0
$#   tolev      newleg      frfreq      minfo      solsig      msgflg      cdetol
    2         0         1         1         0         1         10.0
$#   phschng      demden      icrfile      spc2bnd      penout      shlsig      hisnout      engout
    0         0         0         0         0         0         0         0
$#   insf      isolsf      ibsf      issf      mlkbag
    0         0         0         0
*CONTROL_SOLID
$#   esort      fmatrix      niptets      swlocl      psfail      t10jtol      icohed      tet13k

```

```

      0      0      5      1      0      0.0      0      0
$#  pm1    pm2    pm3    pm4    pm5    pm6    pm7    pm8    pm9    pm10
      0      0      0      0      0      0      0      0      0      0
*CONTROL_SOLUTION
$#  soln      nlq      isnan      lcint      lcacc      ncdef      nocop
      0      0      0      1000      0      1      0
*CONTROL_TERMINATION
$#  endtim      endcyc      dtmin      endeng      endmas      nosol
      05.0      0      0.0      0.01.000000E8      0
*DATABASE_BNDOUT
$#  dt      binary      lcur      ioopt
      0.01      0      0      1
*DATABASE_ELOUT
$#  dt      binary      lcur      ioopt      option1      option2      option3      option4
      0.01      0      0      1      0      0      0      0
*DATABASE_GLSTAT
$#  dt      binary      lcur      ioopt
      0.01      0      0      1
*DATABASE_MATSUM
$#  dt      binary      lcur      ioopt
      0.01      3      0      1
*DATABASE_NODFOR
$#  dt      binary      lcur      ioopt
      0.01      0      0      1
*DATABASE_NODOUT
$#  dt      binary      lcur      ioopt      option1      option2
      0.01      0      0      1      0.0      0
*DATABASE_RBDOUT
$#  dt      binary      lcur      ioopt
      0.01      0      0      1
*DATABASE_RCFORC
$#  dt      binary      lcur      ioopt
      0.01      0      0      1
*DATABASE_SECFORC
$#  dt      binary      lcur      ioopt
      0.01      0      0      1
*DATABASE_SLEOUT
$#  dt      binary      lcur      ioopt
      0.01      0      0      1
*DATABASE_SPCFORC
$#  dt      binary      lcur      ioopt
      0.01      0      0      1
*DATABASE_BINARY_D3PLOT
$#  dt      lcdt      beam      npltc      psetid
      0.01      0      0      0      0
$#  ioopt      rate      cutoff      window      type      pset
      0      0.0      0.0      0.0      0      0
*DATABASE_BINARY_INTFOR
$#  dt      lcdt      beam      npltc      psetid
      0.01      0      0      0      0
*DATABASE_EXTENT_BINARY
$#  neiph      neips      maxint      strflg      sigflg      epsflg      rltflg      engflg
      0      0      3      1      1      1      1      1
$#  cmpflg      ieverp      beamip      dcomp      shge      stssz      n3thdt      ialemat
      0      1      0      1      1      1      2      1
$#  nintsld      pkp_sen      sclp      hydro      msscl      therm      intout      nodout
      1      0      1.0      0      0      0
$#  dtdt      resplt      neipb      quadr      cubic
      0      0      0      0      0
*DATABASE_EXTENT_INTFOR
$#  nglbv      nvelo      npresu      nshear      nforce      ngapc      nfail      ieverf
      1      1      1      1      1      1      0      0
$#  nwear      nwusr      nhuf      ntied      neng      npen
      0      2      0      0      0      0
*END

```

## APPENDIX B -STRESS CONCENTRATIONS RESULT LIST

*Table B.1. Description and location of identified stress concentrations at upper-level tunnels.*

General Information		Geophysical Coordinates		
Label #	Description	X (m)	Y (m)	Z (m)
U1	Upper Level Junction of Tunnels 18 and 11 at Rosalia Southwest Corner	269555.516	1641424.69	602.688
U2	Upper Level Tunnel (Tunnel 42) at Rosalia First-Level South Entrance	269562.778	1641423.48	601.896
U3	Upper Level Junction of Tunnels 46 and 46v2 at Rosalia Southeast First-Level Corner	269567.957	1641423.41	600.685
U4	Upper-Level Tunnel (Tunnel 25) Connecting Rosalia's second and third levels at Southwest Corner	269560.54	1641428.49	611.913
U5	Upper-Level Junction of Tunnels 21 and 20 at Second-Level Rosalia Southeast Corner	269564.962	1641426.84	611.089
U6	Tunnel 54 at 3 meters west from junction with Tunnel 46	269569.25	1641441.66	601.503
U7	Upper-Level Tunnel (Tunnel 4) at Rosalia Southwest First-Level Roof Corner	269556.21	1641424.56	607.31
U8	Upper-Level Junction of Tunnels 22 and 4 at Rosalia Southeast First-Level Roof Corner	269567.707	1641422.92	607.654
U9	Upper-Level at 1 meter west to Junction of Tunnels 20 and 4 at Rosalia's First-Level Roof	269560.049	1641423.94	607.397
U10	Upper-Level Tunnel (Tunnel 18) at 3 meters north of Junction with Tunnel 11 and 2 meters from Rosalia's West Entrance	269556.203	1641428.15	601.842
U11	Upper-Level Tunnel at 2.7 meters South of junction with Tunnels 46v and 56 (Rosalia's Eastern Side)	269570.214	1641430.25	600.157
U12	Upper-Level Junctions of Visitors Tunnels, Tunnel 24 and Tunnel 18 at Rosalia's First-Level Northwest Roof Corner	269560.178	1641442.15	607.578
U13	Upper-Level Tunnel 18 at Rosalia West Wall Tunnel in front to Rosalia's Western Entrance	269555.901	1641433.83	601.986
U14	Upper Level, Western Access to Tunnel System, at Junction to Tunnels 4 and 32	269548.391	1641424.88	602.923
U15	Upper Level, Junction of Tunnels 32 and 11	269549.09	1641426.55	602.336
U16	Upper Level 4 meters west of Junction to Tunnels 4 and 32	269551.654	1641423.55	604.482
U17	Upper-Level Tunnel 42 at 6 meters south of Rosalia's Southern Entrance	269560.552	1641417.53	602.265
U18	Upper-Level Junction of Tunnels 42 and 53A	269560.944	1641412.62	603.673
U19	Upper-Level 8 meters north of Junction of Tunnels 53A and 60	269562.896	1641409.69	602.142
U20	Upper-Level Junction of Tunnels 82 and 82A	269566.906	1641404.94	602.238
U21	Upper-Level Tunnel 82, 1 meter north of Tunnel 60	269566.666	1641402.76	602.109
U22	Upper-Level 6 meters west Junction of Tunnels 82 and 82A	269572.451	1641403.9	602.269
U23	Upper-Level Tunnel 52, 1 meter south of Tunnel 51A	269567.443	1641412.34	602.14
U24	Upper-Level Junction of Tunnels 51 and 51A	269569.512	1641414.72	602.048
U25	Upper-Level Tunnel 45, 1 meter west of Tunnel 84	269571.787	1641418.77	600.547
U26	Upper Level Tunnel 46v2 Vertical Shaft	269566.399	1641422.13	600.423
U27	Upper-Level Junction of Tunnels 86 and 46	269570.312	1641425.28	600.033
U28	Upper-Level East side of Junction of Tunnels 35 and 33	269553.317	1641434.02	600.018
U29	Upper-Level Tunnel 35, 3 meters south of Junction of Tunnels 35 and 33	269552.589	1641431.35	599.409
U30	Upper-Level Tunnel 33, 1 meter west of Junction of Tunnels 35 and 33	269551.273	1641434.46	599.005
U31	Upper-Level Junction of Tunnels 43 and 33	269542.654	1641433.73	599.315
U32	Upper-Level Tunnel 43, 3 meters south of Junction of Tunnels 43 and 33	269541.731	1641432.76	596.604

Table B.2. Description and location of identified stress concentrations at lower-level tunnels.

Label #	General Information	Geophysical Coordinates		
		X (m)	Y (m)	Z (m)
L1	Xukpi Stone Room	269561.894	1641432.17	594.542
L2	Xukpi Stone Room	269564.414	1641432.96	594.584
L3	Xukpi Stone Room	269564.472	1641434.83	594.588
L4	Upper chamber of Margarita (east of Xukpi stone) where the tunnel connects with the lower 1/28 Margarita substructure	269566.818	1641433.22	594.509
L5	Upper chamber of Margarita (east of Xukpi stone) where the tunnel connects with the lower 1/28 Margarita substructure	269567.347	1641433.31	594.466
L6	Xukpi Stone Room	269563.659	1641431.13	594.775
L7	Tunnel to the south of the Xukpi Stone Room on the Margarita platform	269563.027	1641428.53	594.306
L8	Tunnel to the south of the Xukpi Stone Room on Margarita platform	269560.528	1641428.97	594.606
L9	Tunnel to the south of the Xukpi Stone Room on Margarita platform	269561.678	1641429.2	594.421
L10	Tunnel to the west of the Xukpi Stone Room on Margarita platform	269561.266	1641434	594.649
L11	Tunnel to the west of the Xukpi Stone Room on Margarita platform	269558.068	1641433.8	594.782
L12	Tunnel to the west of the Xukpi Stone Room on Margarita platform	269560.815	1641432.3	594.39
L13	Stairs from upper Margarita platform to Margarita façade	269550.318	1641433.21	593.317
L14	Tunnels to the south of the Margarita bird mask façade	269553.088	1641427.53	591.849
L15	Margarita bird mask façade	269552.727	1641432.33	591.444
L16	Tunnels to the south of the Margarita bird mask façade	269553.123	1641426.09	591.211
L17	Tunnels to the south of the Margarita bird mask façade	269552.215	1641426.21	591.486
L18	Tunnel that connects Margarita bird mask façade to Yenal Mask	269552.016	1641436.53	591.306
L19	Tunnel to the west of Yenal	269551.357	1641439.73	590.886
L20	Tunnel that connects Yenal to the Hunal Tomb	269554.484	1641438.56	589.883
L21	Tunnel that connects Yenal to the Hunal Tomb	269557.479	1641437.4	589.63
L22	Yenal Mask	269554.798	1641435.37	589.811
L23	Main tunnel at the north base of the Margarita substructure	269559.127	1641442.46	592.065
L24	Main tunnel at the north base of the Margarita substructure	269563.913	1641442.65	591.336
L25	Tunnel that connects Yenal to the Hunal Tomb	269559.605	1641437.05	590.454
L26	Hunal Tomb	269564.427	1641438.46	590.704
L27	Main tunnel at the east base of the Margarita substructure	269569.369	1641435.28	591.694
L28	Main tunnel near east stairs between Clavel and Margarita substructure	269570.722	1641434.88	590.975
L29	Main tunnel near Clavel	269575.965	1641435.52	590.946
L30	Main tunnel near Clavel	269576.487	1641435.18	590.969
L31	Main tunnel near Clavel	269572.841	1641441.92	593.17

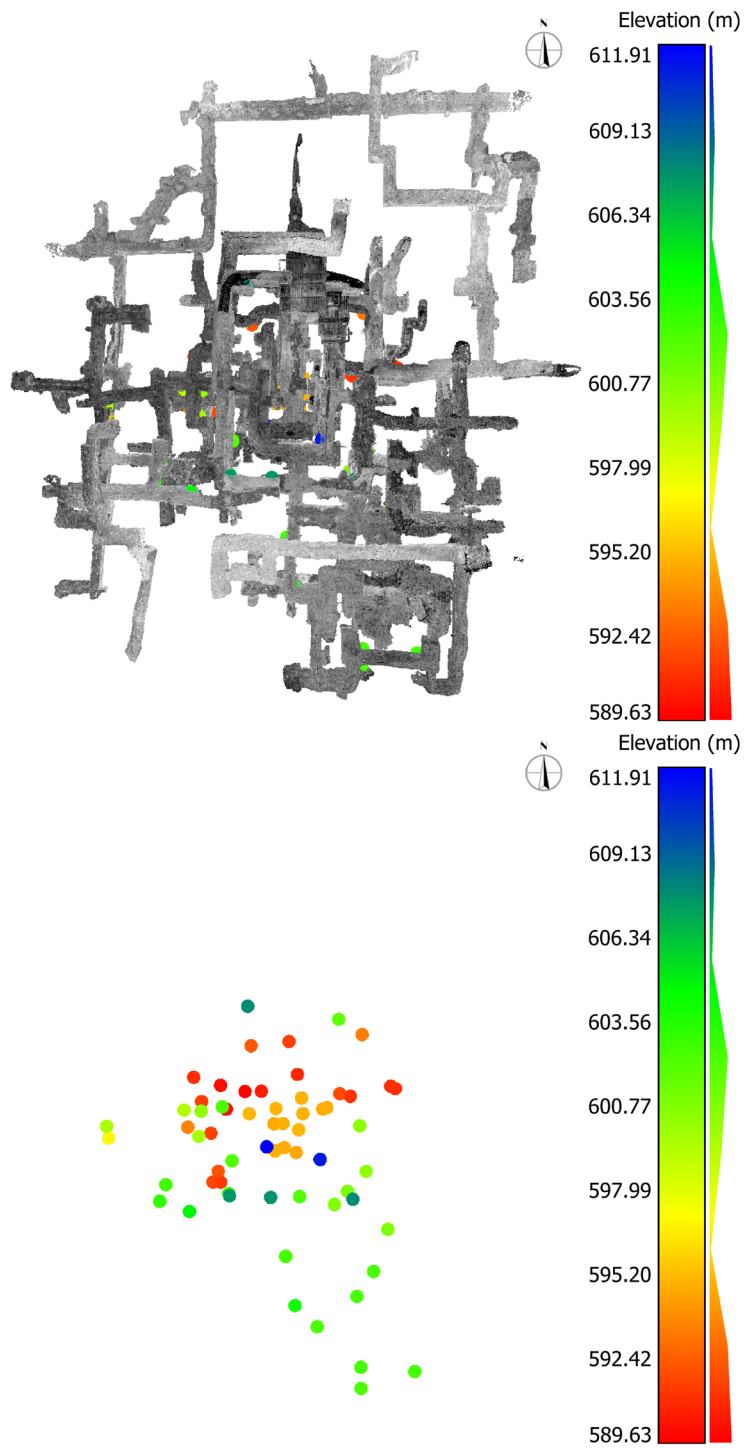


*Figure B.1. Top view of 63 identified areas with high stress levels along Temple 16 tunnels (top) and isolated locations (bottom).*



Table B.3. Stress concentration results for upper-level tunnels at 90% saturation

Label #	<i>Configuration Results</i>				<i>Configuration Comparisons</i>		
	Config A Tresca Stress (Pa)	Config. C Tresca Stress (Pa)	Config. D Tresca Stress (Pa)	Config. E Tresca Stress (Pa)	Config. A vs C (%)	Config. A vs D (%)	Config. A vs E (%)
U1	1701379.38	1825200.38	-	-	7.28%	-	-
U2	1859049.25	1545081.25	-	-	-16.89%	-	-
U3	1154794	1144687.13	-	-	-0.88%	-	-
U4	1779349.88	1723257.63	-	-	-3.15%	-	-
U5	1873230	1808932.5	-	-	-3.43%	-	-
U6	763122.688	797402.688	-	-	4.49%	-	-
U7	1958905.5	2100794.5	-	-	7.24%	-	-
U8	2062927.75	2388678.5	-	-	15.79%	-	-
U9	2700745	2843786.75	-	-	5.30%	-	-
U10	1376033	1231093.88	-	-	-10.53%	-	-
U11	1147017.25	983546.5	-	-	-14.25%	-	-
U12	1184130.5	1026245.81	-	-	-13.33%	-	-
U13	1134853.13	1196560.5	-	-	5.44%	-	-
U14	1123292.63	1078820.5	-	-	-3.96%	-	-
U15	943926.312	835294.25	-	-	-11.51%	-	-
U16	876292.5	812857.812	-	-	-7.24%	-	-
U17	1003575.63	972684.312	-	-	-3.08%	-	-
U18	954545.5	949009.375	-	-	-0.58%	-	-
U19	1087837.13	1016955	-	-	-6.52%	-	-
U20	901110.5	882135.125	-	-	-2.11%	-	-
U21	983865.25	862181.188	-	-	-12.37%	-	-
U22	1012878.25	1107275	-	-	9.32%	-	-
U23	890363	888646.062	-	-	-0.19%	-	-
U24	954290.875	884995.25	-	-	-7.26%	-	-
U25	1051428.75	767323.75	-	-	-27.02%	-	-
U26	1154358.75	1105218.38	-	-	-4.26%	-	-
U27	928411.938	878287.625	-	-	-5.40%	-	-
U28	1355327	1245859.63	-	-	-8.08%	-	-
U29	838600.75	777324.812	-	-	-7.31%	-	-
U30	1014712.13	816642.688	-	-	-19.52%	-	-
U31	959858.438	932824.75	-	-	-2.82%	-	-
U32	889908.25	540805.625	-	-	-39.23%	-	-

Table B.4. Stress concentration results for lower-level tunnels at 90% saturation.

Label #	Configuration Results				Configuration Comparisons		
	Config A Tresca Stress (Pa)	Config. C Tresca Stress (Pa)	Config. D Tresca Stress (Pa)	Config. E Tresca Stress (Pa)	Config. A vs C (%)	Config. A vs D (%)	Config. A vs E (%)
L1	2220360	-	2200542.5	2249853	-	-0.89%	1.33%
L2	1594991.63	-	1841195.5	1767959.63	-	15.44%	10.84%
L3	2303738.75	-	2048306.38	2387907	-	-11.09%	3.65%
L4	2082793.5	-	2336790.25	2189894.5	-	12.20%	5.14%
L5	1717299.75	-	1839152.75	1753843.5	-	7.10%	2.13%
L6	1493883.25	-	1552079.25	1498263.38	-	3.90%	0.29%
L7	2149407.5	-	2067300	2222782	-	-3.82%	3.41%
L8	2101768.25	-	2643169	2017787.88	-	25.76%	-4.00%
L9	1462786.5	-	1502189.63	1442411.63	-	2.69%	-1.39%
L10	1614625.38	-	1884032.75	1768737.25	-	16.69%	9.54%
L11	1882486	-	2310081.25	1861638.63	-	22.71%	-1.11%
L12	1512523.38	-	1455691.13	1462685	-	-3.76%	-3.30%
L13	2047747.63	-	2046003	2006288	-	-0.09%	-2.02%
L14	1767792.5	-	1799139.5	1757018.63	-	1.77%	-0.61%
L15	1472950	-	1492059.5	1476207	-	1.30%	0.22%
L16	1970024.88	-	2138989.75	2051310	-	8.58%	4.13%
L17	1538232.25	-	1500708.63	1567769.75	-	-2.44%	1.92%
L18	1660816	-	1722323.5	1649408.63	-	3.70%	-0.69%
L19	1559441	-	1991498.25	1531967.63	-	27.71%	-1.76%
L20	1677530.75	-	1685517.38	1705462.5	-	0.48%	1.67%
L21	1480841.25	-	1472133.5	1473855.5	-	-0.59%	-0.47%
L22	1512024	-	1617156.38	1512307.25	-	6.95%	0.02%
L23	1554056.13	-	1671727.5	1496565.88	-	7.57%	-3.70%
L24	1566953.63	-	1671167	1503533.5	-	6.65%	-4.05%
L25	1939758	-	2239175	2061048	-	15.44%	6.25%
L26	1517681.75	-	1599852	1575455.5	-	5.41%	3.81%
L27	1534475	-	1685637	1524584.5	-	9.85%	-0.64%
L28	1595485.25	-	1524003.25	1601409.5	-	-4.48%	0.37%
L29	1561407.63	-	1636989.5	1570646.5	-	4.84%	0.59%
L30	1494240	-	1513005.63	1500285.75	-	1.26%	0.40%
L31	1752581	-	1946705.38	1770471.5	-	11.08%	1.02%

Table B.5. Stress concentration results for upper-level tunnels at 70% saturation.

Label #	<i>Configuration Results</i>				<i>Configuration Comparisons</i>		
	Config A Tresca Stress (Pa)	Config. C Tresca Stress (Pa)	Config. D Tresca Stress (Pa)	Config. E Tresca Stress (Pa)	Config. A vs C (%)	Config. A vs D (%)	Config. A vs E (%)
U1	1606625	1722719.88	-	-	7.23%	-	-
U2	1739680.5	1448363.38	-	-	-16.75%	-	-
U3	1074979.38	1065754	-	-	-0.86%	-	-
U4	1632914	1578093.25	-	-	-3.36%	-	-
U5	1720424.63	1664962.88	-	-	-3.22%	-	-
U6	726563.625	758908.125	-	-	4.45%	-	-
U7	1776549.75	1907194.38	-	-	7.35%	-	-
U8	1885095.25	2183220.25	-	-	15.81%	-	-
U9	2436192.75	2568552.75	-	-	5.43%	-	-
U10	1298325.13	1159440.38	-	-	-10.70%	-	-
U11	1078585.88	924455.875	-	-	-14.29%	-	-
U12	1060027.25	921679	-	-	-13.05%	-	-
U13	1039640	1097696	-	-	5.58%	-	-
U14	1040882.31	999772.062	-	-	-3.95%	-	-
U15	875187.5	774898.75	-	-	-11.46%	-	-
U16	811735.875	752962.312	-	-	-7.24%	-	-
U17	929318.438	902046.062	-	-	-2.93%	-	-
U18	881457.438	876225.25	-	-	-0.59%	-	-
U19	1003966.06	940211.5	-	-	-6.35%	-	-
U20	831024.25	813589.75	-	-	-2.10%	-	-
U21	907035.875	796434.688	-	-	-12.19%	-	-
U22	934254.188	1019744.88	-	-	9.15%	-	-
U23	822460.562	820589	-	-	-0.23%	-	-
U24	881844.125	819046.25	-	-	-7.12%	-	-
U25	975330.438	712008.062	-	-	-27.00%	-	-
U26	1074413.75	1028247.75	-	-	-4.30%	-	-
U27	869665.625	822388.25	-	-	-5.44%	-	-
U28	1254874.5	1154049.63	-	-	-8.03%	-	-
U29	781603.062	723939.688	-	-	-7.38%	-	-
U30	939709.938	757086	-	-	-19.43%	-	-
U31	888490.688	863875.938	-	-	-2.77%	-	-
U32	827085.875	501918.5	-	-	-39.31%	-	-

Table B.6. Stress concentration results for lower-level tunnels at 70% saturation.

Label #	<i>Configuration Results</i>				<i>Configuration Comparisons</i>		
	Config A Tresca Stress (Pa)	Config. C Tresca Stress (Pa)	Config. D Tresca Stress (Pa)	Config. E Tresca Stress (Pa)	Config. A vs C (%)	Config. A vs D (%)	Config. A vs E (%)
L1	2072021.75	-	2056449.13	2099589	-	-0.75%	1.33%
L2	1489900.25	-	1717570.13	1650034.38	-	15.28%	10.75%
L3	2152756	-	1917821.38	2242737.75	-	-10.91%	4.18%
L4	1940816.38	-	2174371.5	2040745	-	12.03%	5.15%
L5	1601182.5	-	1718112	1635947.25	-	7.30%	2.17%
L6	1394024.25	-	1448333.75	1398541.63	-	3.90%	0.32%
L7	2006217.75	-	1927458.63	2074087.88	-	-3.93%	3.38%
L8	1961068.13	-	2463804.5	1883781	-	25.64%	-3.94%
L9	1363599.5	-	1400952.63	1345185.5	-	2.74%	-1.35%
L10	1511618	-	1760524.75	1656104.75	-	16.47%	9.56%
L11	1764313.63	-	2159193.25	1745196.88	-	22.38%	-1.08%
L12	1408143.5	-	1357024.88	1363769.25	-	-3.63%	-3.15%
L13	1906176.38	-	1904499.25	1866910	-	-0.09%	-2.06%
L14	1652627.75	-	1682718.25	1642822.5	-	1.82%	-0.59%
L15	1378005.75	-	1395202.25	1381261.75	-	1.25%	0.24%
L16	1833886.63	-	1997691.75	1915840.75	-	8.93%	4.47%
L17	1433096.25	-	1398973.88	1460082.88	-	-2.38%	1.88%
L18	1551079.5	-	1608465	1540944	-	3.70%	-0.65%
L19	1461032	-	1867464.5	1437072	-	27.82%	-1.64%
L20	1574203.5	-	1582688.5	1600871.25	-	0.54%	1.69%
L21	1389762.25	-	1381417	1382440.5	-	-0.60%	-0.53%
L22	1416671	-	1515238.75	1416977.13	-	6.96%	0.02%
L23	1450381.88	-	1561996.13	1398844	-	7.70%	-3.55%
L24	1467282.88	-	1564193.13	1408814.5	-	6.60%	-3.98%
L25	1820351.38	-	2101996.13	1933497.38	-	15.47%	6.22%
L26	1420978.13	-	1499171.63	1476523.75	-	5.50%	3.91%
L27	1427975.63	-	1569405.75	1418733.25	-	9.90%	-0.65%
L28	1488570	-	1421680.38	1491121.5	-	-4.49%	0.17%
L29	1455021.5	-	1526192.13	1464185.75	-	4.89%	0.63%
L30	1394052	-	1412079.5	1399863	-	1.29%	0.42%
L31	1634346.75	-	1813565.38	1650385.13	-	10.97%	0.98%

Table B.7. Stress concentration results for upper-level tunnels at 50% saturation.

Label #	<i>Configuration Results</i>				<i>Configuration Comparisons</i>		
	Config A Tresca Stress (Pa)	Config. C Tresca Stress (Pa)	Config. D Tresca Stress (Pa)	Config. E Tresca Stress (Pa)	Config. A vs C (%)	Config. A vs D (%)	Config. A vs E (%)
U1	1511783.88	1620135	-	-	7.17%	-	-
U2	1621274.75	1352183.88	-	-	-16.60%	-	-
U3	995816.938	987442.312	-	-	-0.84%	-	-
U4	1486931.25	1434250.13	-	-	-3.54%	-	-
U5	1567165.38	1520191.5	-	-	-3.00%	-	-
U6	689952.625	720366.125	-	-	4.41%	-	-
U7	1594769	1714460	-	-	7.51%	-	-
U8	1708306.75	1978614.63	-	-	15.82%	-	-
U9	2180169.25	2302538.25	-	-	5.61%	-	-
U10	1221033.75	1088048.5	-	-	-10.89%	-	-
U11	1009883.5	865197.625	-	-	-14.33%	-	-
U12	937089.875	818071.312	-	-	-12.70%	-	-
U13	944612.5	999027.375	-	-	5.76%	-	-
U14	958659.188	920867	-	-	-3.94%	-	-
U15	806604.312	714453	-	-	-11.42%	-	-
U16	747279.5	693120.125	-	-	-7.25%	-	-
U17	855183.438	831276.25	-	-	-2.80%	-	-
U18	808669.75	803757	-	-	-0.61%	-	-
U19	920423.875	863484.5	-	-	-6.19%	-	-
U20	761253.562	745337.375	-	-	-2.09%	-	-
U21	830569.062	730728.5	-	-	-12.02%	-	-
U22	855867	932782.125	-	-	8.99%	-	-
U23	754733.5	752755.938	-	-	-0.26%	-	-
U24	809745.312	753169.625	-	-	-6.99%	-	-
U25	899382.438	656737.188	-	-	-26.98%	-	-
U26	994520	951436.812	-	-	-4.33%	-	-
U27	810837.25	766493.5	-	-	-5.47%	-	-
U28	1154799.75	1062455.25	-	-	-8.00%	-	-
U29	724463.75	670421.812	-	-	-7.46%	-	-
U30	864698.25	697369.5	-	-	-19.35%	-	-
U31	817046.25	794799.062	-	-	-2.72%	-	-
U32	764060.625	462946.406	-	-	-39.41%	-	-

Table B.8. Stress concentration results for lower-level tunnels at 50% saturation.

Label #	<i>Configuration Results</i>				<i>Configuration Comparisons</i>		
	Config A Tresca Stress (Pa)	Config. C Tresca Stress (Pa)	Config. D Tresca Stress (Pa)	Config. E Tresca Stress (Pa)	Config. A vs C (%)	Config. A vs D (%)	Config. A vs E (%)
L1	1923863.25	-	1911811.88	1949599.5	-	-0.63%	1.34%
L2	1384335.88	-	1593781.38	1531912.63	-	15.13%	10.66%
L3	2001716.63	-	1786779.88	2095859.25	-	-10.74%	4.70%
L4	1798827.75	-	2012068.25	1891526.5	-	11.85%	5.15%
L5	1484874	-	1596358.75	1517778.75	-	7.51%	2.22%
L6	1294056.13	-	1344431.5	1298698.5	-	3.89%	0.36%
L7	1862248.25	-	1787258.13	1924794.75	-	-4.03%	3.36%
L8	1820136.5	-	2284418.5	1749487.88	-	25.51%	-3.88%
L9	1264271.25	-	1299427.63	1247769.5	-	2.78%	-1.31%
L10	1408451	-	1637143.88	1543436.13	-	16.24%	9.58%
L11	1645453.5	-	2007880.5	1628160.5	-	22.03%	-1.05%
L12	1304036.75	-	1258351.63	1264884.25	-	-3.50%	-3.00%
L13	1764190.88	-	1762620.25	1727295.88	-	-0.09%	-2.09%
L14	1537188	-	1565768.13	1528357	-	1.86%	-0.57%
L15	1282871.5	-	1298222.5	1286149.5	-	1.20%	0.26%
L16	1707470.88	-	1855932.5	1779961.5	-	8.69%	4.25%
L17	1327689.75	-	1296913.88	1352195.75	-	-2.32%	1.85%
L18	1441240.38	-	1494576.63	1432310.38	-	3.70%	-0.62%
L19	1362218.25	-	1742699	1341519.38	-	27.93%	-1.52%
L20	1470309.25	-	1479194.38	1495685.75	-	0.60%	1.73%
L21	1298523	-	1290501.88	1290921	-	-0.62%	-0.59%
L22	1321105.63	-	1413109.13	1321448.5	-	6.96%	0.03%
L23	1346478	-	1451765.25	1300581	-	7.82%	-3.41%
L24	1367349.75	-	1456879	1313789.63	-	6.55%	-3.92%
L25	1700427	-	1960316.5	1805633.5	-	15.28%	6.19%
L26	1323885.25	-	1398026	1377317.88	-	5.60%	4.04%
L27	1321340	-	1452985.5	1312692.13	-	9.96%	-0.65%
L28	1381345.13	-	1319166.38	1380785.25	-	-4.50%	-0.04%
L29	1348665	-	1415397.63	1357704.13	-	4.95%	0.67%
L30	1293688.88	-	1310967.13	1299235.25	-	1.34%	0.43%
L31	1515730.25	-	1680270.25	1529985.13	-	10.86%	0.94%